FOSSIL ENERGY

DOE/BC/14126-22
(DE90000250)

# SUPRI HEAVY OIL RESEARCH PROGRAM
# THIRTEENTH ANNUAL REPORT

SUPRI TR 76

By
William E. Brigham
Henry J. Ramey, Jr.
Louis M. Castanier

August 1990

Performed Under Contract No. FG19-87BC14126

Stanford University
Stanford, California

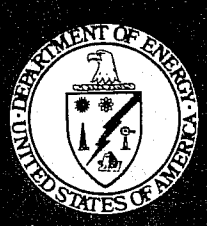


**Bartlesville Project Office**
**U. S. DEPARTMENT OF ENERGY**
**Bartlesville, Oklahoma**

## DISCLAIMER



Available to DOE and DOE contractors from the Office of Scientific and Technical Information, P.O. Box 62, Oak Ridge, Tennessee 37831; prices available from (615)576-8401, FTS 626-8401.

Available to the public from the National Technical Information Service, U.S. Department of Commerce, 5285 Port Royal Rd., Springfield, Virginia 22161.

Price: Printed Copy A07
Microfiche A01

DOE/BC/14126-22
Distribution Category UC-122

# SUPRI HEAVY OIL RESEARCH PROGRAM
# THIRTEENTH ANNUAL REPORT
October 1, 1988-September 30, 1989

SUPRI TR 76

By
William E. Brigham
Henry J. Ramey, Jr.
Louis M. Castanier

August 1990

Work Performed Under Contract No. FG19-87BC14126

Prepared for
U.S. Department of Energy
Assistant Secretary for Fossil Energy

Thomas B. Reid, Project Manager
Bartlesville Project Office
P.O. Box 1398
Bartlesville, OK 74005

Prepared by
Stanford University
Petroleum Research Institute
Stanford, CA 94305-4042

# TABLE OF CONTENTS

## PROJECT 3: STEAM WITH ADDITIVES



## PROJECT 4: RESERVOIR DEFINITION

## PROJECT 5: FIELD SUPPORT SERVICES

# LIST OF TABLES

# LIST OF FIGURES

# SCOPE OF RESEARCH

SUPRI's mission is to conduct research directed towards improved recovery of heavy oils. As most of the existing EOR techniques for heavy oils are thermal recovery methods, emphasis of SUPRI research is on in-situ combustion and steam injection. SUPRI effort is divided into five major projects:

## 1. FLOW PROPERTIES STUDY

To assess the effect of increased temperature and pressure on reservoir properties: This year's effort has focused on experimental determination of temperature effects on oil/water relative permeabilities in consolidated sandstones and on a computer model allowing comparison of relative permeability data from displacement experiments with data obtained by centrifuge experiments. A report on the state of the art in computerized tomography applied to petroleum related experiments has been completed.

## 2. IN-SITU COMBUSTION

To study the parameters affecting in-situ combustion performance: A literature review of various ignition methods has been completed. An analytical study of multiphase multicomponent flow modeling with temperature changes is in progress. This work will be applied to oxygen enriched combustion. Metallic additives are studied in order to modify the reactions of combustion to increase or decrease the amount of fuel burned as needed. Tube runs allow quantitative measurements of the effect of water soluble metallic salts on the combustion of Huntington Beach crude oil.

## 3. STEAM WITH ADDITIVES

To improve sweep efficiency in steam injection: Transient flow of foams generated by surfactants in a sand pack are studied by Cat Scanning. This work should provide data allowing modeling of foam flow in porous media. Experiments aiming at the characterization of surfactants to be used as foaming additives in steam injection were performed. Study of the heat transfer parameters in laboratory experiments is emphazised.

## 4. RESERVOIR DEFINITION

To improve reservoir knowledge before enhanced oil recovery projects: Single well tracer studies to estimate residual oil saturation have been performed. A description of flow through perforations has been completed and a study on the design and interpretation of thermal recovery well testing is in progress. Tracer breakthrough behavior is being studied at nonunity mobility ratio to help evaluate reservoir characteristics.

## 5. FIELD SUPPORT SERVICES

To help solving field related problems: A study on optimizing parallel computing by comparison of Newton and quasi-Newton methods is in progress. A semi-analytical model for steam drive is being derived, this model will allow simulation of dipping reservoirs.

# PROJECT 1: FLOW PROPERTIES STUDY

This project involves measurement of reservoir parameters such as permeabilities, relative permeabilities, and capillary pressure at conditions of temperature and pressure likely to be encountered in thermal recovery processes.

# 1.1 A STUDY OF END EFFECTS IN DISPLACEMENT EXPERIMENTS (S. Qadeer)

Saturation gradients exist both at the inlet and outlet ends of a core during flow experiments. These gradients are caused by the capillary discontinuities at the core ends, and are therefore generally called "capillary end effect". These end effects have been studied extensively from time to time. Attention has concentrated mostly on the outlet end. It is generally believed that the wetting phase does not flow out of the core until its saturation becomes high enough that the capillary forces are negligible. The saturation at which this occurs is still unknown.

The inlet end effect has not received enough attention, and is therefore less understood. Mechanical restriction to the flow at the ends is also a factor, and needs to be studied. All of the core area near the ends may not contribute to the flow, and this can cause extra pressure drop. Similar effects are expected to occur near the injection and production wells, where multiphase flow is occurring.

This study will try to find the applicable boundary conditions for flow experiments which then could be incorporated into the well models in reservoir simulators.

## 1.1.1 LITERATURE REVIEW

Petroleum engineers became interested in the study of multiphase flow in the 1930's. Both gas-liquid and liquid-liquid systems were studied. It was recognized by researchers that end effects exist in the sand packs. The pressure drop and saturations were determined in the middle section of the core to avoid these effects[1,2].

In 1951, Geffen et al.[3] studied the effects of different factors on the laboratory determination of relative permeabilities. They presented experimentally measured saturation profiles across the length of the core. Their results clearly indicated the presence of a capillary end effect.

Richardson et al.[4] compared the experimentally determined saturations in gas-oil systems to those calculated by a simple model which included the outlet capillary end effect (see Fig. 1.1.1). As can be seen, there is a strong outlet end effect. Some disturbance in the saturations at the inlet end is also obvious. They were performing steady state experiments with composite cores. The core was dismanteled and saturations measured by weight balance. It is not obvious therefore whether the fluctuations in the saturation are caused by the capillary forces or because of experimental errors.

Hadley and Handy[5] presented a theoretical analysis of the capillary end effect in steady state experiments. By mathematical modeling they studied the effect of different variables like flowrate, viscosities, and the outlet end saturation on the calculated relative permeabilities. Their analysis confirmed the results from earlier studies regarding the presence of the capillary end effect, and that its effect decreases as the flow rate is increased.

Settari and Aziz[6] implemented the capillary end effect into a single well coning simulator. Sigmund and McCaffery[7] using the same model for outlet end effect found relative permeabilities from low rate laboratory displacement experiments by history matching. They pointed out that use of low rate flow experiments is more appropriate to model field displacements. They

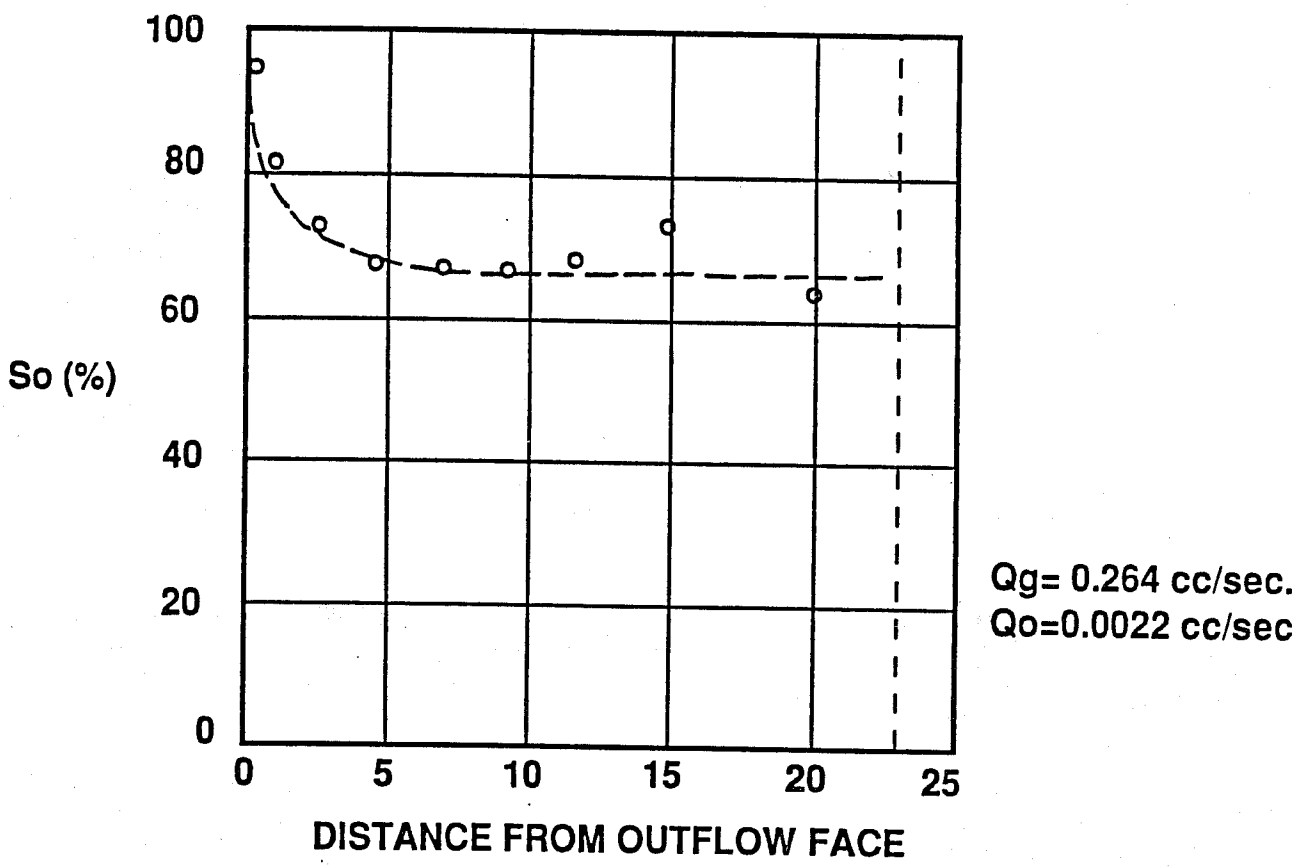


Figure 1.1.1 Comparison of experimental and theoretical saturation gradients due to boundary effect, Richardson et al.[4]

included the outlet end effect by imposing a constraint on the flow of wetting phase out of the core. The wetting phase flows out of the core when its saturation reaches a critical value at which the capillary pressure is zero. After that the flow obeys the Darcy Law. Mathematically this can be written as:

$$q_w = \begin{cases} 0 & \text{if } S_w < S_{w0} \\ \lambda_w \dfrac{\partial p_w}{\partial x} & \text{if } S_w = S_{w0} \end{cases} \tag{1.1.1}$$

Evans et al.[8] presented a core flood simulator that includes both the inlet and outlet effects. Their inlet model considers the accumulation of injected phase in the inlet plenum and thus allows the fraction of injected phase entering the core to change over time. Their outlet model considers a balance of capillary and viscous forces at the outlet face. The wetting phase is allowed to flow out of the core when the viscous forces can overcome the capillary forces. Mathematically their inlet boundary condition can be described by:

$$q - qf_p = V_p \frac{\partial S_p}{\partial t} \tag{1.1.2}$$

$$S_i = S_{wc} + (1 - S_{or} - S_{wc}) * S_p \tag{1.1.3}$$

The capillary pressure at the inlet face of the core is required to be zero. Their outlet boundary condition is:

$$P_w \geq P_p + P_c\ (S_w) \tan \theta \tag{1.1.4}$$

Comparison of the measured and simulated pressure drop data for one of the core floods is presented in Fig. 1.1.2. At early times, their model gives a pressure drop which is different than that observed in the experiment.

Ahmed et al.[9] while injecting at constant pressure into layered sandpack models observed that the flow rate was always greater than expected at the beginning of the flood. Similarly Qadeer[10] during imbibition experiments at constant flow rate observed that the pressure drop is less than that expected (See Fig. 1.1.3). Both clearly indicate the presence of an inlet end effect.

From the preceding discussion the inlet and outlet end effects are not understood completely. Although it is known that wetting phase accumulates at the outlet end, it is not known with certainty to what saturation. Nor are the conditions at the inlet end understood completely. The flow geometry at the core ends is also not known. It is assumed that the fluids flow into and out of the core without restriction, which does not seem to be correct. The purpose of this study is to find the true nature of both inlet and outlet end effect. This will be done by using displacement experiments under differing flow conditions, and by measuring the pressure gradients across the core, and by measuring in situ saturations using computerized tomography.

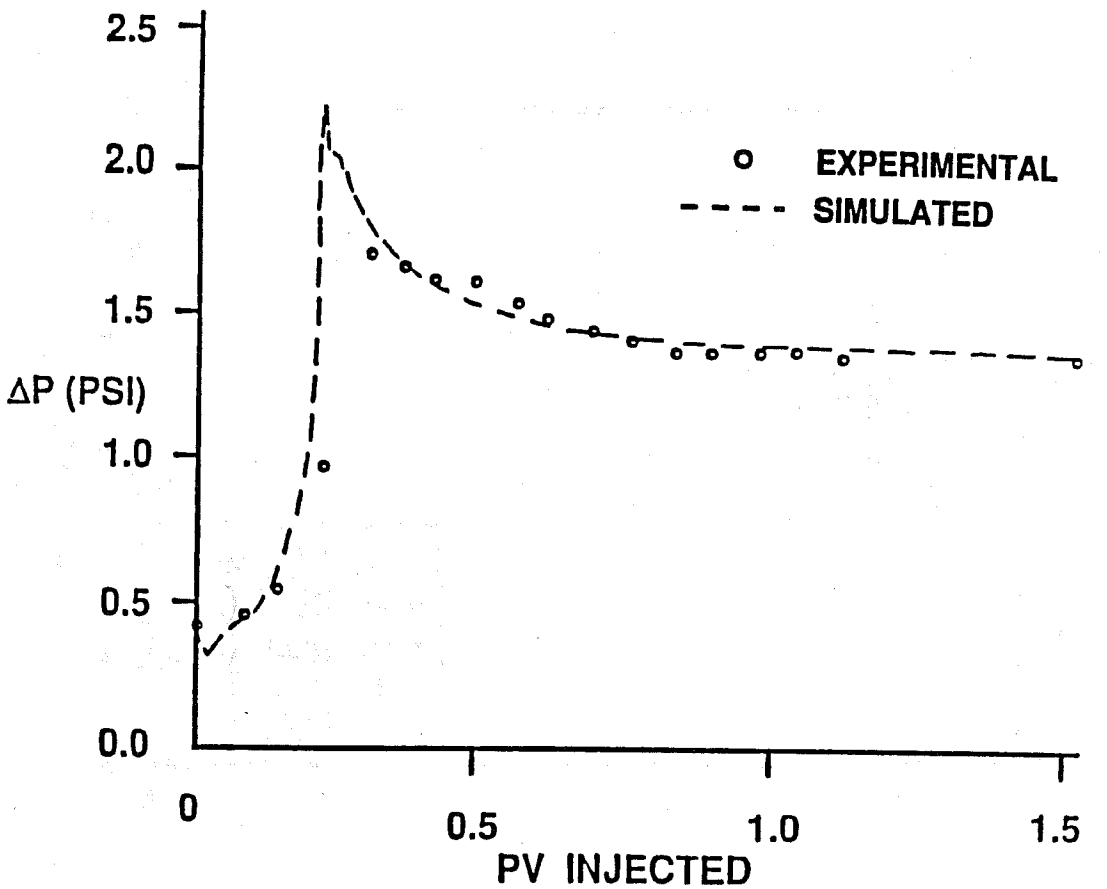


Figure 1.1.2 Base case simulation of experimentally measured pressure drop, Evans et al.[8]

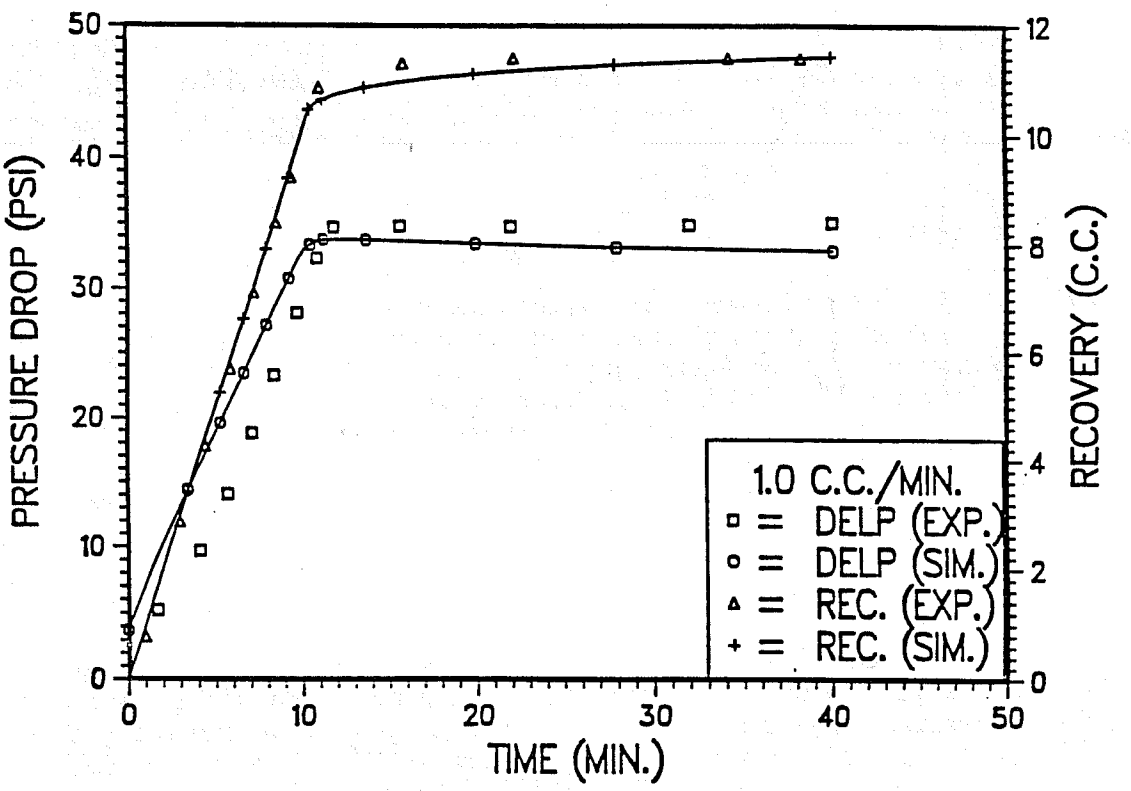


Figure 1.1.3 Experimental and simulated recovery and pressure drop data for 1.0 cc/min imbibition run[10]

## 1.1.2 METHOD OF STUDY

To understand the end effects it is necessary to measure the saturations both across the core length and also along different cross sections of the core. Although it is always assumed that one dimensional flow occurs in laboratory experiments, depending on the effectiveness of the distribution grooves in the inlet plug, it is possible that fluid might not be entering uniformly at the inlet face of the core. This partial flow may continue for some distance into the core. The end plugs are designed so that the volume of the inlet plenum is kept to a minimum. This inherently reduces the distribution capability of the plug. Some experiments will be conducted with no distribution grooves in the plugs to compare with experiments that do use such grooves.

To observe the effect of mobility ratio, the fluids used will be selected to vary the mobility ratio from favorable through unity to unfavorable. Clean oil will be used along with sodium iodide brine. Sodium iodide brine will help in measuring saturation by Cat scanning. The following subsections describe the experimental system and the saturation measurement technique planned.

### Experimental Setup

A core holder has been designed and built using a PVC outer jacket. The details of the core holder are shown in Fig. 1.1.4. The core will be put in an inner rubber sleeve. The annulus between the inner sleeve and outer PVC jacket will be sealed by two tapered plugs. Overburden pressure will be applied through the annulus to ensure that fluids do not bypass the core. One of these plugs will also serve as the inlet end plug. The other plug is hollow and the outlet end plug and spacers can slide in and out from this side. This design will permit the use of different length cores in the same core holder.

Figure 1.1.5 shows the schematic of the experimental system. Two Constametric pumps will be used to inject oil and water phases into the core through separate lines. The pumps will either take fluids from the two fluid reservoirs, or recirculate the fluids produced from the core after they have been separated in the production measurement apparatus. The pressure drop across the core length will be measured by differential pressure transducers. Initially the pressure drop will be measured only between the inlet and outlet end of the core. Based on results from preliminary runs, more pressure taps will be installed near both ends to get pressure profiles along the length of the core.

### Saturation Measurements

The in-situ saturations will be measured by Cat scanning the core during the experiments. Using the X-ray attenuation coefficients, the saturation at any point in the core can be determined with a high degree of accuracy[11]. To get the attenuation coefficients from the Cat scan computer to our data processing computer, an interface has been developed. Using this interface the CT numbers data files are transferred in a format that can be used to calculate saturations at each pixel element of the image. Hence 3-D saturation images can be generated. These saturation determinations will help us to analyze the nature of the end effects.

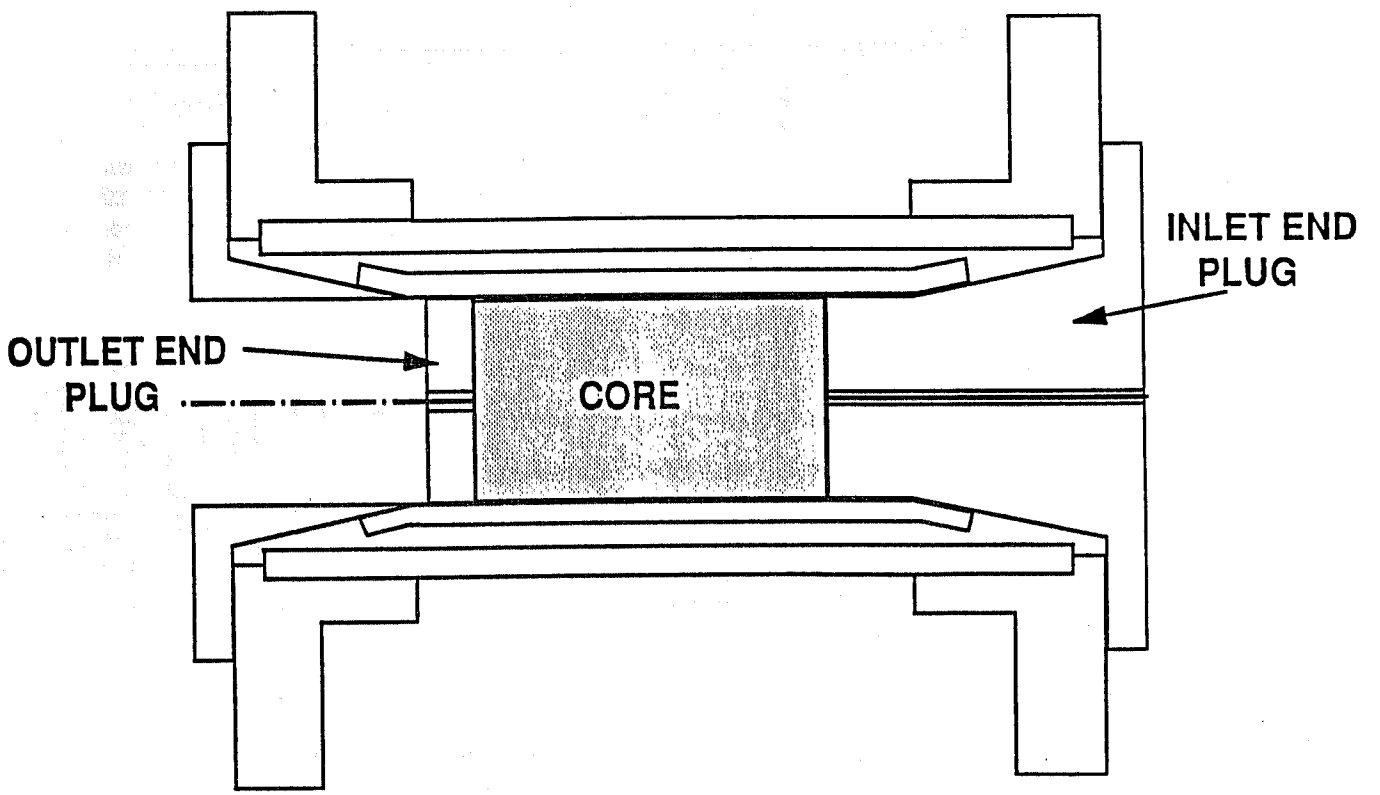


Figure 1.1.4 Cross section through the core holder

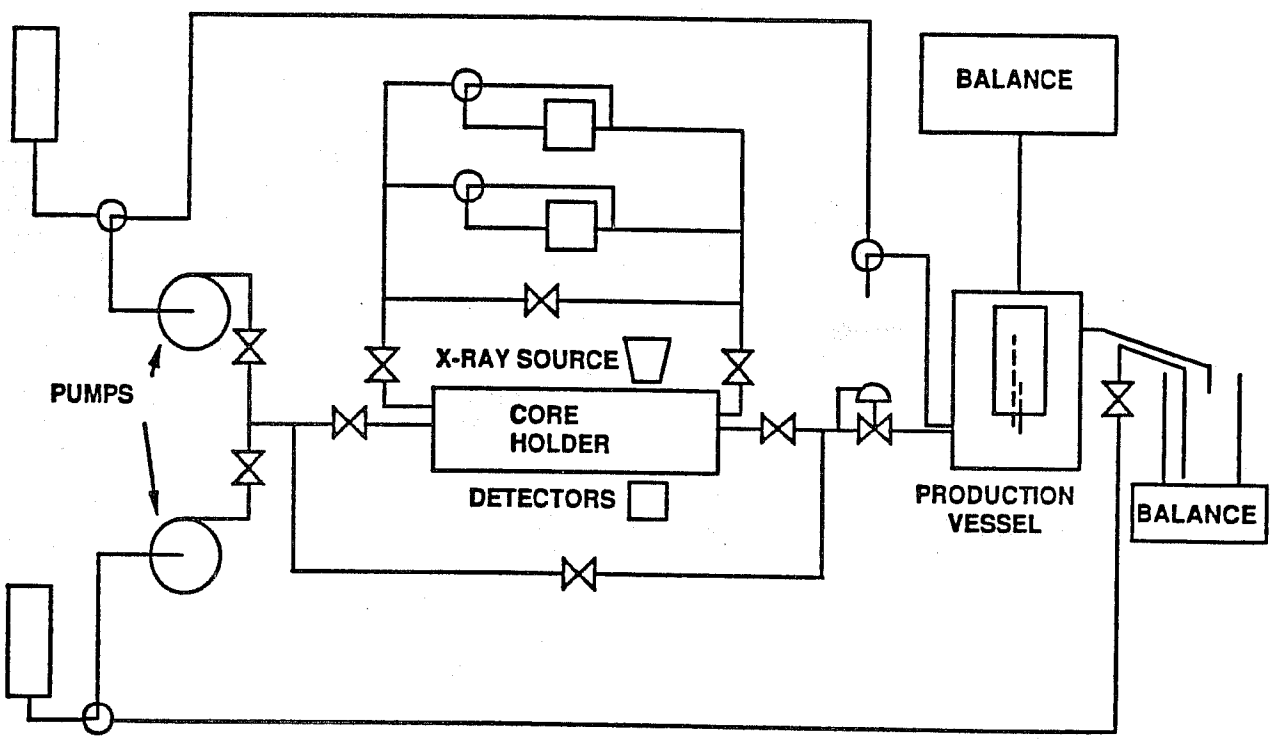


Figure 1.1.5 Schematic of the experimental setup

## 1.1.3 NOMENCLATURE

| | |
|---|---|
| $f$ | fraction of water |
| $P$ | pressure |
| $q$ | flow rate |
| $S$ | saturation |
| $V$ | volume |
| $\lambda$ | mobility |
| $\theta$ | contact angle |

### Subscripts

| | |
|---|---|
| $c$ | capillary |
| $i$ | inlet |
| $or$ | residual oil |
| $p$ | plenum |
| $w$ | wetting phase ,sp |

## 1.1.4 REFERENCES


1. Wyckof, R.D., and Botset, H.G.: "The Flow of Gas-Liquid Mixtures Through Uncomsolidated Sands", Physics (Sept. 1936., 7.

2. Leverett, M.C.: "Flow of Oil-Water Mixtures through Unconsolidated Sands", Trans. AIME (1939., 132, 149-171.

3. Geffen, T.M., Owens, W.W. Parish, D.R. and Morse, R.A.: "Experimental Investigation of Factors Affecting Laboratory Relative Permeability Measurements", Trans. AIME (1951., 192, 99-110.

4. Richardson, J.G., Kerver, J.K., Hafford, J.A. and Osoba, J.S.: "Laboratory Determination of Relative Permeability", Trans. AIME (1952., 195, 187-196.

5. Hadley, G.F. and Handy, L.L.: "A Theoretical and Experimental Study of The Steady State Capillary End Effect", SPE 707-G presented at the 31st Annual Fall Meeting of the Petroleum Branch of the AIME in Los Angeles, Oct. 14-17, 1956.

6. Settari, A. and Aziz, K.: "A Computer Model for Two Phase Coning Simulation", SPEJ (June 1974. 221-236.

7. Sigmund, P.M. and McCaffery, F.G.: "An Improved Unsteady State Procedure for Determining the Relative Permeability Characteristics of Heterogeneous Porous Media", SPEJ (Feb. 1979. 15-28.

8. Evans, A.J., Foulser, R.W. and Weit, G.F.: "Laboratory Water Flood Simulation Including Inlet and Outlet Effects", Report AEEW-R 1985 Oil Recovery Projects Division AEE Winfrith.

9. Ahmed, G., Castanier, L.M. and Brigham, W.E.: "An Experimental Study of Water Flooding in Layered Reservoirs"', SPE 13599, presented at SPE 1985 California Regional Meeting, Bakersfield, California, March 27-29, 1985.

10. Qadeer, S.: "Correcting Oil/Water Relative Permeability Data for Capillary End Effects", M. Sc. thesis University of Alaska Fairbanks, 1988

11. Castanier, L.M.: "An Introduction to Computerized X-Ray Tomography for Petroleum Research", SUPRI TR 66 performed under DOE contract No. DE-FG19-87BC14126.

## 1.2 AN INTRODUCTION TO COMPUTERIZED X-RAY TOMOGRAPHY FOR PETROLEUM RESEARCH (L. Castanier)

A technical report titled "An Introduction to Computerized X-Ray Tomography for Petroleum Research," SUPRI TR 66, by L. Castanier was published in June 1989. The following is an abstract of this report.

This report summarizes the state of the art in the application of medical tomography (CT) to petroleum recovery problems. A brief review of the basic principles of x-ray computerized tomography is followed by a discussion of the governing equations of the method. Calculation techniques and appropriate correlations for continued testing are described and discussed. Existing medical software is reviewed. Consideration of the specific software needed for petroleum engineering as well as applications of new technologies such as image processing and computer networking are described.

Criteria are given for the choice of a machine suitable for most petroleum related applications. Emphasis is placed on flexibility, reliability, accuracy and price of the scanner. Two separate sections discuss positioning of the core and design of the core holders. Examples of possible applications of CT scanning to problems of geology, core analysis, EOR as well as operational process problems are discussed. An appendix presents the status of the CT research at the Stanford University Petroleum Research Institute.

The basic conclusion of this work is that computerized x-ray tomography is a powerful tool for petroleum industry researchers. Present technology allows its use by major research centers in an effective manner providing that some simple criteria are met. Existing hardware is adequate and adaptation of existing medical software in combination with other sources is possible. No new technology is needed.

## 1.3 A COMPARISON OF RELATIVE PERMEABILITY FROM CENTRIFUGING VERSUS COREFLOODING
(David Shimbo)

A technical report titled, "A Comparison of Relative Permeability From Centrifuging Versus Coreflooding," will be published this year. The following is an abstract of this report.

Laboratory measurement of relative permeability has traditionally taken place using unsteady state coreflood tests. Procedures also exist for deriving relative permeabilities from centrifuge data, but the shapes of the curves can be different than those from coreflooding. This research compares coreflood relative permeabilities versus centrifuge relative permeabilities by obtaining coreflood and centrifuge data from the same piece of Berea sandstone for gas/oil and oil/water systems. A one-dimensional coreflood/centrifuge model, a least squares history matching algorithm, and the Corey relationships are used to match the experimental data. Core data is also analyzed using the standard Jones-Roszelle technique. Centrifuge data was analyzed using the model proposed by Hagoort. Jones-Roszelle and Hagoort relative permeability curves are then compared with the Corey curves that were obtained from simulation history matching.

Comparison of the two sets of relative permeability curves from centrifuging versus coreflooding for the oil/water system displayed similar shapes and endpoints for the wetting phase, but showed different shapes and endpoints for the nonwetting phase.

# PROJECT 2: IN-SITU COMBUSTION

SUPRI-s work on in-situ combustion has focused on studies of the effect of metallic additives on the combustion kinetics. Tube runs have been made to verify the results obtained in the kinetics experiments. A detailed survey has been made of ignition techniques used in combustion projects. A new project has been started to correlate the relationship between the amount of fuel for combustion with the residual oil from steam flooding.

## 2.1 MODIFYING IN-SITU COMBUSTION PERFORMANCE BY THE USE OF WATER-SOLUBLE ADDITIVES (D. C. Shallcross, C.F. De los Rios, L.M. Castanier, W.E. Brigham)

A paper titled "Modifying In-Situ Combustion Performance by the Use of Water-Soluble Additives," by D. C. Shallcross, C.F. De los Rios, L.M. Castanier, and W.E. Brigham was presented in SPE-Asia Pacific Conference, Australia (September 13-15, 1989). The following is a summary of this paper.

In-situ combustion is a process not usually associated with recovery of light crude oils. The combustion front usually dies rapidly because the amount of fuel deposited is insufficient to sustain the combustion reactions. Increasing the amount of fuel deposited within the reservoir will enhance the combustion process performance allowing it to be applied to lighter crudes. An investigation was performed to study the effects of a range of catalyzing agents on the kinetics of the main oxidation reactions. These reactions include low temperature oxidation, fuel deposition and fuel combustion. Aqueous solutions of various catalysts were mixed with crude oil and sand. The mixtures were then subjected to a continuous flow of air and a linear heating schedule. The effluent gases were continuously analyzed for composition. Using a kinetic model this information was analyzed by decoupling the total oxygen consumption curve into three components that represent the three major competing oxidation reactions. Using nonlinear regression methods weighted to account for experimental error, estimates were made for the three reactions for the activation energies, pre-exponential factors and reaction rate orders. The catalysts tested included ten water-soluble metallic additives. It was found that the presence of salts of iron and tin increased the amount of fuel formed and deposited on the porous medium for Huntington Beach oil. Conversely the addition of copper, nickel and cadmium salts did not significantly affect fuel deposition. However, the effect of those metals upon the reaction kinetics depends upon the chemical nature of the crude oil, and thus upon the particular oil.

## 2.2 TUBE RUNS WITH METALLIC ADDITIVES
(C. Tavares)

Combustion tube runs were conducted with metallic additives in heavy oil (10°API) from Venezuela. Previous kinetics measurement (see section 2.1) have shown that metallic additives can significantly modify the reactions of combustion and fuel deposition. Last year, a report by Baena described four runs performed on Huntington Beach oil (22.9°API). This year, four additional runs were performed using Hamaca oil (10°API). The equipment and procedure as well as the data analysis techniques are described in detail in a technical report that is in the draft stage (Tavares). Baena also provided a description of the equipment and equations used for the analysis of the tube runs. The following section will concentrate on the results of the four runs on the heavy oil and on a comparison of the results with the previous work performed on lighter oil.

### 2.2.1 SUMMARY OF THE EXPERIMENTAL PROGRAM

Table 2.2.1 shows the parameters for the four runs performed to date. Two control runs were made to verify the repeatability of the results. Despite the fact that the oxygen data were lost by mistake for the first control run, all other measurements showed good repeatability. Table 2.2.1 shows the runs performed by Baena (1989). Zinc chloride was not used as an additive for the heavy oil runs because its effect during previous runs was in between those of tin and iron. All the operating parameters were kept the same for each run and identical to the parameters used by Baena. The additives were introduced in the connate water as aqueous solutions of metallic salts.

### 2.2.2 RESULTS AND DISCUSSION

Figure 2.2.1 shows the raw data for the control run. The oxygen utilization is poor (around 5% oxygen produced). As a result the $CO_2$ produced concentration is low (8 to 10%). The curves of gas produced are not smooth but show peaks and valleys. This phenomenon was also seen in the previous study and was attributed to uneven packing, but in the runs performed with Hamaca oil these variations only occurred during the control runs. Variations in combustion efficiency probably cause the fluctuations observed in the control runs. Figures 2.2.2 and 2.2.3 show the same data for the runs including iron and tin salts. In both runs, the oxygen was completely used during combustion. As a result the $CO_2$ level increased. These curves are more constant over the duration of the experiments.

To compare the runs performed with Hamaca oil with the runs performed with Huntington Beach oil, the following discussion will only pertain to average values. Figure 2.2.4 shows that the presence of metal significantly decreases the oxygen produced in both cases. Figure 2.2.5 shows the average values for $CO_2$. For both oils the control runs show the lowest $CO_2$ values, corresponding with the lowest oxygen utilization.

The Hydrogen/Carbon ratio of the fuel burned, $n$, was calculated and is displayed on Figure 2.2.6. The results here show opposite effects for the light and the heavy oil. While the metals seem to increase $n$ from mere zero for the control runs to 0.8 for the tin run performed on Huntington Beach oil, the effect is reversed using Hamaca oil. The value of $n$ decreases from 1.9 to 1.4 for the control and tin runs.

Table 2.2.1 Table of Combustion Runs

| Huntington Beach Crude Oil | | | | Venezuelan Crude Oil | | | |
|---|---|---|---|---|---|---|---|
| HBO 22.9 Degree API | ø | So | Sw | Hamaca Field 10 Degree API | ø | So | Sw |
| Control, No Additive | .3573 | .3747 | .2705 | Control, No Additive | .4663 | .1354 | .1351 |
| Iron, 1% by wt. FeCl2.4H2O | .3500 | .3867 | .2792 | Iron, 2% mole FeCl2.4H2O | .3657 | .2278 | .2046 |
| Tin, 1% by wt. SnCl2.2H2O | .3910 | .3243 | .2341 | Tin, 2% mole SnCl2.2H2O | .3413 | .1834 | .1834 |
| Zinc, 1% by wt. ZnCl2.----- | .3927 | .3221 | .2325 | Control, No Additive | .3850 | .1885 | .1890 |

p = 100 psig flow rate = 3 SLPM for all runs

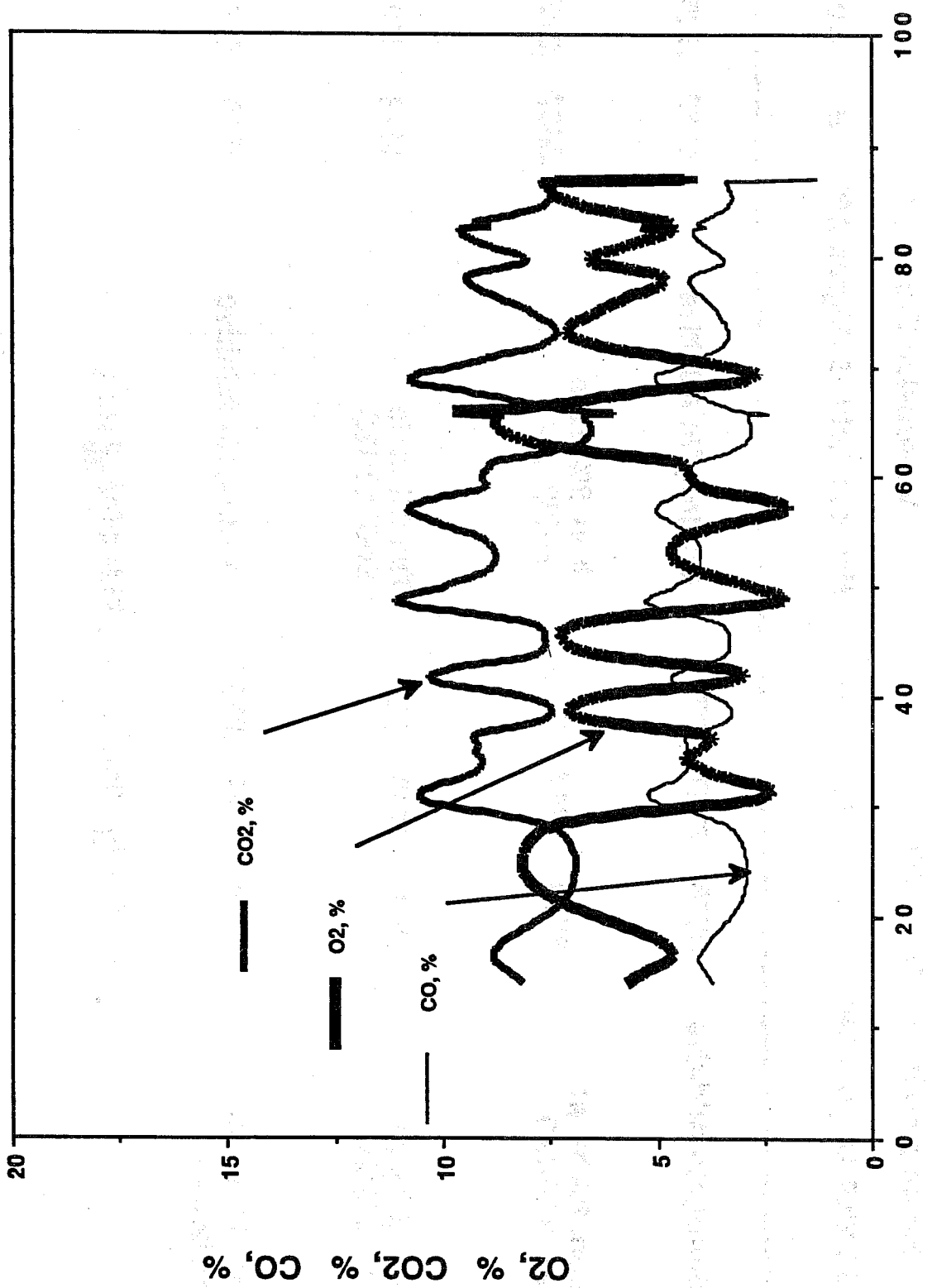


Figure 2.2.1 Venezuelan crude oil control run

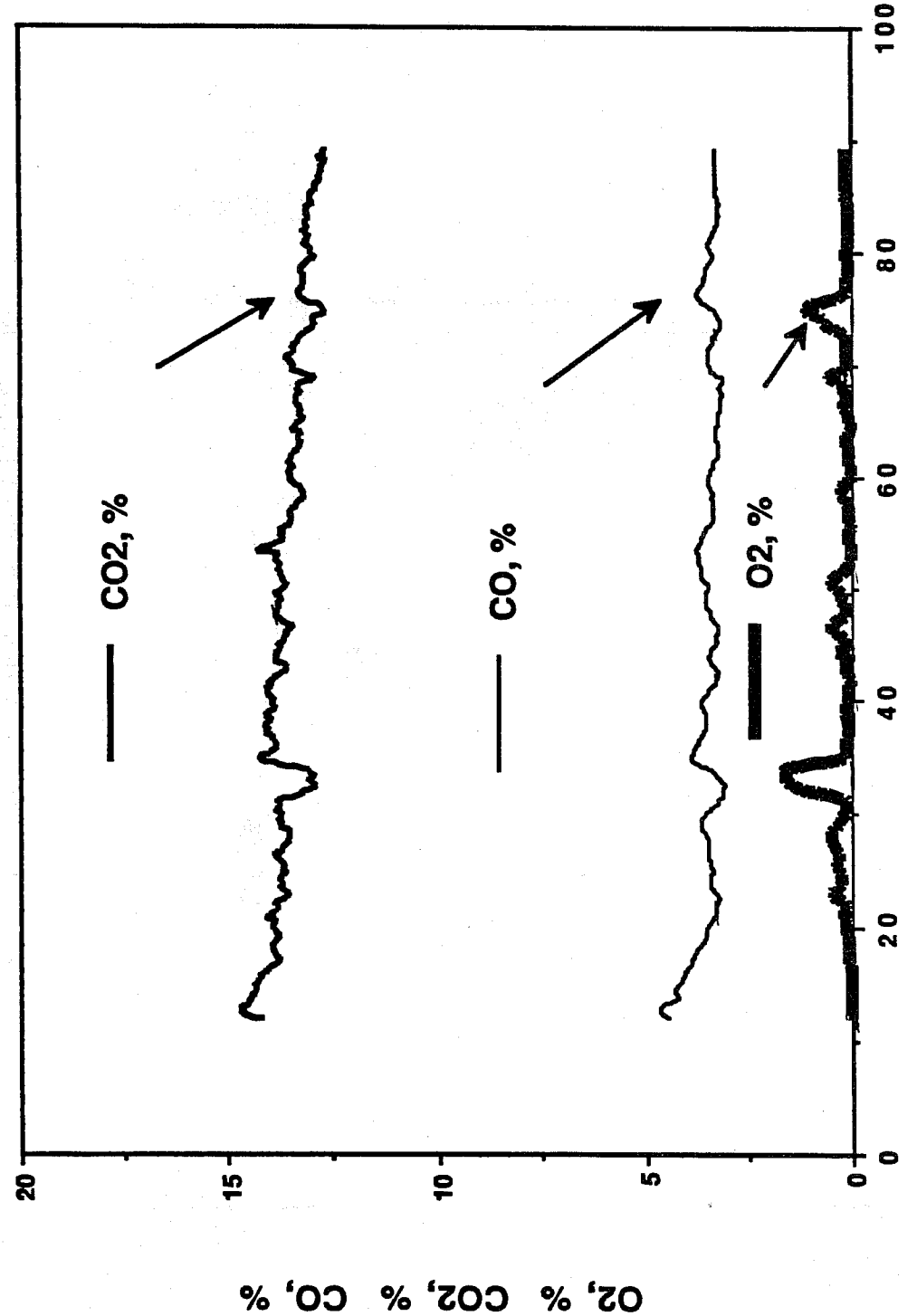


Figure 2.2.2 Venezuelan crude oil with 2% mole frac $FeCl_2$-$4H_2O$

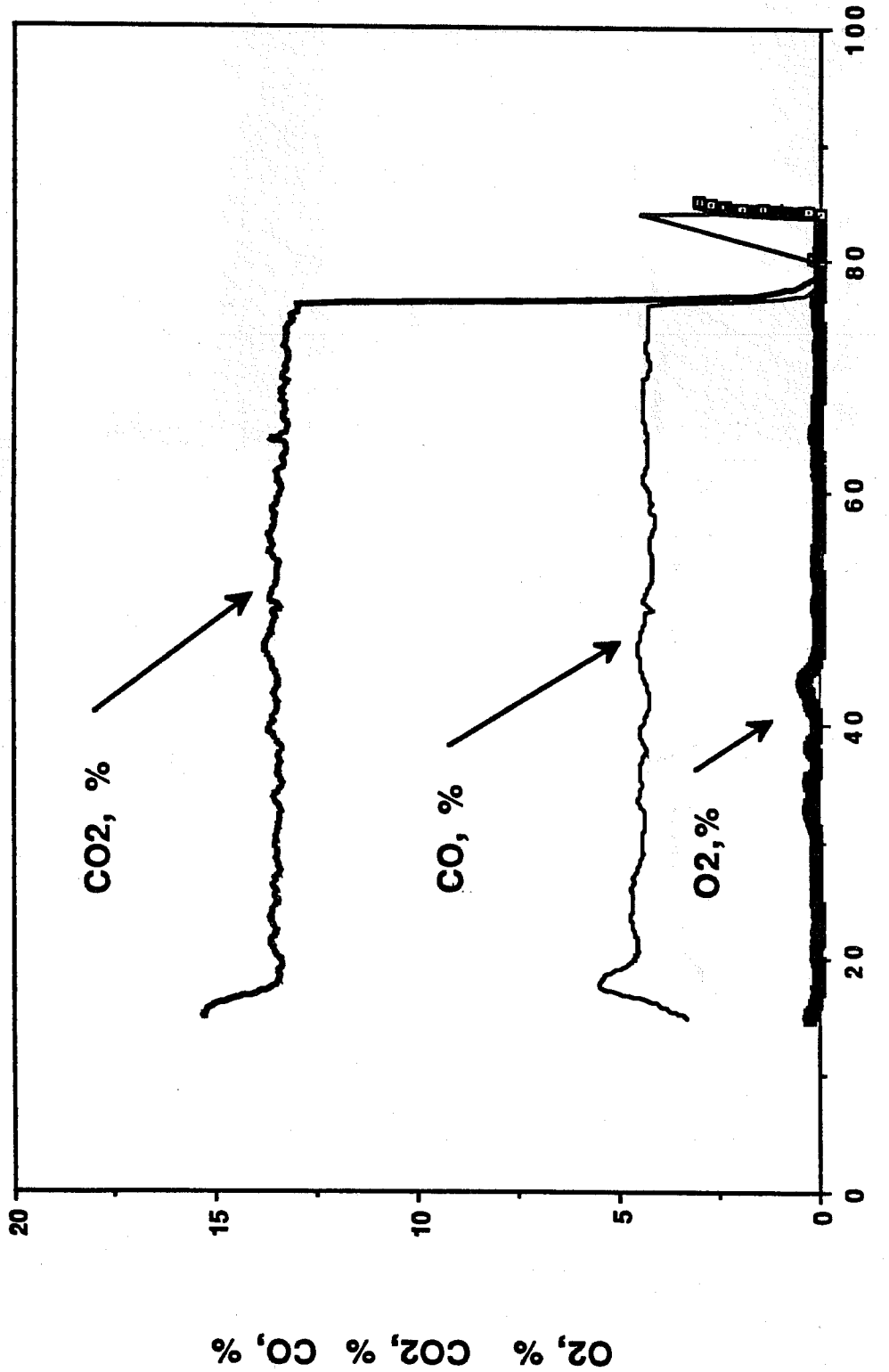


Figure 2.2.3 Venezuelan crude oil with 2% mole frac $SnCl_2$-$2H_2O$

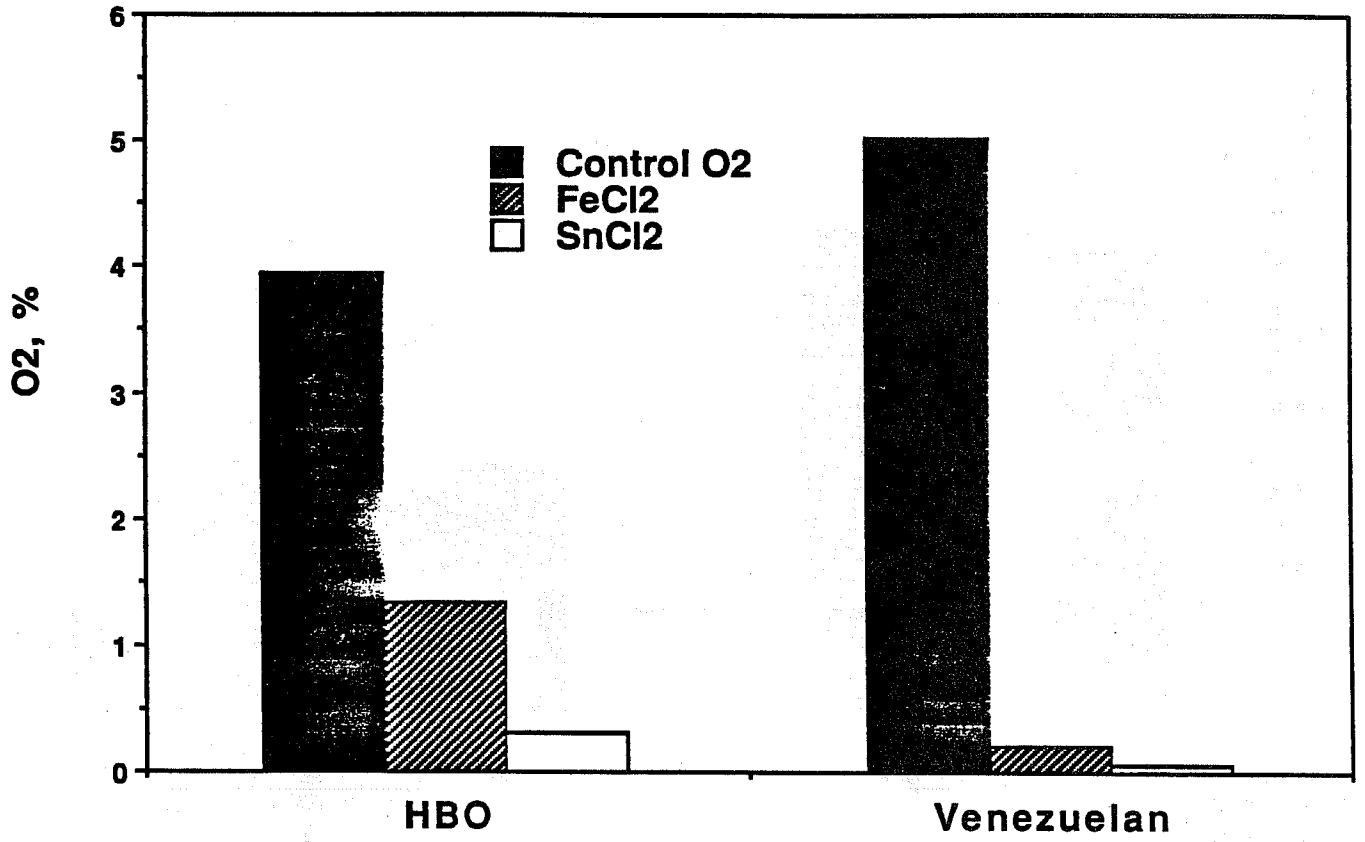


Figure 2.2.4 Average oxygen concentration

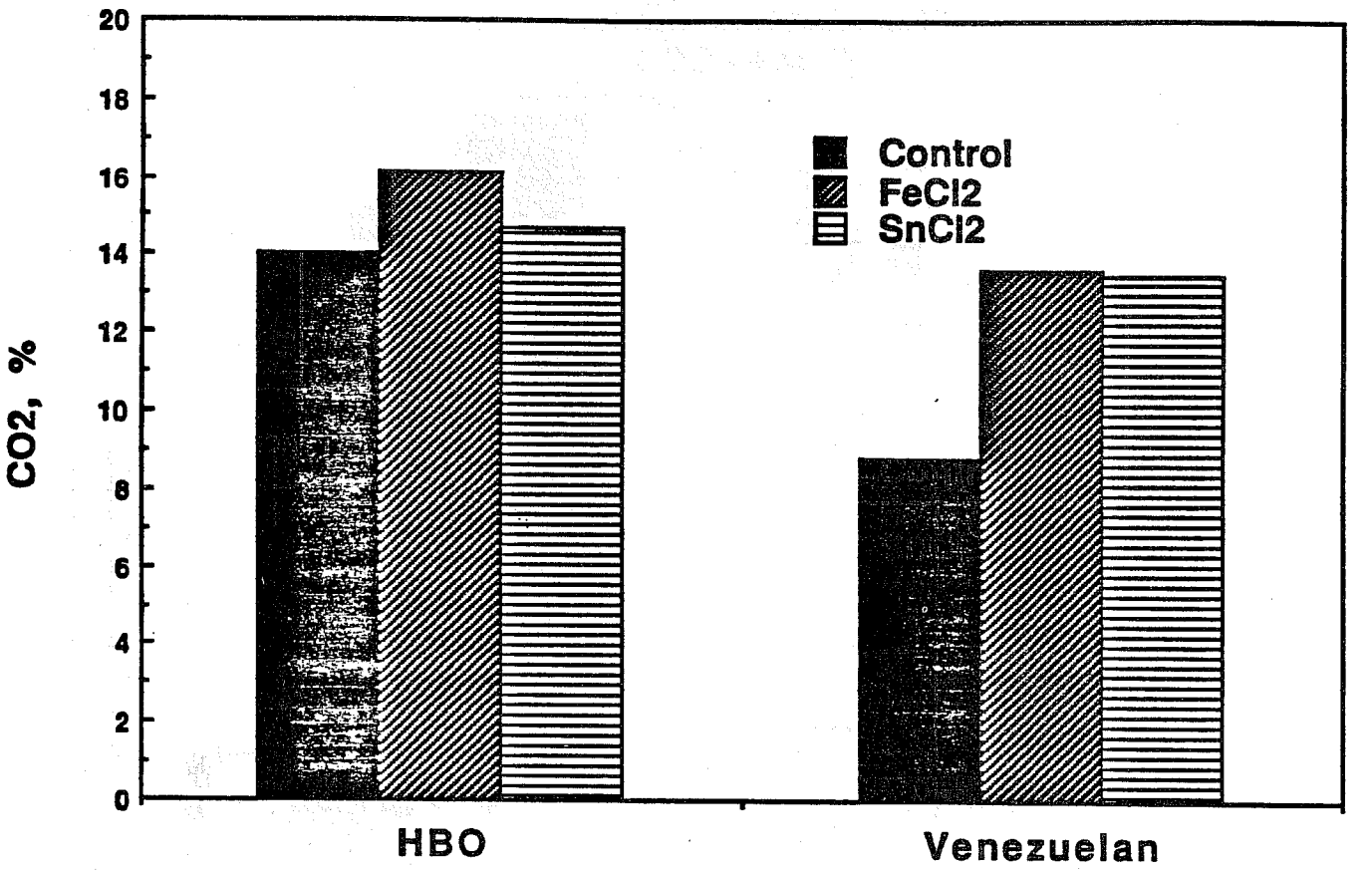


Figure 2.2.5 Average $CO_2$ concentration

$$n = \frac{106.33 + 2\,CO\% - 5.063\,(CO2\% + CO\% + O2\%)}{(CO2\% - CO\%)}$$

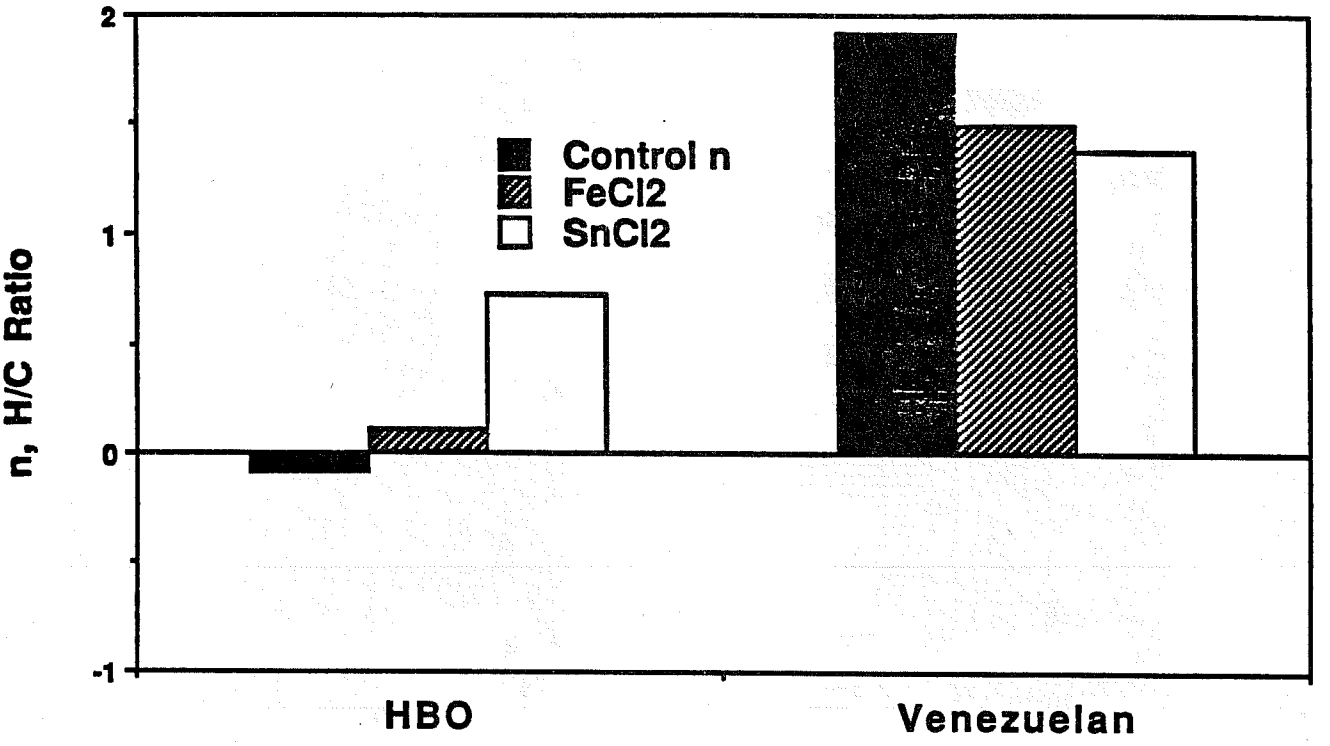


Figure 2.2.6 Average hydrogen carbon ratio

Figure 2.2.7 shows the air required to burn a pound of fuel. This parameter increases for the Huntington Beach oil in the order control, iron and tin and is essentially constant for the Hamaca oil.

The fuel deposited and burned for a cubic foot of reservoir, MR, is graphed on Figure 2.2.8. MR is not affected by the metals for the lighter oil but increases in the order control, iron, tin for the heavier crude.

## 2.2.3 CONCLUSIONS

Tube runs confirm that metallic additives can affect the combustion process, improve the oxygen utilization and the $CO_2/CO$ ratio. The exact nature of the changes observed for the other important field parameters is not fully understood and seems to depend on the nature of the oil. More runs are needed to develop reliable correlations.

## 2.2.4 REFERENCES

1. Baena, C.: "Tube Runs," Annual Report 1988-89, Stanford University Petroleum Research Institute, Stanford, CA., SUPRI TR-67," Report Submitted to the U. S. Dept. of Energy, under Contract No. DE-FG19-87BC14126 (June 1989).

2. Baena, C.: "Effect of Metallic Additives on In-Situ Combustion of Huntington Beach Crude," Engineers Degree Thesis, Stanford University, Stanford, CA (final draft, 1990)

3. De los Rios, C: "The Effect of Metallic Additives on the Kinetics of Oil Oxidation Reactions in In-Situ Combustion," Engineers Degree Thesis, Stanford University, Stanford CA (October 1987). Also available as: "Stanford University Petroleum Research Institute, Stanford CA., SUPRI TR-63," Report Submitted to the U. S. Dept. of Energy, under Contract No. FG19-87BC14126 (November 1988).

4. Shallcross, D. C.: "Modifying In-Situ Combustion Performance by the use of Water-Soluble Additives," SPE Paper 19485, Presented in the Asia-Pacific Conference, Sydney, Australia, (September 13-15, 1989).

$$Faf = \frac{900\ ((2m + 1/m+1) + n/2)}{(12 + n)}$$

SCF air / lbm fuel
@ 100 % efficiency

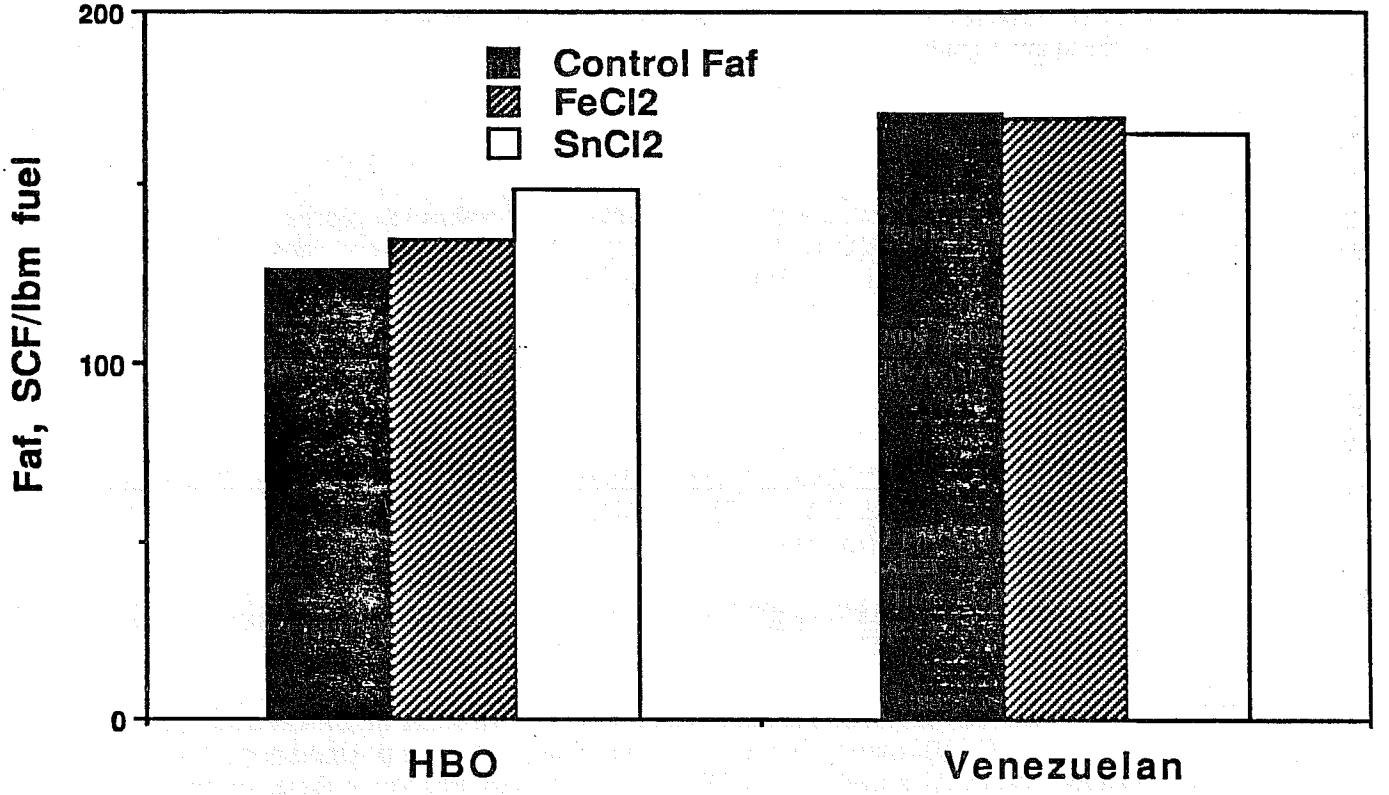


Figure 2.2.7 Average air fuel ratio

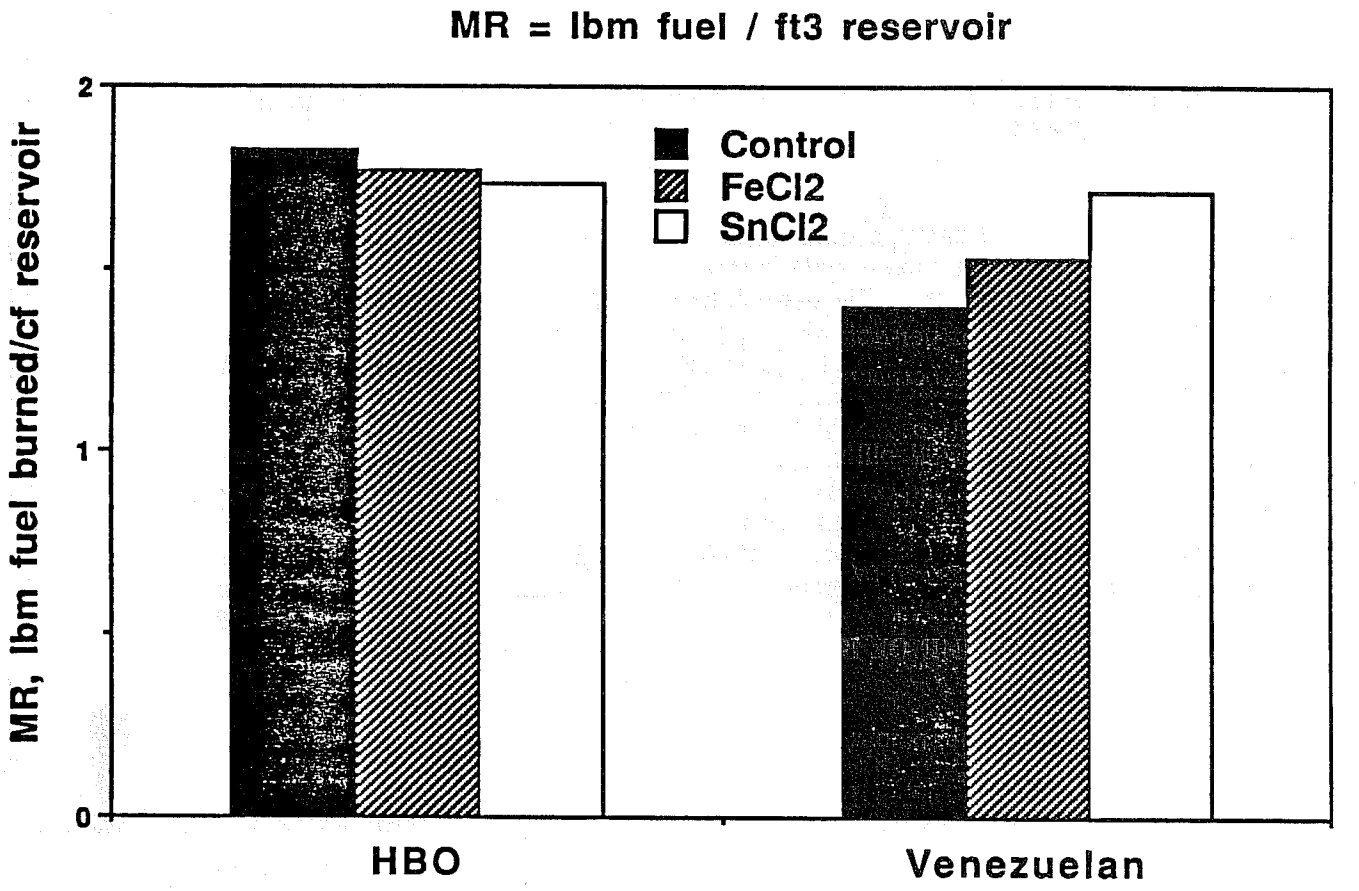


Figure 2.2.8 Average fuel burned per cubic ft. of reservoir

## 2.3 DEVICES AND METHODS FOR IN-SITU COMBUSTION IGNITION (D. C. Shallcross)

A technical report titled "Devices and Methods for In-Situ Combustion Ignition," SUPRI TR 69, by D.C. Shallcross was published in August 1989. The following is a summary of this report.

One of the most important tasks during a fireflood is to ensure the ignition of the oil-bearing stratum efficiently and safely. Many different devices have been developed and employed to achieve this aim. The target zone may ignite spontaneously upon injection of an oxygen-containing gas without the aid of special equipment. Alternatively, ignition may be hastened or enhanced by the use of gas-fired downhole burners, catalytic heaters, electric downhole heaters, or other, chemical means. Other methods involve increasing the reactivity of the formation contents by doping the stratum with compounds that ignite and burn more readily than the reservoir oil. This report surveys the range of ignition methods and devices that have been developed and applied in the field. Not only are successful ignition systems discussed, but also those designs that failed to ignite a formation. In discussing the various techniques, factors considered include reliablility, specialized equipment and materials requirements, and safety. Another consideration is whether a system or device may be easily reused if ignition is not successful on the first attempt. The use of oxidizing gases other than air is also discussed.

## 2.4 CORRELATION OF STEAMFLOOD RESIDUAL OIL SATURATION AND FUEL CONCENTRATION FOR IN-SITU COMBUSTION (D. D. Mamora and K. T. Lim)

In a steamflood four characteristic zones advance radially outwards -- the steam zone drives a condensed hot water zone, which in turn drives a cold water front and reservoir oil. In essence a cold waterflood and then hot waterflood precedes the steam zone.

Steam distillation is the main mechanism in reducing the residual oil saturation which is left behind the hot waterflood. Distillation of the in-situ crude oil causes the produced oil to contain a higher portion of light components than the original oil. An increase in the API gravity by 2 to 3 degrees has been observed both during laboratory experiments[1,2] and field tests[3,4,5]. Consequently, the residual oil in the steam zone has an increasing content of heavier components[6].

Many mathematical models and methods of calculating steamflood oil recovery have been formulated[1,7–13]. All models or methods, however, treat the residual oil saturation due to steamflood as a known parameter. Its value should preferably be determined from representative laboratory steamflood experiments[1,14]. In the absence of laboratory data or a systematic approach for estimating the value of steamflood residual oil saturation, assumptions are made. Average values of 12 to 15% have been used[8,11–13,15] in various studies.

While most literature focuses on the factors affecting recovery efficiency of steam flooding and the planning, implementation and performance of steamflood projects, little attention has been paid to the oil that was left behind. Although the quantity of residual oil due to various factors has been reported, these values are unique to each porous media and oil for which the values were obtained. In the absence of laboratory data, it appears that there is no general approach for estimating residual oil saturation after steamflood, taking into consideration rock and fluid (both oil and steam) properties. Konopnicki et. al.[3] estimated by material balance in the case of Shiells Canyon field steamflood project that the residual oil API gravity decreased to 25.6° compared to 35.2° for the initial oil. While other authors mentioned that residual oils were analyzed, no quantitative data appears to be available.

If the nature of the residual oil changes, so must that of the produced oil. If the residual becomes heavier, the displaced oil must become lighter. This fact has been documented in reported field test results. It is also apparent in laboratory tube run experiments. This sort of information has not been used in interpretation of results or for operational control to our knowledge. A major objective of this study will be to determine the information available from changes in quality of produced oil (compared to the initial oil). Existing laboratory and field data will be interpreted in the light of the findings.

Information regarding the amount and nature of residual oil due to steamflooding can be extended to the estimation of the amount of fuel available for in-situ combustion. During an in-situ combustion process, the mechanism ahead of the combustion region closely resembles a steamflooding process[2] where a steam plateau propagates behind a condensing hot water front, a cold water front and the reservoir oil being driven, in that order.

## 2.4.1 OBJECTIVES

This project has the following main objectives:

1. To develop a general procedure to estimate the amount and nature of residual oil due to steamflooding as a function of oil and rock properties,

2. To correlate steamflood residual oil saturation with fuel concentration for in-situ combustion, and

3. To verify the correlations experimentally.

## 2.4.2 GENERAL OUTLINE OF RESEARCH

The proposed research will be carried out in several stages.

1. Literature search and correlation of available data:
   The literature search will cover four main areas of interest:

   (a) laboratory experiments on hot-water and steam floods,
   (b) field data on hot-water and steam floods,
   (c) laboratory combustion tube runs, and
   (d) field data on in-situ combustion.

   All relevant information will be collated and analyzed to attempt to reach a general approach in correlating or calculating steamflood residual oil saturation and quality. New experimental work, as discussed in the following, may be necessary.

   An attempt will be made to correlate the steamflood residual oil saturation and quality with the amount and quality of fuel burned during an in-situ combustion process. All available tube run data will serve as the initial database. At the same time, methods of computing the expected produced oil quality for an in-situ combustion process will be investigated.

2. Experimental studies:

   Two separate experimental studies are expected:

   (a) A one-dimensional model will be used to study how various oil and rock properties affect the residual oil saturation for a steamflood. API gravity and composition of the residual oil will be analyzed.

   (b) Combustion tube runs will be made to investigate the amount and nature of fuel burned and the quality of produced fluid, and to serve as basis for verifying current correlations and for developing new ones.

   If feasible, computer-aided tomography (CAT) scanning will be used to measure oil saturations in both experiments.

The experiments will involve the use of:

(a) porous media of varying permeability, porosity, gas and water saturations, clay and other mineral contents, and

(b) crude oil of various type, both in terms of API gravity and composition i.e., differing paraffin, aromatic and asphaltene ratios.

3. Simulation Studies:

The possibility of calibrating a PVT and/or multi-component thermal simulator with laboratory data will be attempted. Numerical experiments will be performed to investigate the importance of various parameters used in the correlations as described in (1) and (2).

## 2.4.3 REFERENCES

1. Willman, B. T., Valleroy, V. V., Runberg, G. W., Cornelius, A. J. and Powers, L. W., "Laboratory Study of Oil Recovery by Steam Injection", J. Pet. Tech., (July 1961), 681-690.

2. Wu, C. H. and Fulton, P. F., "Experimental Simulation of the Zones Preceeding the Combustion Front of An In-situ Combustion Process", Soc. Pet. Eng. J., (March 1971), 38-46.

3. Konopnicki, D. T., Traverse, E. F., Brown, A. and Diebert, A. D., "Design and Evaluation of the Shiells Canyon Field Steam-Distillation Drive Pilot Project", J. Pet. Tech., (May 1979), 546-552.

4. Valleroy, V. V., Willman, B. T., Cambell, J. B. and Powers, L. W., "Deerfield Pilot Test of Recovery by Steam Drive", J. Pet. Tech, (July 1967), 956-964.

5. Volek, C .W. and Pryor, J. A., "Steam Distillation Drive - Brea Field, California", J. Pet. Tech., (August 1972), 899- 906.

6. Burger, J., Sourieau, P. and Combarnous, M., "Thermal Methods of Oil Recovery", Editions Technip, Paris, (1985), 106-107.

7. Marx, J. W. and Langenheim, R. N., "Reservoir Heating by Hot Fluid Injection", Trans. AIME, Vol. 216, (1959), 312-315.

8. Farouq Ali, S. M., "Oil Recovery by a Steamflood in a Waterflooded Reservoir", Prod. Monthly, (September 1966), 4-8.

9. Davies, L. G., Silberberg, I. H. and Caudle, B. H., "A Method of Predicting Oil Recovery in a Five-spot Steamflood", J. Pet. Tech., (September 1968),1050-1058.

10. Fairfield, W. H., "How To Quickly Estimate Steam Drive Recovery", World Oil, (March 1968), 74-78.

11. Myhill, N. A. and Stegemeier, G. L., "Steam Drive Correlation and Prediction", J. Pet. Tech., (February 1978), 173-182.

12. Gomaa, E. E., "Correlations for Predicting Oil Recovery by Steam Flood", J. Pet. Tech., (February 1980), 325-332.

13. Jones, J., "Steam Drive Model for Hand-held Programmable Calculators", J. Pet. Tech., (September 1981), 1583-1598.

14. Van Lookeren, J., "Calculation Methods for Linear and Radial Steam Flow in Oil Reservoirs", Soc. Pet. Eng. J., (June 1983), 427-439.

15. National Petroleum Council, "Enhanced Oil Recovery: An Analysis of the Potential for EOR from known Fields in the United States - 1976 to 2000", NPC, Washington, D.C., (1976), 177.

## PROJECT 3: STEAM WITH ADDITIVES

The purpose of this project is to develop an understanding of the mechanisms of the process using commercially available surfactants for reduction of gravity override and channeling of steam. Modeling foam flow in porous media is emphasized because foaming agents have shown promise both in the laboratory and in the field as steam additives.

# 3.1 ANALYSIS OF TRANSIENT FOAM FLOW IN 1-D POROUS MEDIA WITH COMPUTED TOMOGRAPHY
(D. Liu)

Transient behavior is likely to dominate over most of the duration of a foam injection field project. Due to the lack of experimental data, little is presently known about foam flow transient behavior. Foam flow does not follow estabished models such as the Buckley Leverett theory and no general predictive model has been derived. Therefore, experimental data are badly needed. Transient foam flow is being studied in a simple linear porous medium.

Foam is injected at a constant volume rate into a one-dimensional sandpack of 1-inch diameter and 24-inch length, initially saturated with distilled water. The system is placed in a CAT-Scanner. Data are accumulated at low temperature and pressure including the pressure field and saturations obtained by scanning. The liquid saturation can be obtained at each point of a cross section of the pack with less than 1% error over the range of interest. Calculations from the numbers obtained from the scanner show that the best spacial resolution available is a volume element (voxel) of $0.5 \times 0.5 \times 5$ mm. Hence a relationship can be found between saturation and pore volume injected for each location in the sandpack. Pressure profiles show that the pressure drop along the sandpack is not evenly distributed and varies with time. The pressure gradient is much greater between the injection end and the foam front than it is ahead of that front. Moreover, the pressure gradient keeps changing as the foam advances in the sandpack. It is this behavior that differs from standard Buckley-Leverett theory. The cat-scan results demonstrate that foam displacement is not piston-like. Gas channeling appears near the front, and eventually the foam blocks all these channels. The foam flows through the sandpack, continuously breaking and reforming. It takes several pore volumes of foam injection to reach residual liquid saturation.

The saturation versus pore volumes injected relationships for a given section of the sandpack have been matched with power law formulas. In general the matches are satisfactory, however the exponents and constants in the formulas vary as a function of the position of the section considered. Graphing the data as saturation versus equivalent pore volumes injected reduces the range of these variations but does not eliminate them. We are unable to model this behavior to date.

Techniques of measurement of saturations by X-ray cat-scanning as well as interpretation of CT data will be presented.

## 3.1.1 INTRODUCTION

Gas injection is one of the many enhanced recovery techniques. But gas injection is characterized by high gravity forces and high mobility ratios since gas has lower density and viscosity than reservoir oils. Thus gas injection projects are prone to gravity segregation, channeling and fingering, which cause early breakthrough with much of the oil left behind the displacing front. The most widely used and most successful enhanced oil recovery methods are the various thermal recovery techniques. Cyclic steam injection and steam drives are typically applied to heavy oil reservoirs with good results. Because of high ultimate recovery, steam drives are becoming the dominant thermal recovery technique. One of the biggest problems associated with steam injection is the early breakthrough of steam to production wells before all of the oil has been contacted.

Early steam breakthrough is also caused by the heterogeneity of the reservoir. High permeability streaks within the reservoir may conduct most of the gaseous phase and leave most of the oil within the tight portions of the formation. Obviously anything that would help alleviate one or more of these problems would improve the ultimate recovery of a steam drive.

One promising method to improve these techniques is by the formation of an in-situ foam. According to Marsden,[1] the first publication of any direct importance was a patent awarded to Bond and Holbrook[2] They suggested that foam could be generated in an oil reservoir by consecutive injection of aqueous surfactant solution and gas. They considered foam as a displacing medium for oil which would be less mobile than gas and therefore have a more favorable mobility ratio relative to oil. It was claimed that sweep efficiency for both miscible and immiscible gas drives would thereby be increased.

Foam's high apparent viscosity could improve the mobility ratio, and the blocking ability of foam is useful in reducing the effect of high permeability streaks on premature steam breakthrough. As reported by Lescure and Claridge[3] these beneficial characteristics could also be utilized to improve the efficiency of other enhanced recovery methods, such as carbon dioxide flooding.

Not long after Bond and Holbrook,[2] Fried[4] conducted a number of experiments using foam to displace brine and/or oil from porous media. Fried generated an aqueous foam external to the porous medium, injected a slug of foam into the medium, and then drove this slug along by continuous injection of air. Fried showed that the low mobility of the foam as well as its gas blocking ability contribute to a higher oil recovery and lower gas-oil ratio than with conventional displacement methods.

A prior literature survey conducted by Marsden *et al.*[5] indicated that the prime candidate for a blocking agent in steam drives was foam. Subsequently Chiang *et al.*[6] investigated different surfactants and found that indeed, gravity override of gas could be sharply reduced. They also found that in situ foaming generally increased with surfactant concentration until the critical micelle concentration (CMC) was reached. Additional surfactant beyond the CMC did not affect the foaming process. Wang *et al.*[7] studied the ability of several surfactants to generate foams at actual steam injection temperatures and pressures. They achieved promising results with several foamers despite surfactant degradation due to elevated temperatures. Demiral and Okandan[8] investigated the possibility of using in-situ foam and steam in carbonate formations with the aid of a three dimensional model. Under their stated test conditions, the optimum slug size was found to be 0.12 PV at the surfactant concentration of 1.0%. It was claimed that the foam generation improved the steam front movement and enhanced the heat flow to uninvaded zones, thereby increasing the oil recovery from the model by an order of 10%. Robin[9] performed laboratory work on foaming additives to improve steam drive efficiency. He studied the evolution of foam efficiency from ambient conditions up to 300°C and 100 bars and the effect on foam stability of the presence of residual oil phase. As expected, the foam stability of most surfactants deteriorates when temperature increases. But this negative effect can be reduced by increasing the pH, and by using different additives.

Dilgren *et al.*[10] described reduction of steam mobility by foam in terms of a permeability reduction factor defined as the ratio of the permeability of steam in the presence of foam to the permeability of steam in the absence of foam. They found these factors ranging from 1.0 to 0.025. For their purposes Dilgren *et al.* assumed that the mobility reduction was due to lowered permeability only, and no change in viscosity was considered.

In reality, foam has a measurable viscosity much higher than the viscosity of either its gas or liquid components. Marsden and Khan[11] measured foam viscosities using a modified

Fann VG Meter. They found the foam viscosity increased with increasing quality at a given shear rate. They concluded that foam was a non-Newtonian fluid by virtue of the fact that the apparent viscosity decreased with increased shear rate. Marsden and Khan also found that increasing the surfactant concentration increased the apparent viscosity slightly. Further studies by other researchers include Raza and Marsden,[12] Mitchell,[13] Minssieux,[14] Holbrook et al.,[15] and Treinen.[16]

Although the investigators didn't agree with each other, the conclusion of foam being nonNewtonian seems valid in most of the cases, including different media, different procedures and different surfactants. Moreover, foam most commonly behaved like either a pseudoplastic or a Bingham plastic fluid.

There are as many disagreements on foam flow mechanisms as on foam rheological behavior. Beginning with Holm,[17] attempts have been made to establish the flow paths of gas and liquid when foam is injected into a porous medium. He concluded that foam does not flow as a body even when the liquid and gas were combined and injected as foam. There was no free foam flow; the gas moved through the system by progressively breaking and reforming bubbles through the length of the medium. The liquid was found to move via the interconnected film network of the bubbles. The respective flow rates were a function of the number and strength of the films. The stability and bubble making ability of liquid films (lamellae) has therefore become the crux of many recent studies.

The behavior of foam lamellae in smooth capillary tubes was the subject of a project undertaken by Hirasaki and Lawson.[18] They emphasized the importance of foam texture, or average bubble size in relation to the capillary tube size; foam quality, or the gas volume divided by the total volume; and the surface tension gradients created when surfactant is swept from the front of a bubble to its rear. The most recent work on the subject has dealt with the conditions under which foam bubbles are formed and/or destroyed using simplified models such as a toroidally constricted capillary tube described by Sanchez and Schechter[19] They formulated an expression for the generation rate of foam bubbles based on geometric and fluid properties.

Radke and Ransohoff[20] categorized the mechanisms of foam generation within glass bead packs. The snap-off mechanism was concluded to be the primary mechanism responsible for the formation of a strong foam. They developed a simple model to predict the onset of snap-off.

The stability of foam lamellae as determined by capillary pressure was the subject of a recent study by Khatib *et al.*[21] The destabilization of foam lamellae by oil droplets was observed by Nikolov *et al.*[22] using sophisticated microscopic techniques. They have demonstrated that the surfactant type and concentration directly influence the stability of the three phase emulsion structure.

Hirasaki[23] recently discussed in detail the steam foam process. Castanier[24] gave a summary of the field tests of steam foam. In general, good recovery results were reported.

Mathematical simulation of foam flow has been a goal for a long time. Due to poor understanding of flow mechanisms, the models proposed could only fit a small number of experiments involved. For example, Marfoe *et al.*[25] in simulating foam flow in porous media, described the foam behavior as gas-liquid dispersions. Then they adopted the black-oil model equations for oil-water-gas systems, modifying the gas by considering surfactant concentration and another factor of gas interstitial velocity. However, this model was not validated due to

lack of experimental data.

Most studies have dealt with the steady state operation of foam injection. One approach not yet reported is the investigation of the transient pressure behavior of a foam displacement process. Because many investigators have found that truly steady state conditions cannot be achieved before a considerable amount of foam has been introduced into a porous medium, the transient forces are likely to dominate over most or all of the duration of a field project. This work deals with experimental observations of "transient" foam flow.

### 3.1.2 EQUIPMENT AND PROCEDURES

The equipment was originally designed and used by Treinen[16] for his study of the steady-state apparent viscosity of foam in porous media. Some modifications have been made for the current experiment to investigate the transient behavior of foam flow. One major modification is the addition of CAT (computer aided tomography) into the system.

A simplified system diagram is shown in Figure 3.1.1. Foam of known quality and flow rate was generated from nitrogen and surfactant solution passing through a foam generator simultaneously. The foam was then injected into a sandpack 100% saturated with water. The entire sandpack was placed in the CT gantry on a mechanical moving table. Pressure at various points along the sandpack was recorded. The effluent liquid was collected at the outlet.

The CT system used for this study is an EMI 5005, second-generation (translate-rotate) type scanner. For the basic principles of CT, the interested reader is referred to Morgan.[26] A more detailed description of other parts of the equipment can be found in Treinen's report.[16]

The sand used in the sandpack was 100-120 mesh Ottawa sand which had been acid and base washed. Sand migration was prevented by 200 mesh stainless steel screens at the inlet and outlet, and by in line filters with 60 micron porous elements at the pressure tap fittings.

To minimize variation in foam quality due to expansion of gas, the system was initially run at an elevated downstream pressure of 50 psig. This was achieved by using a backpressure regulator. To measure the absolute pressure along the sandpack eight pressure taps were located at 2, 4, 6, 9, 12, 15, 18, and 21 in. from the inlet (Figure 3.1.2). The inlet and outlet, along with six of the sandpack taps, were connected to differential pressure transducers. The total flowing pressure drop across the sandpack is in the range of 5 psi. The pressure transducers were connected to a constant pressure source of 50 psig allowing the use of 5 psi differential pressure plates in the pressure transducers.

Prior to each experimental run, the pressure transducers were calibrated and the transducer demodulators were adjusted to the appropriate range. Each experimental run was begun with a new sandpack. Dry sand was packed into the tube in an upright position, while vibration and an induced vacuum were used to enhance settling of the sand. Then distilled water was introduced from the bottom of the sandpack to achieve the effect of *wet packing*. After the sandpack was fully saturated with water, $CO_2$ was used to displace the water from the top down. During this entire process, vibration was continued. This process was repeated for a few times before the sand was packed homogeneously. To ensure consistency, each sandpack's porosity and permeability were measured before each run. The porosity was estimated by the weight (volume) of distilled water saturating the sandpack and that of the sand volume. The sandpack was mounted on to the experimental system. More water was pumped in. The permeability of the sandpack was calculated from the pressure drop and the water flow rate.

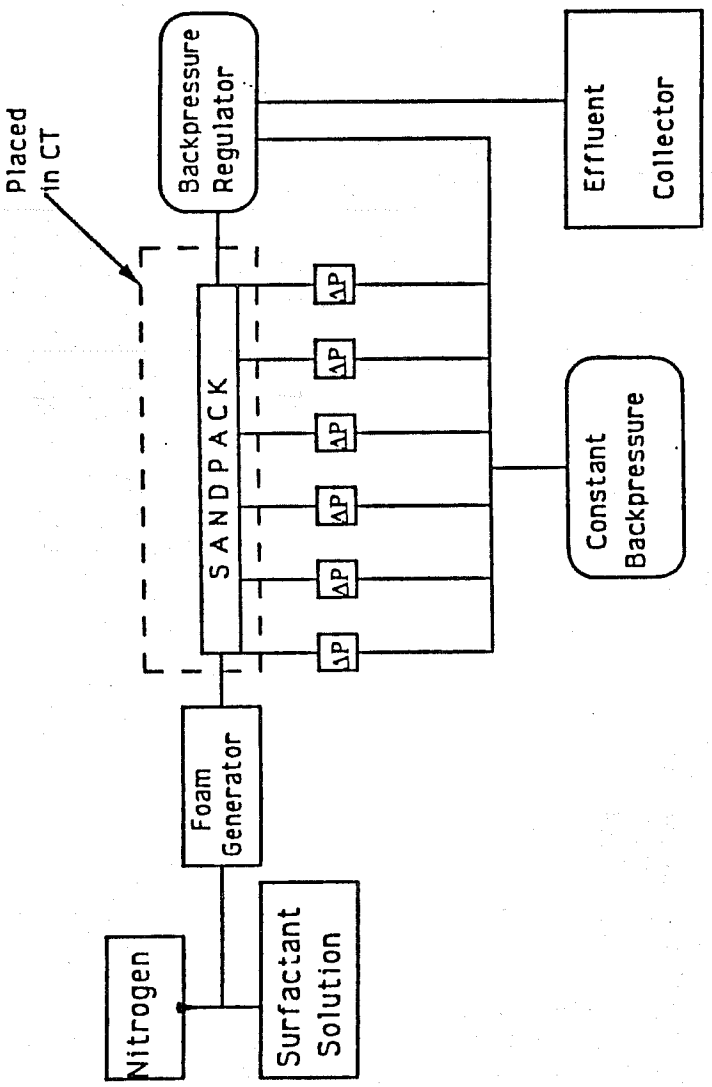


Figure 3.1.1 Simplified system diagram

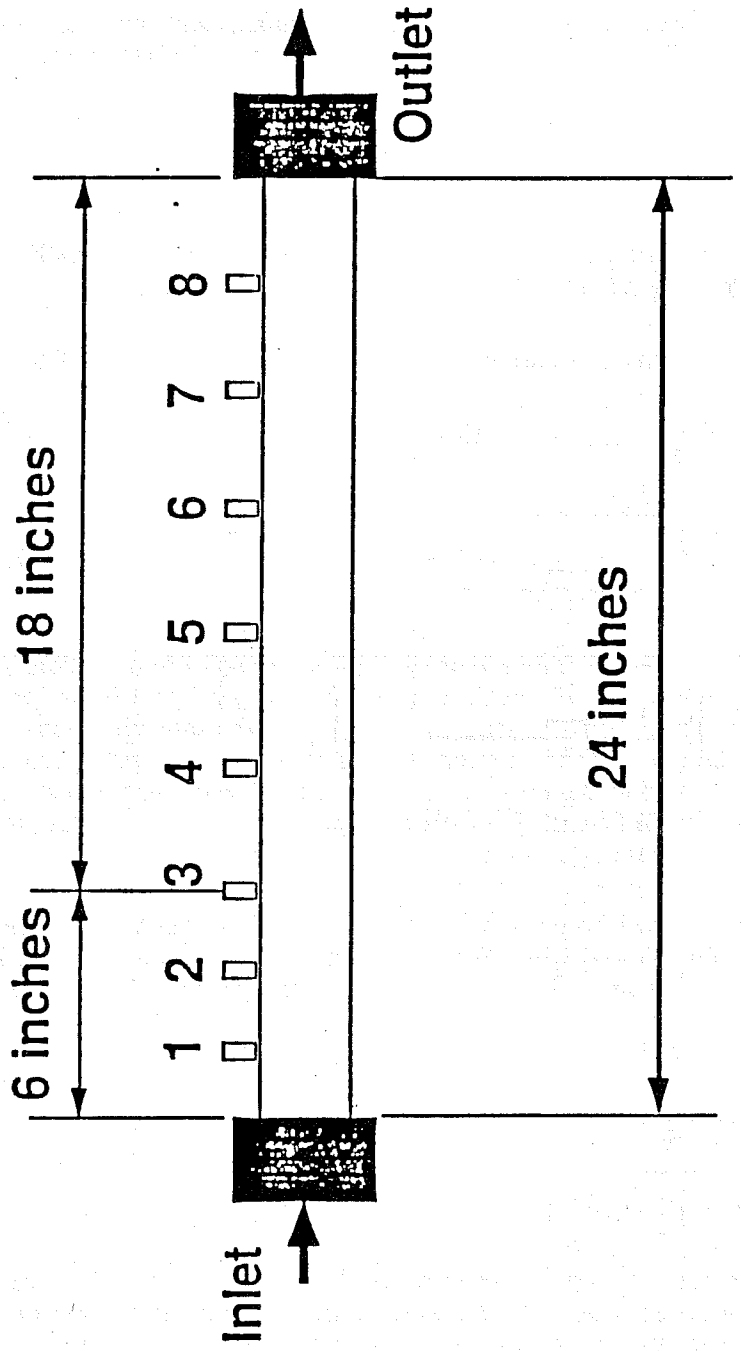


Figure 3.1.2 Sandpack dimensions

Verification of homogeneity in porosity was made by scanning.

The surfactants used in this study were AOS 1618 of ENORDET and Suntech IV.

The sandpack was placed under the CT during the displacement process. For each scan, a CT number was obtained. For this system, the CT number was calculated from:

$$N_{CT} = \frac{\mu_{mat} - \mu_W}{\mu_W} \times 1000 \tag{3.1.1}$$

where $N_{CT}$ is the CT number, $\mu_{mat}$ and $\mu_W$ are the linear attenuation coefficients for the porous material and water, respectively.

The liquid saturation at any cross-section of the sandpack was estimated from:

$$S_l = \frac{N_{CT} - N_{CTg}}{N_{CTl} - N_{CTg}} \tag{3.1.2}$$

where $S_l$ is the liquid saturation. $N_{CTl}$ and $N_{CTg}$ are the CT numbers for the sandpack saturated with water and gas, respectively.

Since each experiment begins with a new sand-pack, several cross sections of the sand-pack were scanned fully saturated with distilled water and analyzed as a basis for future comparisons. Once the experiment starts and foam is flowing into the sand-pack, one cross-section is concentrated upon to be scanned for a period of time to get a CT number-time relationship, which is in turn closely related to the saturation. At the end of each experiment, the foam has completely displaced the distilled water from the sand-pack. A CT scan at this time gives yet another basis for comparison with other scans for intermediate stages.

The CT number is obtained from the computer on an average basis. It is a measure of all the voxels of interest on that cross section. Since it is a statistical average, every CT number is associated with a standard deviation. The greater the standard deviation, the more heterogeneous the cross section; hence the standard deviation is an indication of the amount of gas channelling on that cross section. For this preliminary work no detailed analysis of every voxel of cross section was made on a quantitative basis. However, a good estimate of the saturation distribution can be made directly from the pictures.

### 3.1.3 RESULTS AND DISCUSSION

A summary of the runs to date is presented in Table 3.1.1. As can be seen from the table, the foam quality was set at 90% for all these runs. The foam injection rates were from 0.01 to 1.0 cc/min. The surfactant concentration was either 0.1 or 1.0 weight percent. The absolute permeability of the sandpack varied between 6.5 to 7.0 Darcy. The porosity fell in the range of 32 to 35%.

The pressures measured at the pressure taps were plotted versus distance from the inlet of the sandpack. As an example, the pressure distribution for Run 4 is presented in Figure 3.1.3. The surfactant used for this run was AOS 1618 with a concentration of 1.0%. The foam injection rate was 1.0 cc/min. The circles on the pressure curves indicate the foam front visually

Table 3.1.1 Basic Data for the Experimental Surfactant Steam Runs

Surfactants Used: AOS 1618, Suntech IV
Foam quality: 90%
Pore Volume: 120 cc
Backpressure: 50 psig

| RUN No. | Injection Rates (cc/min) | Surfactant Concentration | K (Darcy) | Porosity (%) |
|---|---|---|---|---|
| 1 | 0.1 | 0.1% | 6.5 | 35 |
| 2 | 0.01 | 0.1% | 7.0 | 35 |
| 3 | 1.0 | 0.1% | 7.0 | 33 |
| 4 | 1.0 | 1.0% | 6.7 | 32 |
| 5 | 1.0 | 1.0% | 6.8 | 33 |
| 6 | 1.0 | 0.1% | 6.6 | 32 |
| 7 | 1.0 | 0.1% | 6.5 | 33 |
| 9 | 1.0 | 0.1% | 6.5 | 32 |
| 10 | 1.0 | 1.0% | 6.9 | 32 |

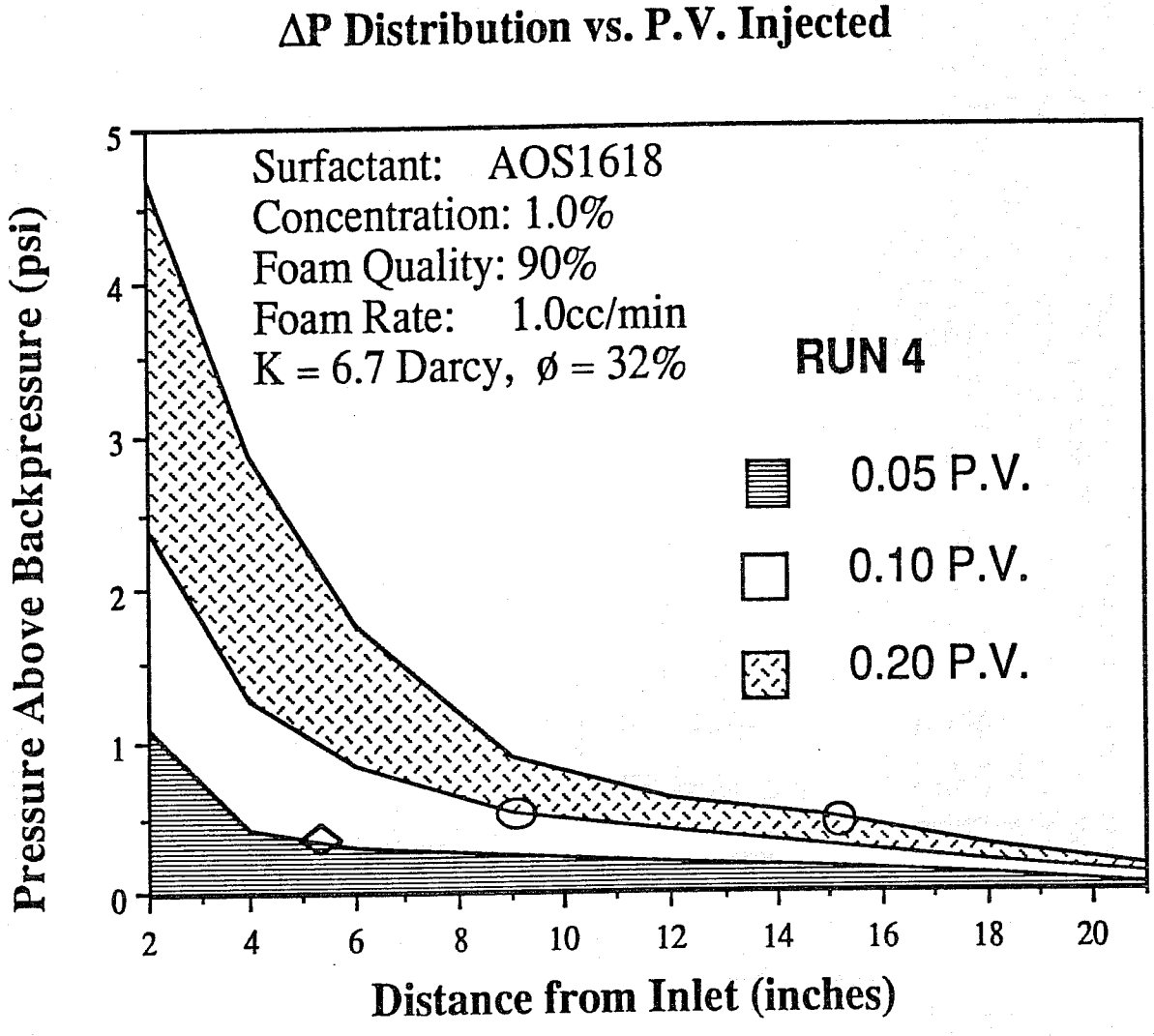


Figure 3.1.3 Pressure distribution at several PV injected (Run 4)

observed from the outside of the sandpack. The pressure profile for Run 9 is presented in Figure 3.1.4 in which the surfactant concentration was 0.1%. From the two figures, one can see that an increase in surfactant concentration produced an increase in pressure drop for the same amount of foam injected. In any case, the pressure gradient behind the foam front is much higher than that ahead of the front. This shows the high apparent viscosity of foam. The pressure gradient increases with the displacement of original fluid with foam. However this relationship is complex and is dependent on many factors.

All the pressure data showed this trend of pressure change. This pressure behavior contradicts standard Buckley-Leverrt displaement. If it had conformed to Buckley-Leverett theory, the pressure gradients behind the front could have been directly related throughout the displacement process. The exact reason why this happens is yet to be discovered. In other words, a simple mathematical model which is descriptive of transient foam flow behavior has not been established. Because of equipment limitations, all runs were stopped when the inlet pressure went over 150 psig.

For each cross section during the experiment, a series of scans were taken at different stages and the CT numbers were obtained from the CT computer. For example, a CT Number-Pore Volumes Injected relationship is shown in Figure 3.1.5 for Run 9 at the cross section location 9 (23 inches from the inlet). To have all the cross sections comparable with one another, a common factor was used. The volume of foam injected was converted into an Equivalent Pore Volume (EPV) which was based on the pore volume from the inlet to the cross section concerned. Naturally, the EPV in the middle of the sandpack is half of the total pore volume and the EPV at the end is the total pore volume. Then Figure 3.1.5 was replotted as Figure 3.1.6 as a CT number-EPV relationship. Comparison of the two plots shows that the use of EPV improves correlation of the data points. Another plot of CT number versus EPV is shown in Figure 3.1.7 for Run 9 at location 1 (1 inch from the inlet). Different locations and experimental conditions give different relationships. As can be seen in Figure 3.1.7, the CT number-EPV relationship was found to be:

$$N_{CT} = 468 \times EPV^{-0.052} \tag{3.1.3}$$

The CT number for gas was 340 and that for water was 560. According to Equations 3.1.2 and 3.1.3:

$$S_l = \frac{N_{CT}}{220} - 1.55 \tag{3.1.4}$$

where $S_l$ is the liquid saturation. Based on Eqs. 3.1.3 and 3.1.4, $S_l$ can be expressed as a function of EPV:

$$S_l = 2.13 \times EPV^{-0.052} - 1.55 \tag{3.1.5}$$

In general, for any cross section at any time $S_l$ can be expressed as:

$$S_l = a \times EPV^b - 1.55 \tag{3.1.6}$$

where $a$ and $b$ are coefficients which will depend on location and experimental conditions such as foam quality, surfactant concentration, foam flow rate, porosity, and permeability.

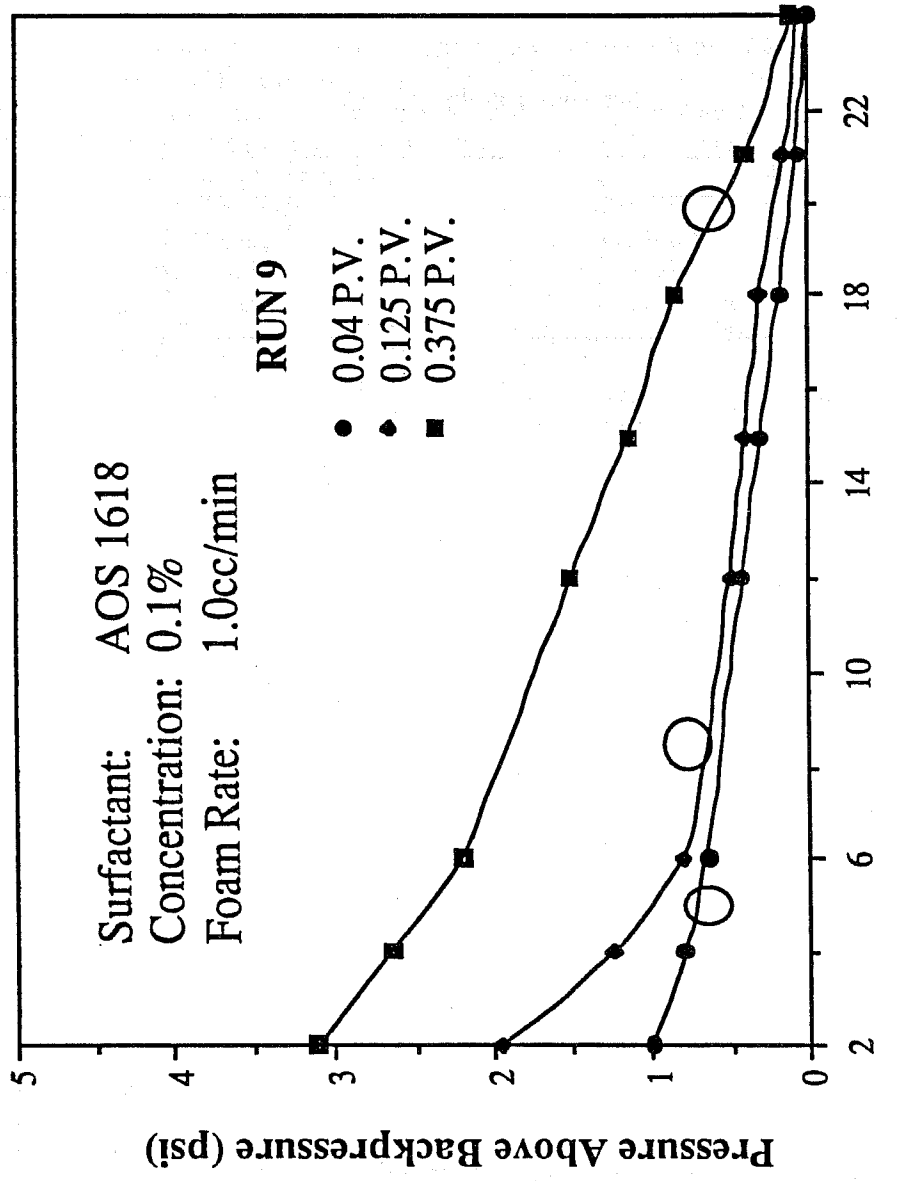


Figure 3.1.4 Pressure distribution at several PV injected (Run 9)

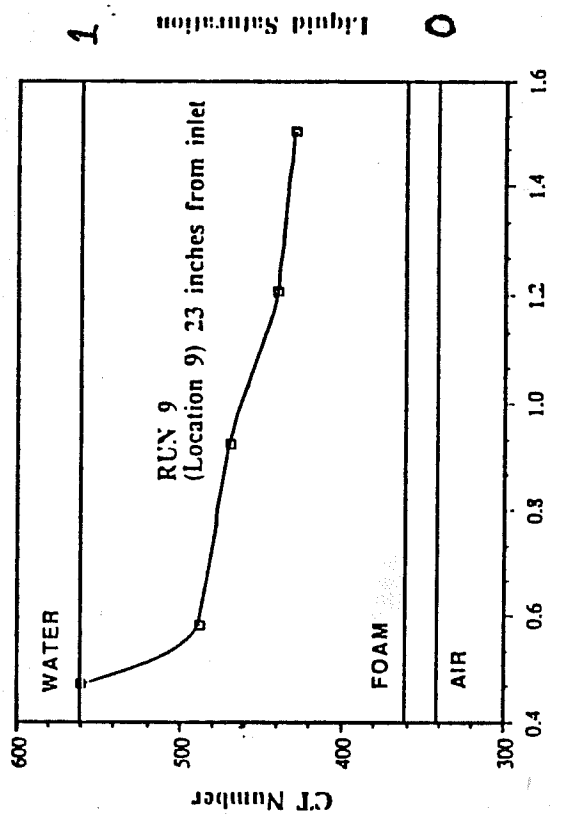


Figure 3.1.5 CT number (liquid saturation) vs pore volume injected (Run 9, Location 9)

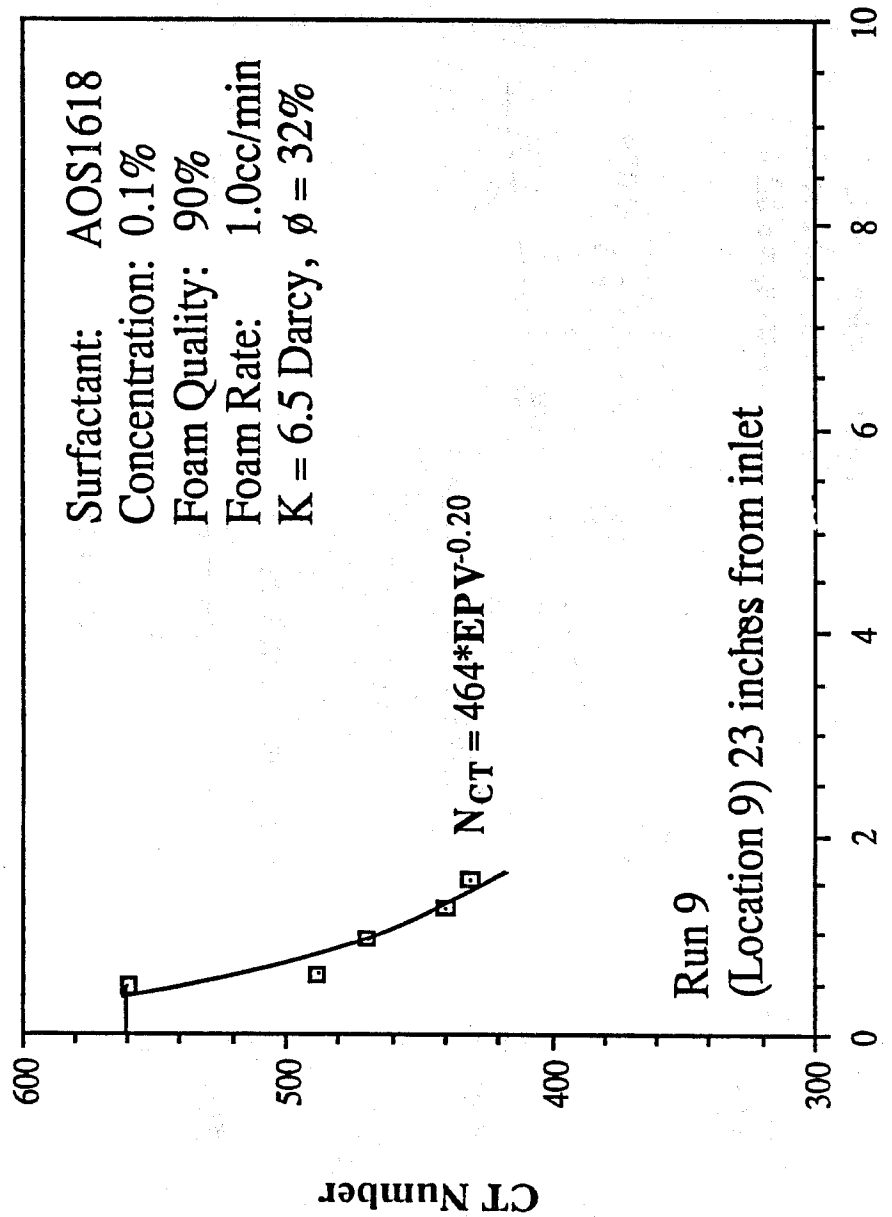


Figure 3.1.6 CT number vs equivalent pore volumes injected (Run 9, Location 9)

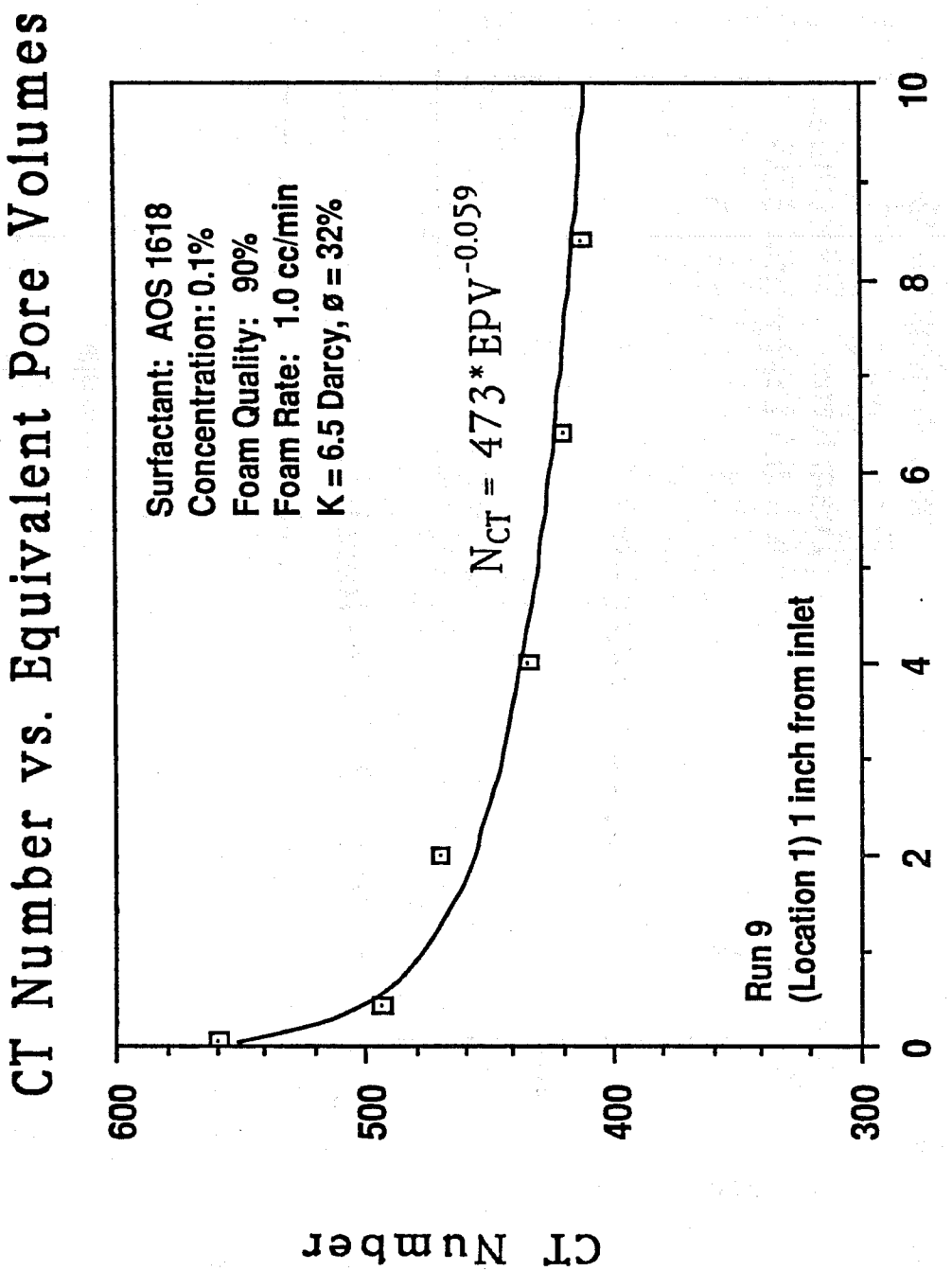


Figure 3.1.7 CT number vs equivalent pore volumes injected (Run 9, Location 1)

The coefficients, $a$ and $b$, vary for different cases. Table 3.1.2 gives a list of some of the coefficients. We are yet unable to obtain a statistically accurate correlation or their coefficients.

The CT numbers given previously were mean values. There was a standard deviation attached to each CT number. A larger standard deviation means a heterogeneous saturation distribution in the cross section. Figure 3.1.8 gives a plot for Run 4 at Location 1 (1 inch from the inlet) with the standard deviation shown as vertical bars for each data point. The standard deviation for fully water- or gas-saturated sandpack was small, indicating that the saturation was homogeneous. When the foam displaced part of in-situ water, the standard deviation became larger, which means that the foam flow was not a piston-like displacement.

Figure 3.1.9 shows a sequence of scans with foam displacing in-situ water at a cross section in Run 10 at location 1 (1 inch from the inlet). In the beginning, the cross section was homogeneous (Figure 3.1.9a) when saturated with water. Foam of 90% quality (1% surfactant concentration) was injected into the sandpack at a rate of 1cc/min. At a later time (6 minutes after start of foam injection), Figure 3.1.9b, gas was starting to invade the cross section. The dark part is gas in the foam. As can be seen, foam flow was not a piston-like displacement. There was fingering and channelling. As time passed, the cross section was filled with foam. Foam block gas channels and displaced the rest of the liquid from the cross section (Figures 3.1.9c and 3.1.9d). At the later stage of displacement, the saturation change slowed. The last two CT pictures are hard to distinguish with naked eyes. The pictures shown have different window level settings. For example, Figure 3.1.9a has a window level of 500. A higher window level gives greater contrast. At 36 minutes (Figure 3.1.9c), foam had displaced almost all the water from the cross section and the scan was too dark to be viewed at a window level of 500. Through experience, 350 was chosen as the new window level for better visualization.

It was found that for the range of surfactant concentration studied (between 0.1 and 1.0 weight %), the higher the surfactant concentration, the better and faster the displacement. For a low concentration, the foam in the front broke and did not reform due to adsorption of the surfactant on the porous medium. In this case, gas fingering was severe and gas breakthrough was faster. A complete displacement required more pore volume throughput of foam. The foam flow rate played an important role in displacing the in-situ fluid from the sandpack. The higher the flow rate, the more piston-like was the displacement.

### 3.1.4 CONCLUSIONS

Some conclusions are:

- Computerized Tomography has proved to be a useful tool in the study of foam flow in porous media.
- The transient foam behavior differs from standard Buckley-Leverett displacement theory. The pressure gradient behind the foam front increased with foam throughput.
- The higher the surfactant concentration, the greater the pressure gradient for the concentrations studied.
- Gas channelling occurs in the foam front. It is not valid to assume a piston-like behavior.

Table 3.1.2 List of Some of the Coefficients in Foam Displacement Equations

| RUN No. | Location No. | Distance from inlet (inches) | a | b |
|---|---|---|---|---|
| 3 | 1 | 1 | 1.96 | -0.036 |
| 4 | 4 | 7.5 | 2.82 | -0.320 |
| 5 | 1 | 1 | 2.53 | -0.039 |
| 6 | 5 | 10.5 | 2.41 | -0.290 |
| 7 | 9 | 23 | 2.11 | -0.200 |
| 9 | 1 | 1 | 2.13 | -0.052 |

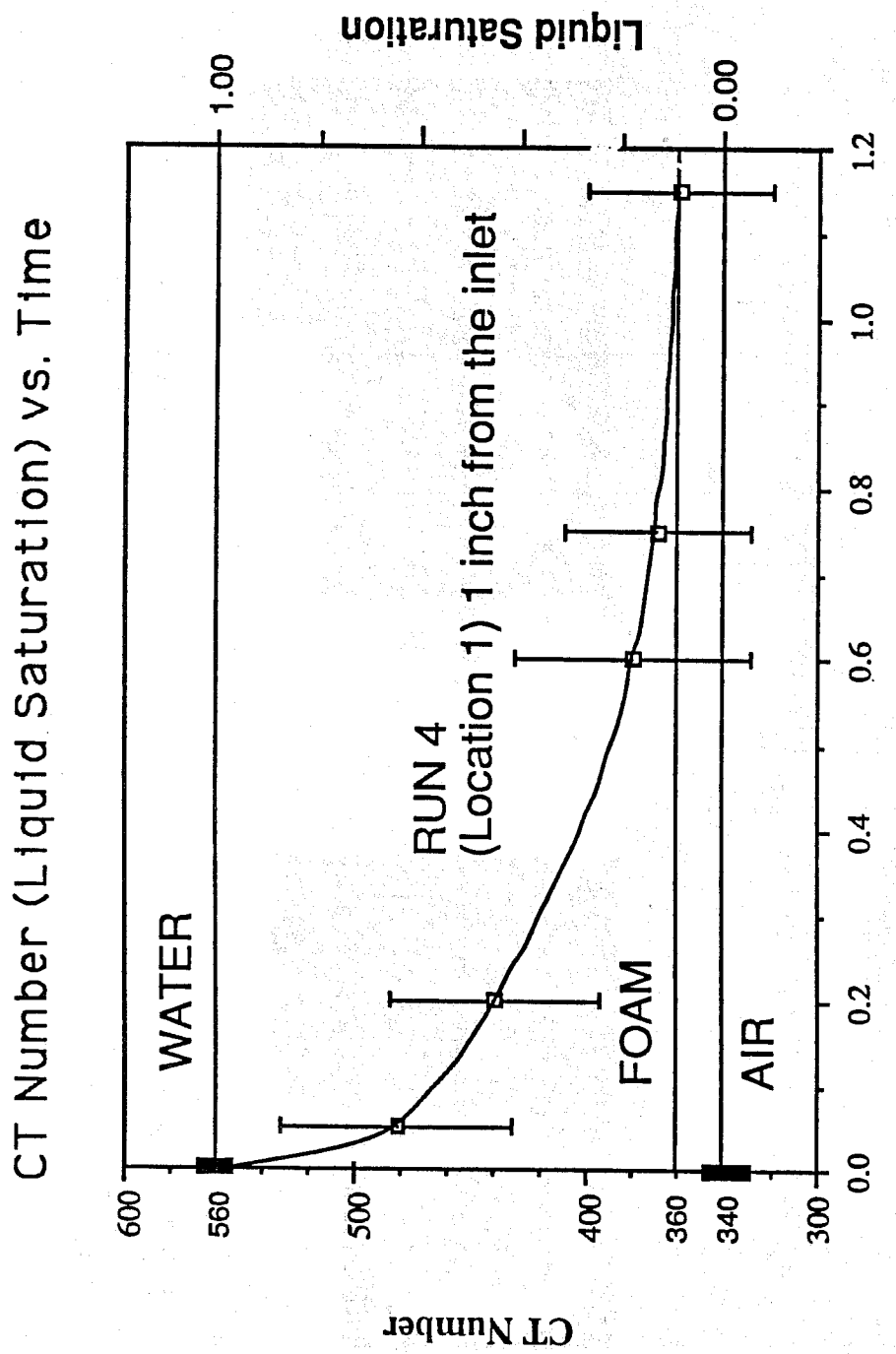


Figure 3.1.8 CT number (liquid saturation) vs PV injected (Run 4, Location 1)

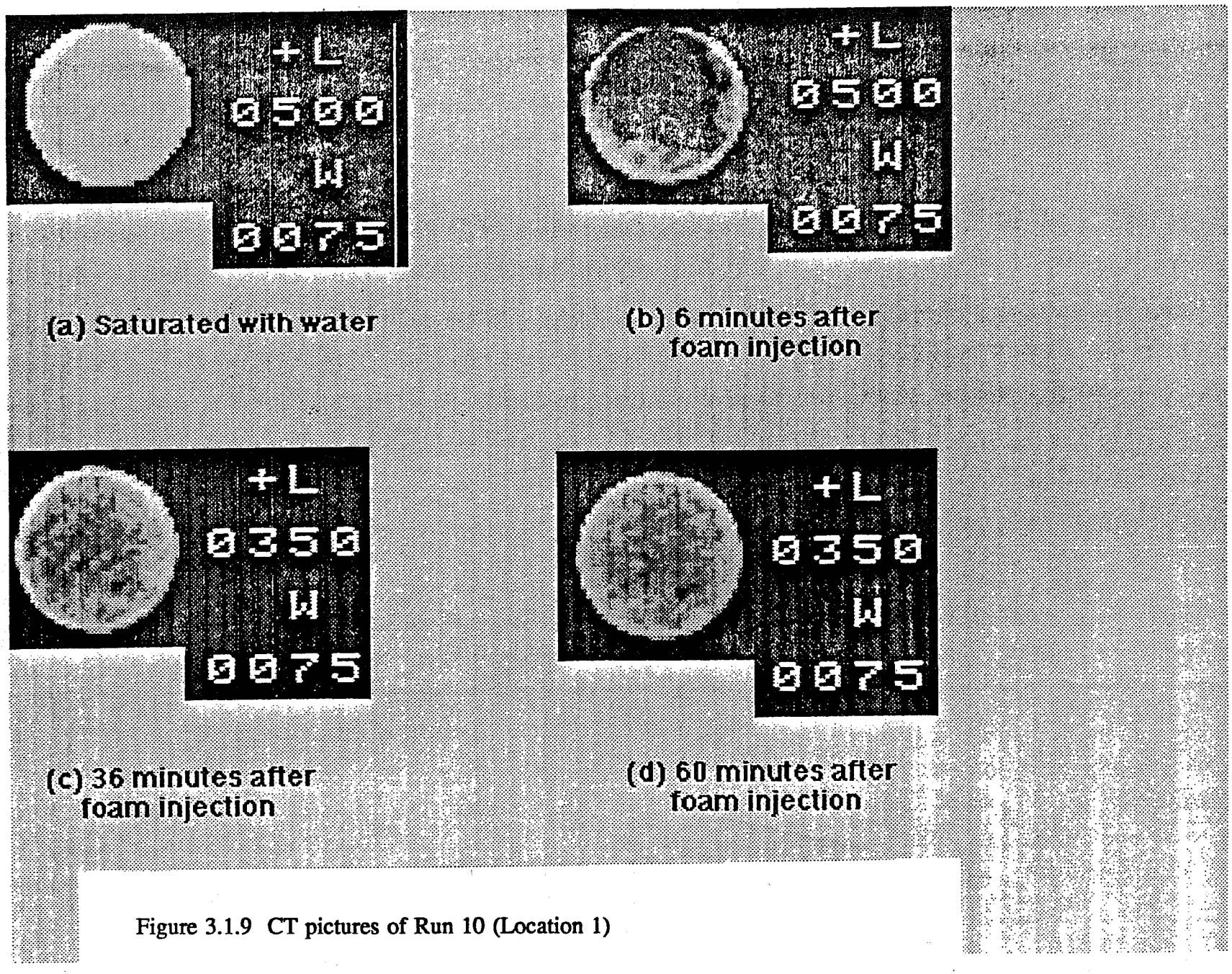


Figure 3.1.9 CT pictures of Run 10 (Location 1)

- The mechanism of foam propagation seems to be initial gas channelling, progressively becoming more uniform as foam blocks the channels.

- More experimental data is needed to help establish a satisfactory model.

### 3.1.5 NOMENCLATURE

$a$ a constant coefficient
$b$ a constant coefficient
$EPV$ Equivalent Pore Volume
$K$ absolute permeability, Darcy
$N_{CT}$ CT number
$N_{CTg}$ CT number for gas
$N_{CTl}$ CT number for liquid
$S_l$ liquid saturation
$\mu_{mat}$ linear attenuation coefficient for porous material
$\mu_w$ linear attenuation coefficient for water

### 3.1.6 REFERENCES

1. Marsden, S.S.: "Foams in Porous Media". US DOE Report No. DE-AC03-81SF11564, May 1986.

2. Bond, D.C. and Holbrook, O.C.: "Gas Drive Oil Recovery Process." U.S. Patent No. 2,866,507, (1958).

3. Lescure, B.M. and Claridge, E.L.: "$CO_2$ Foam Flooding Performance vs. Rock Wettability". Paper SPE 15445 presented at the SPE 61st Annual Technical Conference and Exhibition, New Orleans, Oct. 5-8, 1986.

4. Fried, A.N.: "The Foam Drive Process for Increasing the Recovery of Oil." USBM Report of Investigations 5866, 1961.

5. Marsden, S.S., Elson, T., and Guppy, K.: "Literature Review of the Selective Blockage of Fluids in Thermal Recovery Projects". SUPRI-TR-3, Stanford U. Petroleum Research Inst., Stanford, CA, (Dec. 1977).

6. Chiang, J.C., Sanyal, S.K., Castanier, L.M., Brigham, W.E., and Sufi, A.: "Foam as a Mobility Control Agent in Steam Injection Processes". Paper SPE 8912 presented at the SPE 50th Annual California Regional Meeting, Los Angeles, April 9-11, 1980.

7. Wang, P.F., Al-Khafaji, A., and Castanier, L.M.: "Steam-surfactant systems at reservoir conditions". DOE Fossil Energy Report No. CONF-820712, (July 1982)216-226.

8. Demiral, M.R.B. and Okandan, E.: "Experimental Analysis of Steam Foam Injection to Heavy Oil Limestone Reservoirs". Paper SPE 15734 presented at the Fifth SPE Middle East Oil Show, Manama, Bahrain, March 7-10, 1987.

9. Robin, M.: "Laboratory work on Foaming Additives to Improve Steam Drive Efficiency". Paper Presented at the 3rd European Meeting on Improved Oil Recovery, Roma, Italy, April 16-18, 1985.

10. Dilgren, R.E., Deemer, A.R., and Owens, K.B. "The Laboratory Development and Field Testing of Steam Noncondensible Gas Foams for Mobility Control in Heavy Oil Recovery". Paper SPE 10774 presented at the 52nd Annual California Regional Meeting, San Francisco, March 24-25, 1982.

11. Marsden, S.S. and Khan, S.A.: "The Flow of Foam Through Short Porous Media and Apparent Viscosity Measurements". Soc. Pet. Eng. J., (March 1966) 17-25.

12. Raza, S.H. and Marsden, S.S.: "The Streaming Potential and Rheology of Foam". Soc. Pet. Eng. J., (Dec. 1967) 359-368.

13. Mitchell, B.J.: "Viscosity of Foam". PhD dissertation, U. of Oklahoma, Norman, (1969).

14. Minssieux, L.: "Oil Displacement by Foams in Relation to Their Physical Properties in Porous Media". J. Pet. Tech., (Jan. 1974) 100-108.

15. Holbrook, S.T., Patton, J.T., and Hsu, W." "Rheology of Mobility Control Foams". Paper SPE 9809 presented at the SPE DOE Second Joint Symposium on Enhanced Oil Recovery, Tulsa, OK, April 5-8, 1981.

16. Treinen, R.J.: "Apparent Viscosity Measurements of Surfactant Foam in Porous Media". M.S. Report, Stanford U., Stanford, CA, (1985).

17. Holm, L.W.: "The Mechanism of Gas and Liquid Flow Through Porous Media in the Presence of Foam". Soc. Pet. Eng. J., (Dec. 1968) 359-369.

18. Hirasaki, G.T. and Lawson, J.B.: "Mechanism of Foam Flow in Porous Media - Apparent Viscosity in Smooth Capillaries". Paper SPE 12129 presented at the SPE 58th Annual Technical Conference and Exhibition, San Francisco, Oct. 5-8, 1983.

19. Sanchez, J.M. and Schechter, R.S.: "The Effect of Trace Quantities of Surfactant on Nitrogen Water Relative Permeabilities". Paper SPE 15446 presented at the SPE 61st Annual Technical Conference and Exhibition, New Orleans, Oct. 5-8, 1986.

20. Radke, C.J. and Ransohoff, T.C.: "Mechanisms of Foam Generation in Glass Bead Packs". Paper SPE 15441 presented at the SPE 61st Annual Technical Conference and Exhibition, New Orleans, Oct. 5-8, 1986.

21. Khatib, Z.I., Hirasaki, G.J., and Falls, A.H.: "Effects of Capillary Pressure on Coalescence and Phase Mobilities in Foams Flowing Through Porous Media". Paper SPE 15442 presented at the SPE 61st Annual Technical Conference and Exhibition, New Orleans, Oct. 5-8, 1986.

22. Nikolov, A.D., Wasan, D.T., Huang, D.W., and Edwards, D.A.: "The Effect of Oil on Foam Stability, Mechanisms and Implications for Oil Displacement by Foam in Porous Media". Paper SPE 15443 presented at the SPE 61st Annual Technical Conference and Exhibition, New Orleans, Oct 5-8, 1986.

23. Hirasaki, J.G.: "The Steam Foam Process". Journal of Petroleum Technology, May, 1989.

24. Castanier, L.M.: "Steam with Additives: Field Projects of the Eighties". Journal of Petroleum Science and Engineering, 2, 1989.

25. Marfoe, C.H., Kazemi, H., and Ramirez, W.F.: "Numerical Simulation of Foam Flow in Porous Media". Paper SPE 16709 presented at the 62nd Annual Technical Conference and Exhibition of the Society of Petroleum Engineers held in Dallas, TX, September 27-30, 1987.

26. Morgan, C.L. "Basic Principles of Computed Tomography". Baltimore Md: University Park Press, 1983.

## 3.2 CHARACTERIZATION OF SURFACTANTS AS STEAMFLOOD ADDITIVES
(F. Hamida)

Steamflood efficiency can be increased by adding surface active agents to steam to generate foam to preferentially reduce permeability to steam in previously swept zones. The partial results of a continuing project to optimize the results of surfactant use as additives in steamflood applications are reported. Two parts of the project have been completed to date. The foamability of seventeen surfactants was evaluated at steam injection conditions (160°C and 75 psig) and linked to their chemical structure. As previously reported by D. C. Shallcross et al.[1], a linear model saturated with water was used to compare and characterize different surfactants as steamflood additives. During the experiments, surfactant solutions were injected as slugs into the sand pack after steam breakthrough. Nitrogen was injected as a noncondensable gas. Evaluation of foamability was based on pressure gradient changes and steam mobility reduction along the model. Under the conditions of the experiments, alpha olefin sulfonates generated the strongest foam at low surfactant concentrations. Internal olefin sulfonates, linear toluene sulfonates and linear xylene sulfonates all generated stable foams at higher concentrations. Flow resistance due to foam also increased as the alkyl chain length increased.

In the second study, the previous experiments were repeated using eight selected surfactants to check reproducibility. During the runs, two 10% PV slugs of surfactant solution with 0.5 weight percent surfactant concentration were injected into the sand pack. The second slug was injected after the foam created by the first one completely collapsed. Then the runs were repeated under the same operating conditions as the water runs except for the presence of oil. West Newport crude oil was used at residual saturation after steam flooding during these runs. Analysis of the results showed that both the pressure gradients and the reduction in steam mobility after surfactant solution injection were affected by the presence of oil. In the presence of oil, no increase in pressure was observed.

The two sets of experiments were compared using maximum pressure drops and duration of pressure changes, pressure increases with distance from the inlet and time, steam mobility reduction, and thermal parameters. One interesting result was the fact that relative permeability to steam was reduced to between 0.005 and 0.02 when no oil was present.

### 3.2.1 INTRODUCTION

Steam injection is the most common method used in thermal oil recovery. However, volumetric sweep efficiency and oil recovery are significantly limited by gravity override and steam channelling through the more permeable parts of the reservoir. Channelling is the result of the high mobility contrast between steam and the heavy oil. Gravity override results from the density difference between steam and oil. The combined effect is an early breakthrough at the production wells and low sweep efficiency. Improving mobility control is important for a successful steamflooding operation. Foam generated by injection of surfactants can reduce steam channelling by blocking the high permeability regions of the reservoir. Thus, steam is diverted to the less permeable, oil-rich zones resulting in an increase in the volumetric sweep efficiency.

Many workers have conducted laboratory and field tests in an effort to identify the most suitable surfactants in a steam-foam process. The first stage for the selection of a suitable surfactant is to test the thermal stability of the surfactant under steam conditions (Castanier and Brigham[2], McPhee, et al.[3]). The foam-forming ability and the longevity of foam are then examined. Using such a screening technique, McPhee et al.[3] reduced a field of 109 surfactants to eight, which were then tested using a laboratory sand pack in which the foam forming ability of the surfactants under reservoir conditions was observed.

In a patent issued in the United States, Dilgren, et al.[4], found that Siponate DS-10, an alkylaryl sulfonate, was the most suitable surfactant of ones tested. They suggested that the surfactants used should contain between 14 and 22 carbon atoms in the alkyl chain. They further suggested that of the surfactant molecules, about half should contain between 16 and 18 carbon atoms. In a later patent, Muijs and Keijzer[5] concluded that the alpha olefin sulfonates containing up to 30 carbon atoms in alkyl chain would also be suitable as foam-forming surfactants.

Muijs et al.[6] investigated steam-foam properties of alpha olefin sulfonates and alkylaryl sulfonates. They reported that alkyl chain length appears to be an important parameter in the steam-foam performance of surfactants at elevated temperatures. At temperatures around 215°C, they found that alpha olefin sulfonates are the most suitable class of surfactant. At higher temperatures, alkylaryl sulfonates were found to be better. However, all experiments were carried out in absence of oil. Duerksen et al.[7] concluded after a series of experiments that dimers of the alpha olefin sulfonates might be suitable foam-forming surfactants. They recommended that dimers should be prepared from C15 - C20. Law and Borchardt[8] reported results from a Kern River Pilot where an alpha olefin sulfonate containing 16 to 18 carbon atoms in the hydrocarbon chain (AOS1618) improved sweep efficiency and oil recovery of the steam drive but propagated relatively slowly and yielded the same residual oil as that to steam.

Despite the extensive amount of research previously mentioned, no comprehensive study has investigated the characteristics of surfactants as steam foam additives for California type conditions (moderate pressures and temperatures). The objective of this study is to relate the chemical composition of surface active agents to their performance as foamers in steam injection under California steam injection conditions.

The first stage of this study dealt with the steam foam performance of seventeen surfactants. All surfactants tested were sulfonates. Emphasis was placed on pressure drop history, minimum foaming concentration, and duration of pressure response. All experiments were performed in the absence of oil. Among the seventeen surfactants investigated, seven were selected to study the effect of oil on their foamability. A new product, AOS2024DE, was also added. It is an alpha olefin sulfonate containing 20 to 24 carbon atoms in the hydrocarbon chain and enriched in disulfonate content.

Runs with the eight surfactants selected were performed under the same operating conditions both in the absence and presence of residual oil. The total pressure drop induced by the injection of the surfactant and the reduction in steam relative permeability were investigated. Slug injection technique was used in order to be able to examine the persistence of the foam and foam decay.

## 3.2.2 EXPERIMENTAL APPARATUS AND PROCEDURE

The equipment used in this study was built by Wang[9] and is described in detail by Shallcross et al.[1] A horizontal, cylindrical stainless steel tube [ss#321], 1.83 m (6 ft) long with

an outside diameter of 0.057 m (2.25 in) and an inside diameter of 0.0548 m (2.16 in) was used . To reduce heat losses, tube was wrapped with 7 cm of insulating material (a Fiberfrax product). Two flanges were used at each end of the tube. The tube was packed with clean sand and pressure tested to 2.1 MPa (300 psig). Figure 3.2.1 shows a diagram of the model. Temperatures along the sandpack were monitored using 21 type J thermocouples located alternately at the center and at 1.27 cm (0.5 in) from the top of sandpack. Five pressure taps were located at 0.41, 0.82, 1.32, and 1.83 m (16, 32, 52, and 72 in ) from the inlet of the tube. This allowed the foam behavior to be investigated at different sections of the sandpack as will be discussed later.

Five thin film heat flux sensors were mounted on the tube (beneath insulation) in order to measure the rate of heat transfer between the tube and the surroundings. One of the heat flux sensors was located on the top of the tube at 0.965 m (38 in) from the inlet. The other four were located at the top, base, and one side of the tube at 0.651 m (25.5 in ) from the inlet. The use of these sensors has been discussed in detail by Shallcross et al.[1,10]

The fluid injection system consisted of two Constametric Model III pumps. One is used exclusively to supply distilled water to the steam generator. The other was used to inject the surfactant solution and cleaning fluids. Steam was generated by a tubular furnace (Marshall Model #1056) containing a coiled tube, a separate gas line is used to inject nitrogen and carbon dioxide when needed. A sight glass, a backpressure regulator, a condenser, and a fraction collector were connected to the production end of the tube.

An IBM XT computer interfaced with an HP 3497A data-acquisition system stores the temperature and pressure data. Strip chart recorders also monitor the pressure at the end of each of the tube sections, the backpressure, and the nitrogen injection rate.

During the first stage of this work, i.e., screening of the seventeen surfactants, the sandpack used had a porosity of 30.8% and an absolute permeability of ninety Darcys. All experiments were performed using the same sandpack. No oil was present. Initially, the sandpack was saturated with distilled water. Slightly superheated steam was injected into the sandpack at 4.0 ml/min cold water equivalent. A backpressure of 580 kPa ( 70 psig ) was maintained throughout the experiment. Nitrogen injection was started about 30 min after steam breakthrough. Nitrogen was injected at 0.081 L/min ( ~ 0.05 mole % of the gas phase). After injecting nitrogen for about an hour, the first surfactant slug was injected. Each slug was ten percent of the total pore volume and contained one percent by weight sodium chloride. The first slug usually contained 0.1% by weight of the surfactant to be tested. If one hour after the injection of a surfactant slug no increase in the pressure gradient was observed, the slug concentration was progressively increased to 0.25, 0.5, and finally 1.0% by weight until a response was observed. When response was observed, the slug producing that response was followed by one or more slugs of the same concentration.

In the second stage of the work, eight surfactants were selected to investigate the effect of oil. The sandpack was changed. It had a porosity of 34.4% and an absolute permeability of 4.68 Darcys. Since a different sandpack was used, runs where no oil was present were repeated. The same operating conditions were used for all surfactants, both in the presence and absence of oil. All surfactants slugs had a concentration of 0.5% by weight and were 10% of the total pore volume. Nitrogen was injected at 0.063 L/min (2 - 4 mole% of the gas phase). Other operating conditions were the same as those used in the first stage of the work. During the oil runs, Mobil's Newport Field oil was used. Oil was was present in the sandpack at a residual saturation after steam of about 5%.

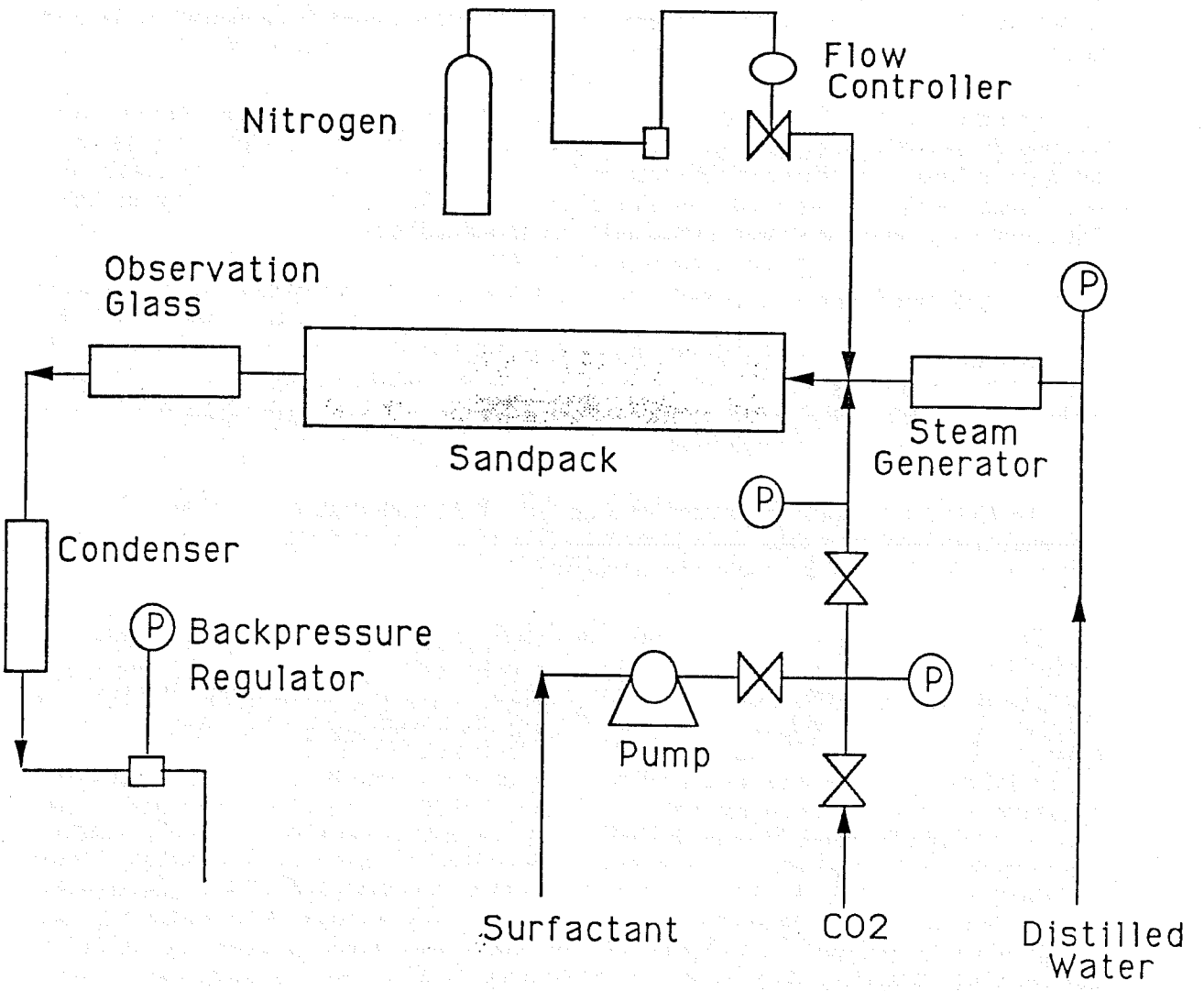


Figure 3.2.1 A simplified representation of the experimental apparatus.

The sandpack was thoroughly cleaned after each experiment. When no oil was present, cleaning was achieved by injecting about 10 pore volumes of distilled water. This was then followed by 0.8 to 1 pore volume of isopropanol to remove all traces of the surfactant. This in turn was followed by the injection of 15 pore volumes of distilled water. Carbon dioxide was used to remove all nitrogen from the tube. Finally, about 15 pore volumes of distilled water were injected. When oil was present in the sandpack, cleaning was started by injecting 3 to 4 pore volumes of mineral spirit to dissolve the oil. This was then followed by about 1 pore volume of TBA (Tert-Butyl Alcohol). About 5 pore volumes of hot distilled water were then injected to remove TBA. Carbon dioxide was used to remove all gasses. Finally about 20 pore volumes of distilled water were injected to remove carbon dioxide.

### 3.2.3 RESULTS AND DISCUSSION

In the first stage, seventeen surfactants were tested. Chemical structures included alpha olefin sulfonates (AOS), internal olefin sulfonates (IOS), linear alkyl xylene sulfonates (LXS), linear toluene sulfonates (LTS) and others. Within a class of surfactants having the same chemical structure, the length of the alkyl chain was varied. The results are shown in Table 3.2.1. The minimum concentration causing a significant increase in the pressure drop is listed for each product. The magnitude and duration of the pressure drop increase are also reported. Only four generated significant pressure gradient within the sandpack upon injection of 0.1% by weight solution (Enordet AOS1618, AOS2024, and LTS18 and Chevron SD1000).

The highest pressure drop generated by the 0.1% solution was for the alpha olefin sulfonate with the longest alkyl chain (AOS2024). Figure 3.2.2 shows the pressure drop vs time for AOS1618 and AOS2024. AOS2024 has the longer chain length. In all figures, zero time corresponds to the start of the injection of the first surfactant slug. These results agree with Muijs et al.[6] Three products (Enordet IOS1720 and IOS2024 and Hoecht OSfl) generated significant pressure drops at 0.25%. Figure 3.2.3 shows the response of the internal olefin sulfonates. The lightest (IOS1517) did not foam at 0.25%. The response of the IOS2024 lagged the response of IOS1720 by about 0.3 hours suggesting adsorption desorption by the sand in a process that we do not understand. The linear alkyl xylene sulfonates only foamed at 1% by weight concentration.

Among the seventeen surfactants tested in the first stage, seven were selected for further investigation. The initial objective was to study the effect of oil on the foamability of these surfactants. Since a different sandpack was used, runs in the absence of oil were also repeated under the same operating conditions as described earlier. The seven surfactants included alpha olefin sulfonates (AOS2024, AOS1618, and SD1000), internal olefin sulfonates (IOS1518, IOS1720, and IOS2024), and a linear toluene sulfonate (LTS18). AOS2024DE, a newly introduced product from Enordet, was also tested. It is an alpha olefin sulfonate enriched in disulfonate content compared to AOS2024. All the runs in the second stage were performed at 0.5% by weight concentration.

Table 3.2.2 lists the maximum observed total pressure drop across the sandpack for each surfactant. These pressures correspond to runs made with no oil present in the sandpack. The other parameter listed in Table 3.2.2 is a measure of foam strength and persistence. These values are the integral of the area under the pressure drop versus time curve. As before, AOS2024 formed the strongest foam. It yielded the highest total pressure drop. Also, as shown in Table 3.2.2, AOS2024 yielded the highest area under total pressure drop versus time curve. The difference in values reported on Table 3.2.2 and those reported in Table 3.2.1 is attributed to the difference in concentration (0.5% versus 0.1% by weight), and to the use of a different sandpack. AOS1618, an alpha olefin sulfonate tested by Shell with success in the

Table 3.2.1 Pressure Responses for Seventeen Surfactants

| Surfactant | Manufacturer | Minimum Foaming Concentration (wt%) | Maximum Pressure Drop (kPa) | Duration of Pressure Response (min) |
|---|---|---|---|---|
| AOS2024 | Shell | 0.10 | 1611 | 85 |
| AOS1618 | Shell | 0.10 | 928 | 68 |
| LTS18 | Shell | 0.10 | 396 | 91 |
| SD1000 | Chevron | 0.10 | 45 | 19 |
| IOS1720 | Shell | 0.25 | 1497 | 79 |
| IOS2024 | Shell | 0.25 | 1438 | 87 |
| OS fl | Hoechst | 0.25 | 449 | 45 |
| SAS 60 | Hoechst | 0.50 | 1479 | 80 |
| IOS1517 | Shell | 0.50 | 1105 | 101 |
| AOS1416 | Shell | 0.50 | 487 | 144 |
| LTS1618D | Shell | 0.50 | 290 | 133 |
| LXS16 | Shell | 1.00 | 1583 | 89 |
| LXS18 | Shell | 1.00 | 1464 | 89 |
| LXS1314 | Shell | 1.00 | 1392 | 113 |
| LXS814 | Shell | Foaming did not occur for 1.00 wt %. | | |
| LSX1112 | Shell | Foaming did not occur for 1.00 wt % | | |
| SD1020 | Chevron | Foaming did not occur for 1.00 wt % | | |

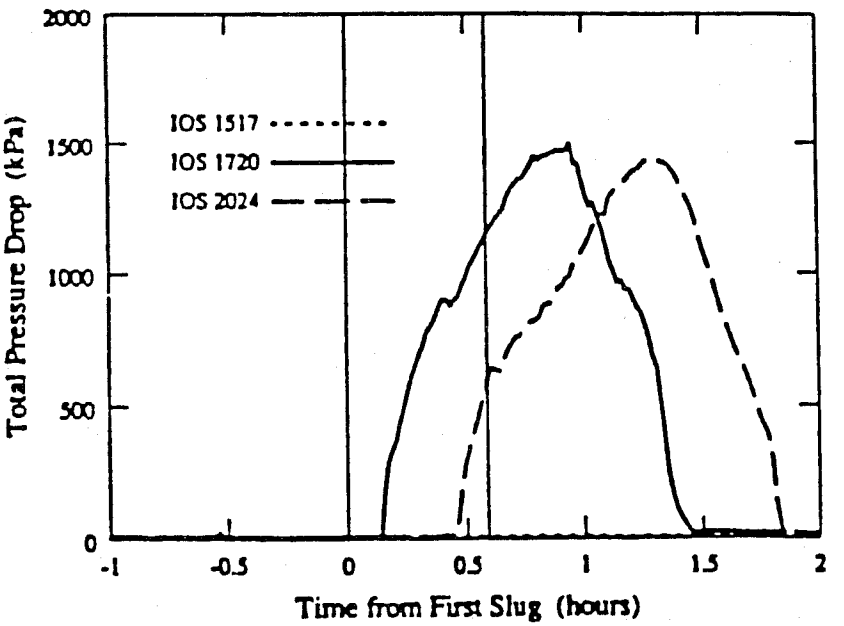


Figure 3.2.2 Total pressure drop responses to injection of single 0.10% slugs of Alpha Olofin Sulfonates AOS1618 and AOS2024.

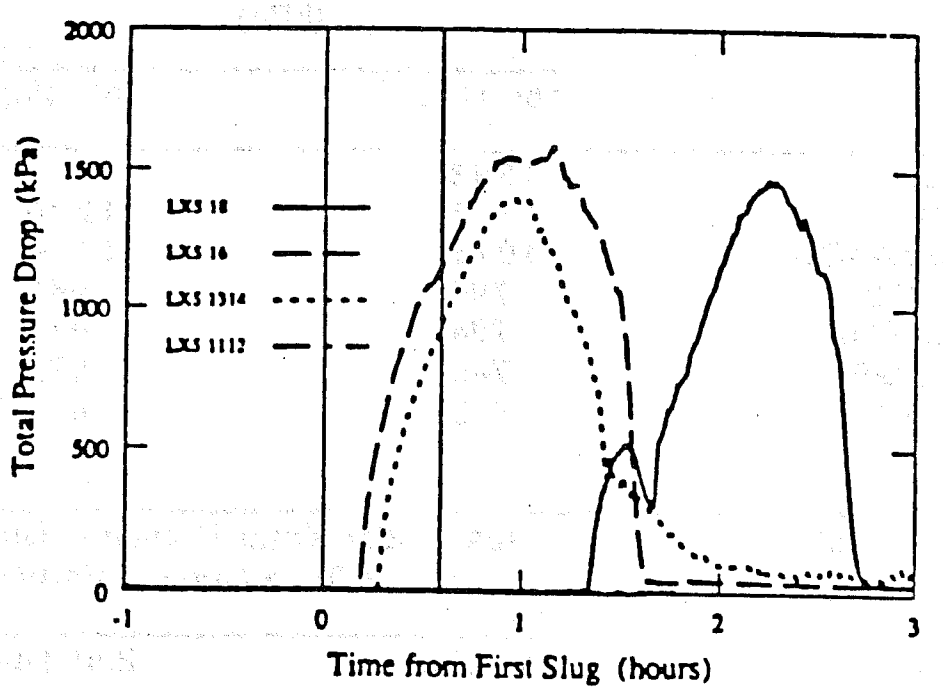


Figure 3.2.3 Total pressure drop responses to injection of single 0.25% slugs of internal olefin sulfonates.

Table 3.2.2 Pressure Responses and Foam Persistence of Various Surfactants

| Surfactants | Maximum Pressure Drop (kPa) | |
|---|---|---|
| | 1st slug | 2nd slug |
| AOS2024 | 1333 | |
| LTS18 | 1113 | 1226 |
| AOS2024DE | 1076 | 1166 |
| SD1000 | 796 | 945 |
| AOS1618 | 794 | 879 |
| IOS1720 | 745 | 878 |
| IOS1518 | 432 | 460 |

| Surfactants | Area Under Total Pressure Drop Versus Time Curve (kPa-hr) | |
|---|---|---|
| | 1st slug | 2nd slug |
| AOS2024 | 4696 | |
| AOS2024DE | 1777 | 1847 |
| LTS18 | 1492 | 4151 |
| SD1000 | 876 | 1239 |
| AOS1618 | 908 | 1074 |
| IOS1720 | 545 | 844 |
| IOS1518 | 203 | 371 |

Kern River Field, dropped to fifth in ranking in terms of total pressure drop. This may be due to the increase in concentration from 0.1% to 0.5% by weight. An increase in concentration had a different effect on LTS18 and SD1000. The total pressure drop caused by LTS18 increased from 396 kPa to 1226 kPa, while that caused by SD1000 increased from 45 kPa to 984 kPa. However, the use of a different sandpack may have affected the results.

Figures 3.2.4 and 3.2.5 show total pressure drop versus time for alpha olefin sulfonates and internal olefin sulfonates. Under the operating conditions, an increase in alkyl chain length resulted in an increase in foam strength. This conclusion held for both alpha olefin sulfonates and internal olefin sulfonates. IOS2024 did not cause an increase in pressure gradient. This was attributed to having an old sample. From Figure 3.2.4, AOS2024DE gave a lower pressure drop than AOS2024. Thus, we may conclude that the enrichment in disulfonate content resulted in a slightly weaker foam. Also, the foam generated by AOS2024 is more persistent than that formed by AOS2024DE. For the first slug, the duration of pressure response was 4.3 hours for AOS2024 compared to 2.2 hours for AOS2024DE. Also from Table 3.2.2, the area under the total pressure drop versus time curve was 4,696 kPa-hr for AOS2024 and only 1,777 kPa-hr for AOS2024DE. In the case of AOS2024DE, the pressure increased faster and also dropped faster than the normal AOS2024 once it reached a peak. That is because AOS2024DE propagated faster than AOS2024 due to being richer in disulfonates. Since AOS2024DE propagates faster, the foam generated reaches the downstream sections of the sandpack faster blocking the flow and reducing steam mobility which translated into an increase in pressure gradient. AOS2024 formed a stronger foam than AOS1618 but propagated slower. This is because a higher carbon number rendered the surfactant less tolerant to divalent ions resulting in slower propagation (Law and Borchardt[8]). Enordet solved this problem by enriching the disulfonate content through the development of AOS2024DE. These results are consistent with Hirasaki's[11] comments.

For all surfactants, the pressure response due to the second slug was higher than that due to the first slug. Clearly surfactant injection during each slug built onto the surfactant present from the preceding slugs to increase the foaming response. Fig. 3.2.6 demonstrates this effect for SD1000 and LTS18. In addition to pressure drop, steam permeability reduction caused by the injection of the foaming agents was calculated.

Since the sandpack was flooded by steam until reaching steady state condition before the surfactant solution was injected, the rate of heat loss from the inlet to position x along the sandpack can be obtained from the steady state convective heat transfer equation:

$$H_{1x} = 2prU \int_o^x (T_x(x') - T_o)\, dx' \tag{3.2.1}$$

The heat flux sensors mounted on the tube were used to find U, the overall heat transfer coefficient. Equation 3.2.2 is a heat balance. The rate of heat flow equals the heat injection rate minus the rate of heat loss:

$$A\dot{m}_i h_v f_{st}(x) = A\dot{m}_i h_v - 2prU \int_o^x (T_s(x') - T_o)\, dx' \tag{3.2.2}$$

From equation 3.2.2, an expression for the flowing steam quality can be obtained from:

$$f_{st}(x) = 1 - \frac{2prU \int_o^x (T_s(x') - T_o)\, dx'}{Ah_v \dot{m}_i} \tag{3.2.3}$$

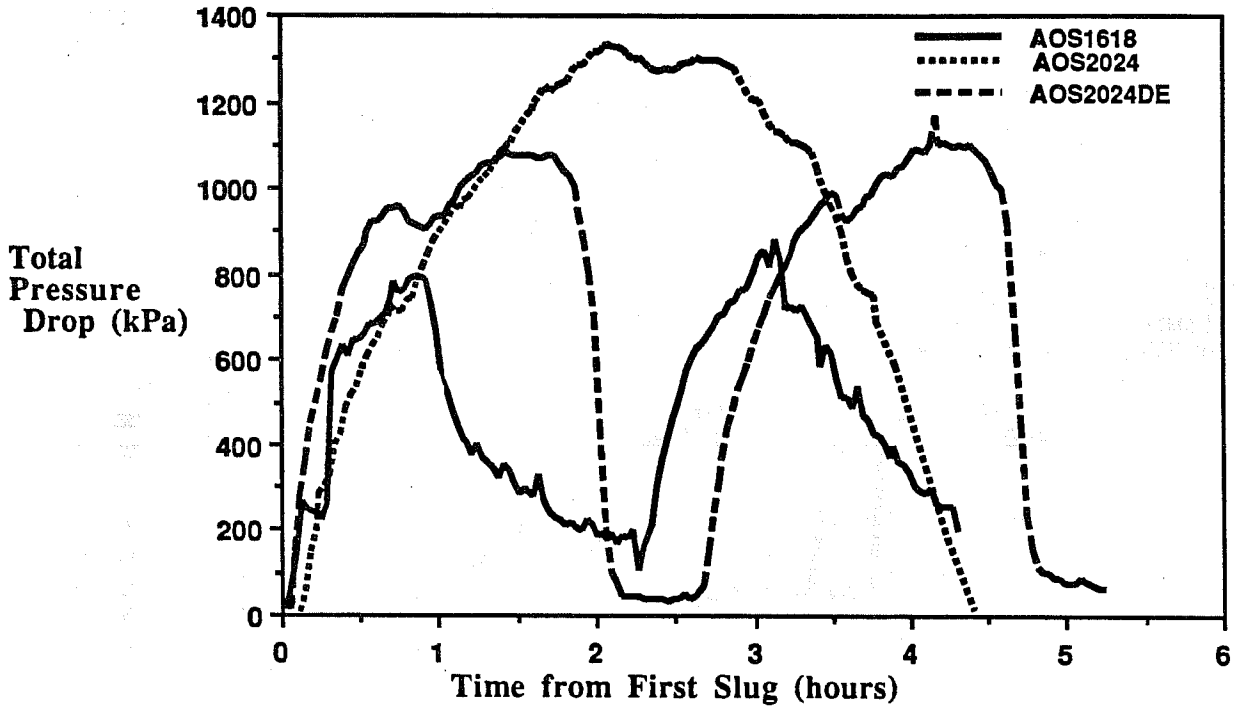


Figure 3.2.4 Total pressure drop responses to injection of 0.5% slugs of alpha olefin sulfonates.

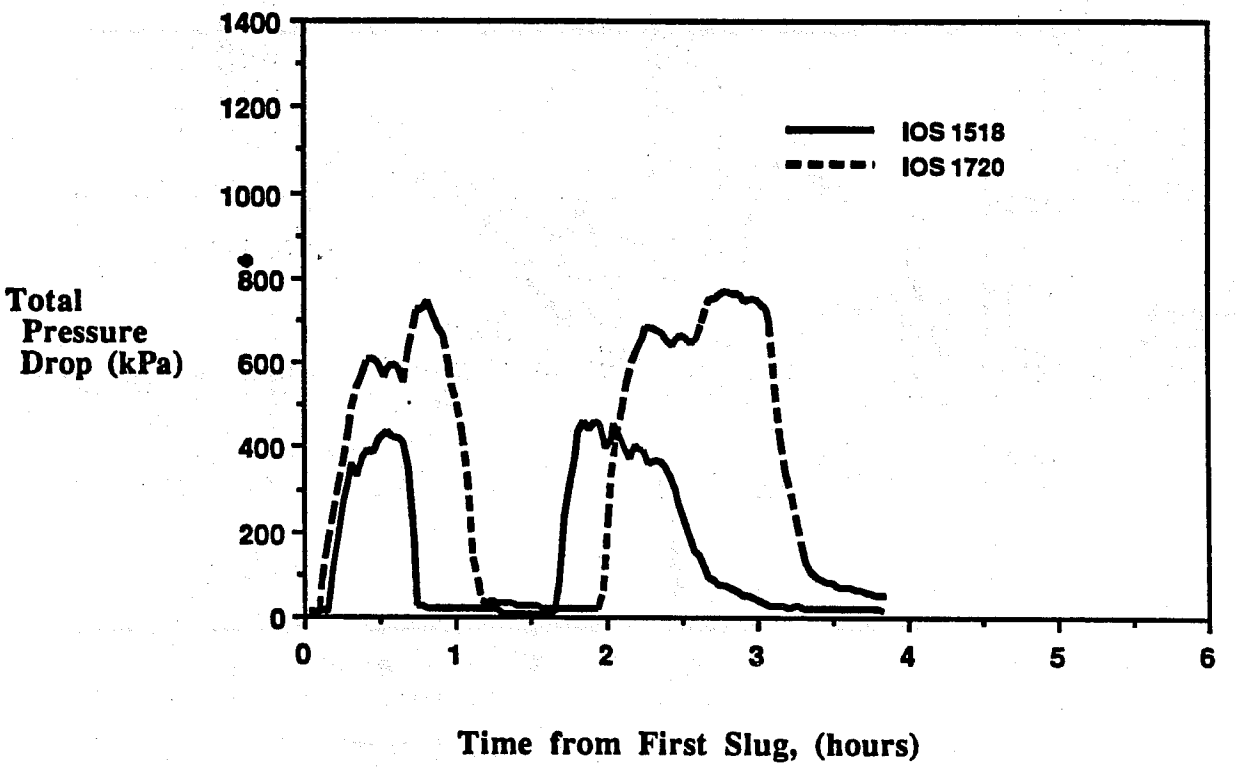


Figure 3.2.5 Total pressure drop responses to injection of 0.5% slugs of internal olefin sulfonates.

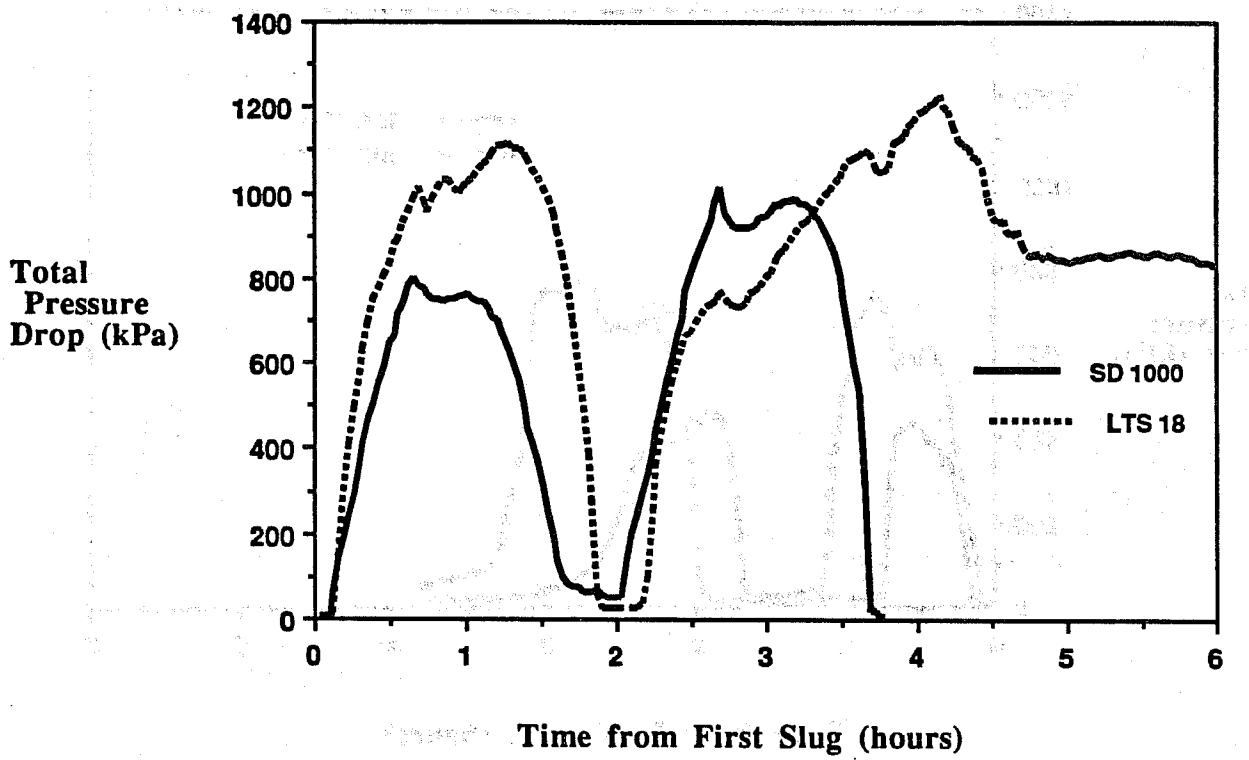


Figure 3.2.6 Total pressure drop responses to injection of 0.5% slugs of SD1000 and LTS18.

In equation 3.2.4, two expressions for the steam volumetric flow rate are equated:

$$q = \frac{A\dot{m}_i f_{st}(x)}{r_s} = -k_a A \left[\frac{k_r}{m}\right]_s \frac{dp}{dx} \tag{3.2.4}$$

When pressures are less than 2.75 MPa (400 psia) (Wang and Brigham[9]):

$$\frac{r_s}{m_s} = bP_s^g \tag{3.2.5}$$

where $b$ = .004466 and $g$ = .8704.

Combining equations 3.2.3, to 3.2.5 and integrating from location 1 to location 2 along the sandpack:

$$k_{rs} = \frac{(1+g)\dot{m}_i \int_{x_1}^{x_2} f_{st}\,dx}{k_a b (P_1^{1+g} - P_2^{1+g})} \tag{3.2.6}$$

Equation 3.2.6 gives an expression for the steam relative permeability over a section of the sandpack. In order for these equations to be valid, calculations of the steam relative permeability must be performed when only steam and nitrogen were injected. The data discused later include the time periods when no surfactant was being injected. The first data point corresponds to the time immediately after surfactant injection ceased.

Figure 3.2.7 shows steam relative permeability over the whole sandpack for the five strongest foamers. Figures 3.2.8 to 3.2.10 show the behavior of steam relative permeability in each of the four sections of the sandpack for AOS2024, LTS18, and AOS2024DE, respectively. For all surfactants, a significant steam permeability reduction was achieved. Steam relative permeability ranged from 0.005 to 0.02 as soon as foam was present. A similar trend was obtained for all surfactants. Steam relative permeability started at a high value, decreased to a minimum, then increased. The stronger the foam, the longer the steam relative permeability stayed at a minimum value. In the case of AOS2024 which caused the strongest foam, the steam relative permeability stayed at a minimum value of 0.0017 for 1.5 hours. Also, referring to Figure 3.2.7, AOS2024DE gave lower steam relative permeability values than AOS2024. As mentioned earlier, AOS2024DE propagated rapidly causing pressure to increase rapidly which results in low steam relative permeabilities at early time. The minimum steam relative permeability values were almost the same for all surfactants. This suggests that if continuous injection is to be used and steam relative permeability reduction is the main objective, all of the eight surfactants tested may be appropriate.

Under the operating conditions mentioned earlier, none of the surfactants caused a pressure increase. The authors do not understand the reasons behind this. One the possible reasons is that oil might have been contaminated with deemulsifiers used in the field. Another possible reason is that under experimental conditions, none of the surfactants tested is able to generate foam due to the detrimental effect of oil on foam flow. Oil can destabilize foam by dissolving the surfactants from the gas/water interface. Also Law and O'Brien12 reported that spreading oil can delay foam generation. Foam may have been generated but the presence of

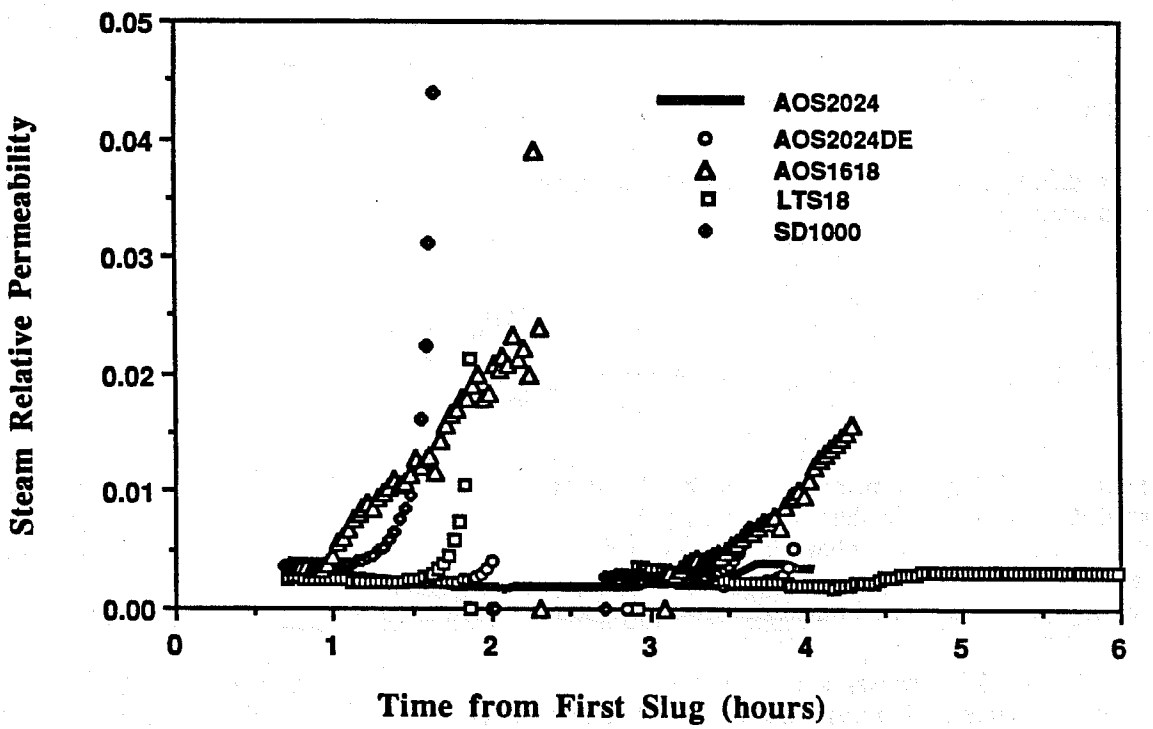


Figure 3.2.7 Steam relative permeability along the sandpack when 0.5% slugs of surfactants are injected.

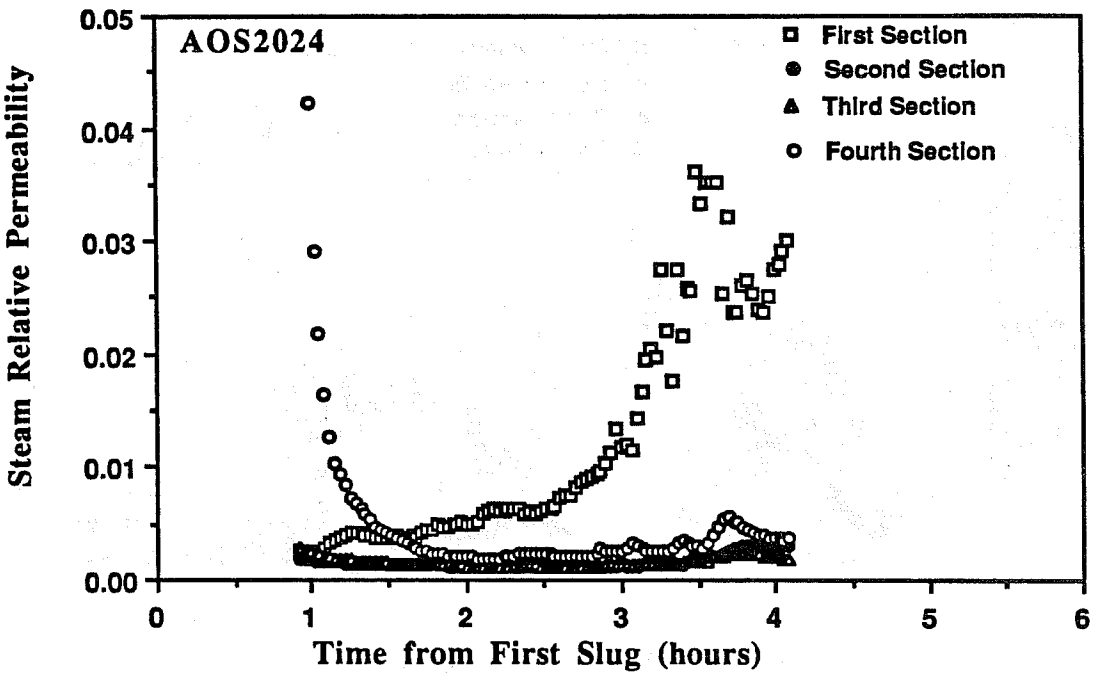


Figure 3.2.8 Steam relative permeability in four different sections of sandpack when 0.5% slug of AOS2024 is injected.

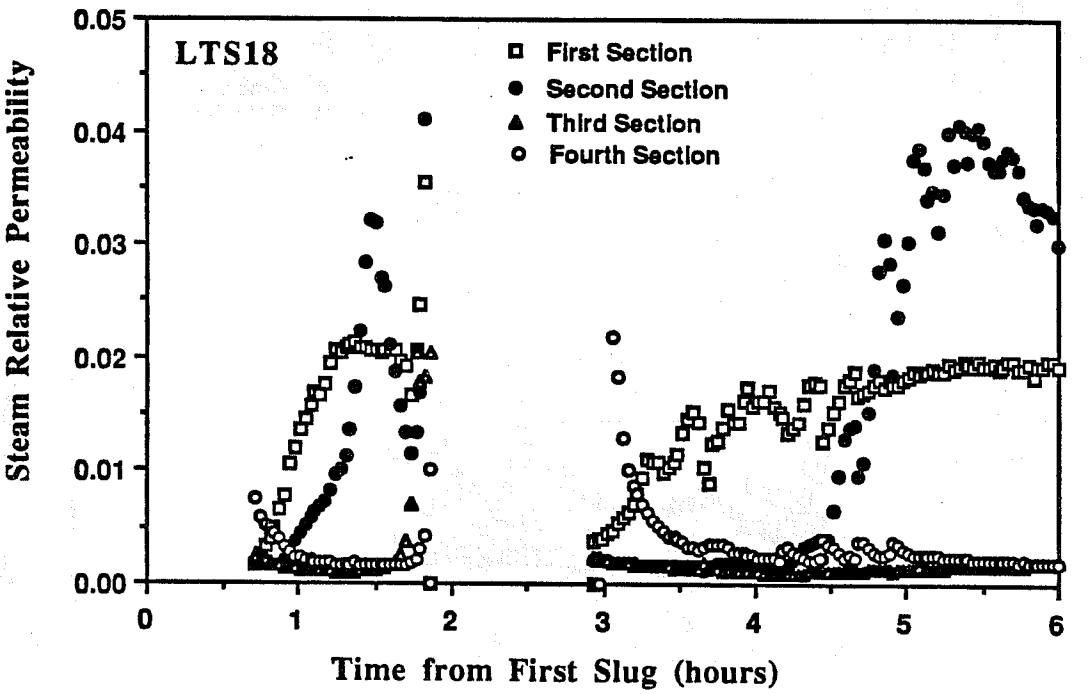


Figure 3.2.9 Steam relative permeability in four different sections of sandpack when 0.5% slugs of LTS18 are injected.

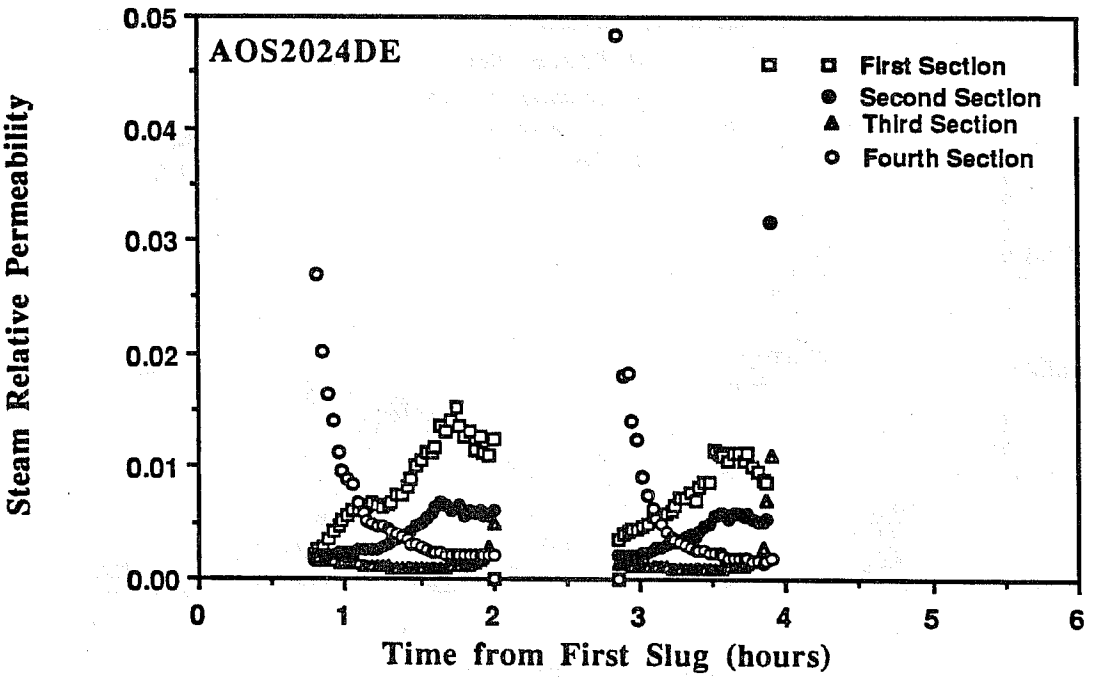


Figure 3.2.10 Steam relative permeability in four different sections of sandpack when 0.5% slugs of AOS2024DE are injected.

oil may have caused immediate collapse.

Robin[13] and Demiral and Okandan[14] reported foaming in the presence of oil under slightly different conditions from this study. The next stage of our work will be trying other oils. The operating conditions will be changed to try to determine the range under which large pressure gradients can be generated in the presence of oil.

## 3.2.4 CONCLUSIONS

1. Under the experimental conditions alpha olefin sulfonates generated the strongest and most long-lived foams of all the surfactants tested at low concentrations.

2. Internal olefin sulfonates and linear alkyl-xylene sulfonates produced just as strong foams, but required higher surfactant concentrations. Not enough linear toluene sulfonates were studied to allow similar conclusions to be drawn.

3. Generally, under the experimental conditions, within each surfactant class the strength of the foam increased with increasing alkyl chain length.

4. Significant steam relative permeability reduction was achieved for all eight surfactants tested. Steam relative permeability values ranged from 0.005 to 0.02 in the presence of foam.

5. Under the experimental conditions, none of the surfactants caused a pressure increase in the presence of residual crude oil.

## 3.2.5 ACKNOWLEDGEMENT

This work was performed at the Stanford University Petroleum Research Institute (SUPRI-A) under U.S. DOE Contract DE-FG19-87BC14126. The authors acknowledge the support of SUPRI Industrial Associates. D. C. Shallcross also gratefully acknowledges the support of the Commonwealth Scientific and Industrial Research Organization, Australia. The authors also thank Enordet, Chevron, and Hoescht for supplying the surfactant samples and Mobil for supplying the crude oil

## 3.2.6 NOMENCLATURE

A = Cross-Sectional Area, m2
fst = Flowing Steam Quality
Hlx = Rate of Heat Loss at Position x, J/s
hv = Latent Heat of Vaporization, J/Kg
Ka = Absolute Permeability, 5m2
Krs = Steam Relative Permeability
mi = Mass Injection Rate of Steam, Kg/s
Ps = Steam Pressure, MPa
P1 = Upstream Pressure, MPa
P2 = Downstream Pressure, MPa
q = Steam Volumetric Flow Rate, m3/s
r = Outside Tube Radius, m

Ts = Steam Temperature, {K
T0 = Ambient Temperature, {K
U = Overall Heat Transfer Coefficient, W/m2 {K
x = Axial Distance Along the Sandpack, m

### 3.2.7 REFERENCES


1. Shallcross, D. C., Castanier, L. M., and Brigham, W. E.: "Characterization of Surfactants as Steamflood Additives," Proceedings, III International Symposium on Enhanced Oil Recovery, Maracaibo, Venezuela, February 1989, 561-581

2. Castanier, L. M. and Brigham, W. E.: "Selecting Foaming Agents for Steam Injection Improvement," Chemical Engineering Progress, Vol. 6, 37-40 (1985).

3. Mcphee, C. A., Tehrani, A. D. H., and Jolly, R. P. S.: "Foam Flooding Of Cores under North Sea Reservoir Conditions," SPE/DOE 17360, Presented at the Sixth SPE/DOE Symposium of Enhanced Oil Recovery, Tulsa, Oklahoma, April 1988.

4. Dilgren, R. E., Hirasaki, G. J., Hill, H. J., and Whitten, D. G.: "Steam- Channel-Expanding Steam Foam Drive," U. S. Patent 4,393,937, issued May 2, 1978.

5. Muijs, H. M. and Keijzer, P. P. M.: "Steam Foam Process," U. S. Patent 4,693,311, issued September 15, 1987.

6. Muijs, H. M., Keijzer, P. P. M., Wiersma, R. J." "Surfactants For Mobility Control in High Temperature Steam-Foam Applications," SPE/DOE 17361, Presented at the Sixth SPE/DOE Symposium of Enhanced Oil Recovery, Tulsa, Oklahoma, April 1988.

7. Duerksen, R. E., Wall, R. G., and Knight, J. D.: "Steam injection Including Alpha-Olefin Sulfonate Dimer Surfactant Additives and a Process of Stimulating Hydrocarbon Recovery from a Subterranean Formation," U.S. Patent 4,556,107, issued December 3, 1985.

8. Law, H. C. and Borchardt, J. K.: "Improved Steam Foam Formulations: Concepts and Laboratory Results," SPE 18783. Presented at the 1989 SPE California Regional Meeting, Bakersfield, CA, April 1989.

9. Wang, F. P. and Brigham, W. E.: "A Study of Heat Transfer During Steam Injection and Effect of Surfactants on Steam Mobility Reduction," DOE Report DE-AC03-81SF-11564, SUPRI Report TR 55, August 1986.

10. Shallcross, D. C. and Wood, D. G.: "The Accurate Measurement of Heat Flux Using a Film Heat Flux Sensor with Application to Axisymmetric Bodies," Proceedings, Eighth International Heat Transfer Conference, 1986, 3.

11. Hirasaki, J. G.: "The Steam Foam Process," JPT (May 1989) 449-456.

12. Law, H. C. and O'Brien, S. M.: "Effects of spreading and Nonspreading Oils on Foam Propagation Through Porous Media," SPE RE (August 1988) 893-896.

13. Robin M.: "Utilisation D'agents Moussants Pour Ameliorer L'efficacite De L'injection De Vapeur," Proceedings, 3rd European Meeting on Improved Oil Recovery, Roma, Italy, April 1985, 349-361.

14. Demiral M. R. B. and Okandan E.: "Experimental Analysis of Steam Foam Injection to Heavy Oil Limestone Reservoirs," SPE 15734. Presented at the Fifth SPE Middle East Oil Show, Manama, Bahrain, March 1987.

## 3.3 MICROVISUALIZATION OF FOAM FLOW IN A POROUS MEDIUM (J.W. Hornbrook)

The study of foam with application to petroleum engineering began with the pioneering work of Bond and Holbrook[1] in 1958. Their work concentrated on the mobility effects of injected foam and it pointed out the benefits of foam injection as a method of enhancing oil reservoir performance. Over the next thirty years much research and several field experiments have attempted to both qualify and quantify the flow mechanisms of foam in porous media. Research carried out in foam flow may be roughly divided into three broad areas: 1) foam properties, 2) foam flow mechanisms, and 3) foam interactions with oil.

Many papers have been written on the properties of foam as a fluid. The results of these papers are rarely in agreement on the nature of foam and often are contradictory. A chronological survey of foam research was carried out by Marsden[2] (1986). In his survey, Marsden outlines the major advances in the understanding of foam flow and points out shortcomings and contradictions in existing work. A brief summary of foam fluid properties is: 1) foam is a fluid of high apparent viscosity, 2) foam viscosity is a function of surfactant concentration, 3) foam viscosity is a function of flow rate, and 4) the flow history of foam affects its apparent viscosity.

Foam flow mechanisms, the means by which foam propagates through a porous medium, have been studied in numerous papers as well. Most of this work, however, has focused on a qualitative description of foam rather than a quantitative one. Most recently, the research of Owete[3] (1984), and Ettinger and Radke[4] (1989) have attempted to extend the understanding of foam flow mechanism beyond the description of observed phenomena. Owete studied the flow of foam in the two areas: 1) propagation of foam and its components, and 2) the mobility of gas in the presence of foam. Owete carried out his work in micromodels with homogeneous and heterogeneous flow paths and, although most of his conclusions were qualitative, some quantitative results were obtained. The research planned will verify Owete's results and extend the quantitative aspects of his work.

Research on the effects of oil on foam is limited and almost entirely qualitative. In addition to the extension of Owete's work, the effects of porous medium wettability on the flow of foam will be studied.

### 3.3.1. EQUIPMENT

Apparatus has been constructed so the flow of foam through a micromodel may be simultaneously observed, videotaped, and photographed, and the pressure drop across the model monitored. The micromodel is a two-dimensional representation of a porous medium made by etching a flow path into a silica wafer and then bonding the wafer to a flat piece of glass (Fig. 3.3.1), thus creating a self contained flow path. At present, two homogeneous pattern micromodels have been constructed. In both models, flow paths are etched to a depth of 30 microns. The pattern in one of the micromodels represents cubic packing of spheres with radii of 100 microns. In the second micromodel, the flow pattern represents rhombohedral packing of spheres with radii of 30 microns. A micromodel that represents a two-dimensional slice of a Berea sandstone is currently being constructed. A detailed description of the construction of the Berea replica micromodel serves to illustrate how all micromodels for the proposed experiments are made.

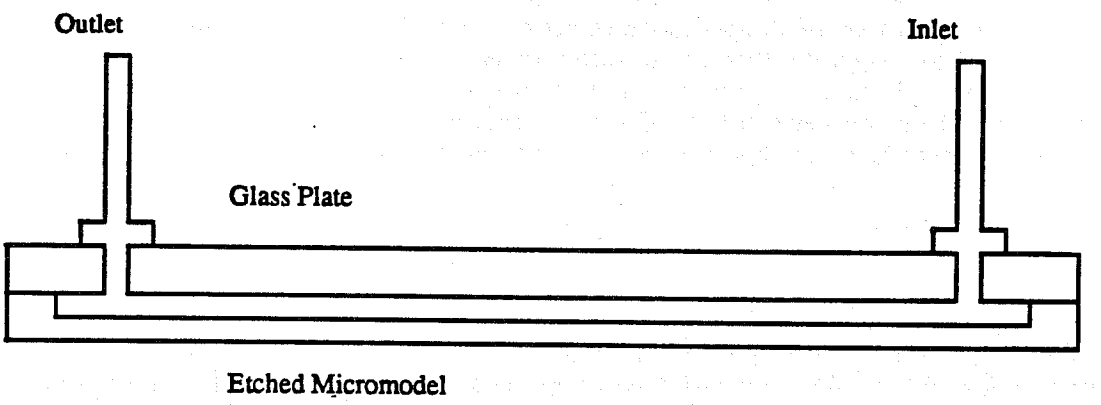


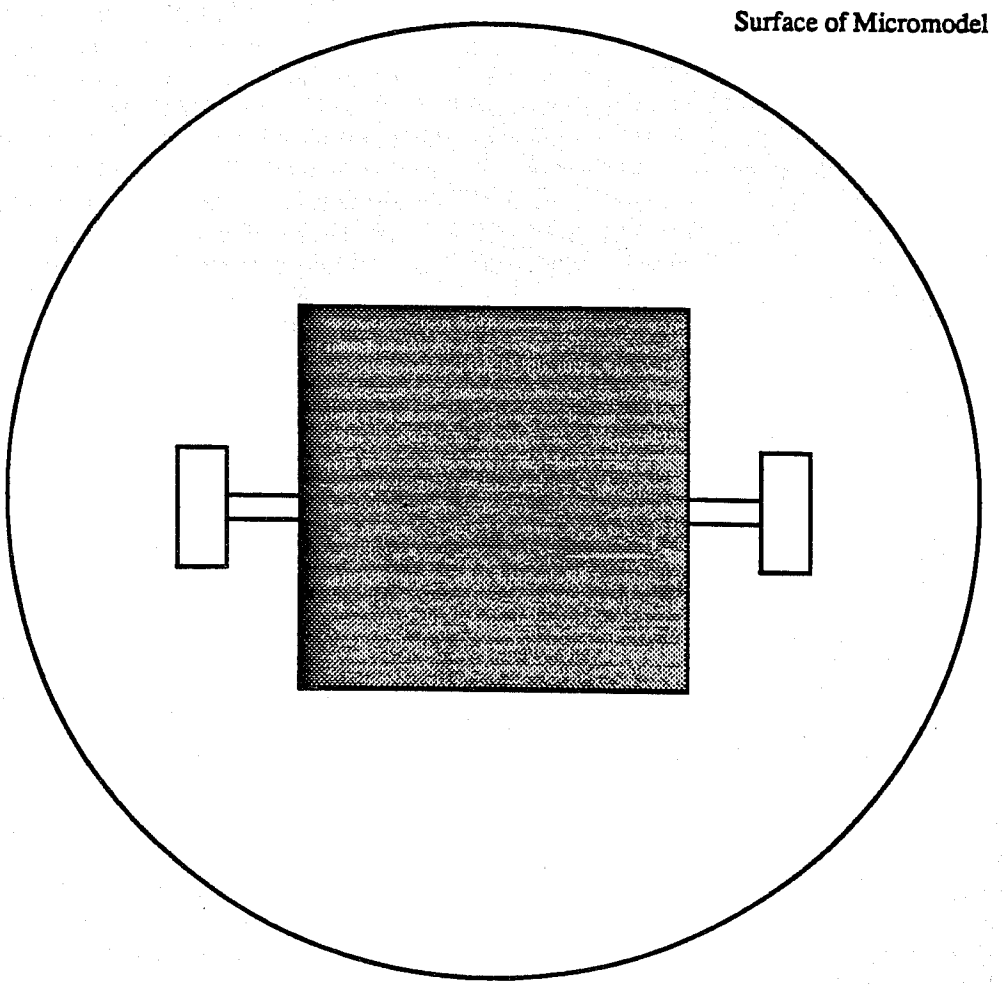


Figure 3.3.1 Micromodel schematic

A thin section of a clean Berea sandstone was prepared with the pore spaces filled with blue-dyed epoxy so a color contrast was obtained between grains and pores. A black and white, color reversed photograph of the thin section was taken at no magnification. This color reversed image is called a mask of the sample. The sample mask is necessary to transfer the image of the sandstone onto a silica wafer for construction of flow channels. The image transfer process is carried out in the following manner:

1. Oxidize one side of a silicon wafer (5 cm. diameter).
2. Coat one side of the oxidized wafer with a photoresist substance.
3. Position the sample mask on the photoresist side of the wafer.
4. Expose the sample mask to ultra-violet light. The structure of the photoresist is destroyed by contact with ultra-violet light. Since the sample mask is a negative of the sample, the photoresist is destroyed where pores exist.
5. Etch the wafer with hydrofluoric acid to the desired depth.

Only the parts of the wafer not coated with photoresist will be etched, so after etching, the pores and flow channels of the Berea sample will be etched away while the grains will be intact. After etching, the wafer is anodically bonded to a flat glass plate. The process of anodic bonding is simple and easy to carry out. The silicon wafer, in contact with the glass plate, is sandwiched between two electrodes (the negative electrode contacting the glass plate) and the entire system is placed on a hot plate (Fig. 3.3.2). The system is heated to 400°C and a potential drop of 600 V is applied across the electrodes. Bonding between the wafer and the glass plate is immediate and is irreversible. Figure 3.3.3 illustrates the initial and final potential distributions across the system.

Figure 3.3.4 shows a schematic of the equipment to be used in all experimental runs. A syringe pump will be used to either independently or simultaneously inject a surfactant solution and air which may be mixed in a foam generation cell and observed through a view port. While foam is passing through the view port, it will be photographed at regular intervals so a record of foam texture may be kept throughout the run. Next, the foam will pass through the micromodel. While in the micromodel, video and still cameras will record the movement of the foam (Fig. 3.3.5). After leaving the micromodel the foam will pass through another view port. Here, more photographs will be taken of the foam to determine, by comparison with the photographs from the inlet port, if structural changes have taken place in the foam. The pressure drop across the micromodel will be monitored with the use of a pressure transducer, and pressure data will be recorded on a chart recorder.

By using a digital analysis program to manipulate the visual data, and with the addition of pressure drop data, an attempt will be made to develop an empirical model describing the flow of foam at the pore level.

## 3.3.2. PLANNED WORK - 1990

The following work is planned for 1990. It will be carried out in the order indicated:

1. Verify Owete's work in a homogeneous flow channel micromodel. Air will be injected into a surfactant saturated micromodel at a flow rate of $2.5 \times 10^{-4}$ cc/s and the recorded pressure drop and general flow characteristics observed will be compared to those recorded by Owete. Note: The flow rate used in Owete's work corresponds to a reservoir flow rate of about 100 feet per day. This flow rate is typical of flow rates near a well bore. Attempts will be made to reduce the flow rate to the range of one to ten feet per day (typical reservoir flow rate).

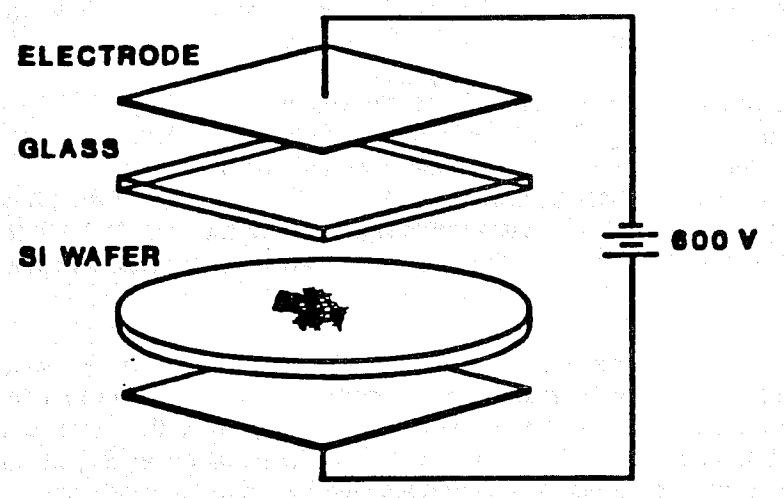


Figure 3.3.2 Schematic of anodic bonding process

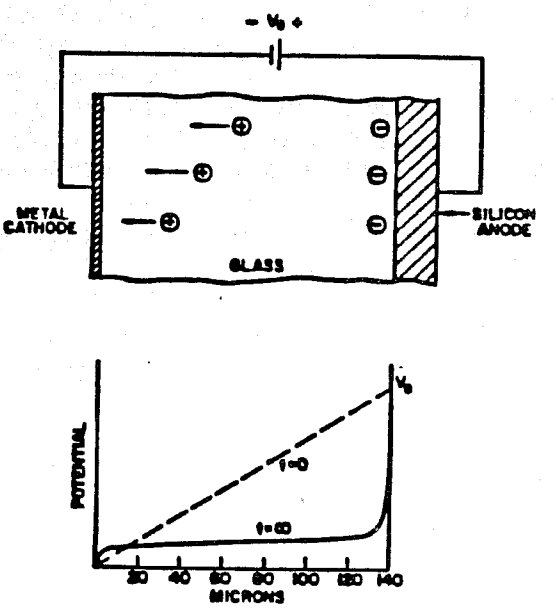


Figure 3.3.3 Initial and final equilibrium DC potential distributions across the glass plate during anodic bonding

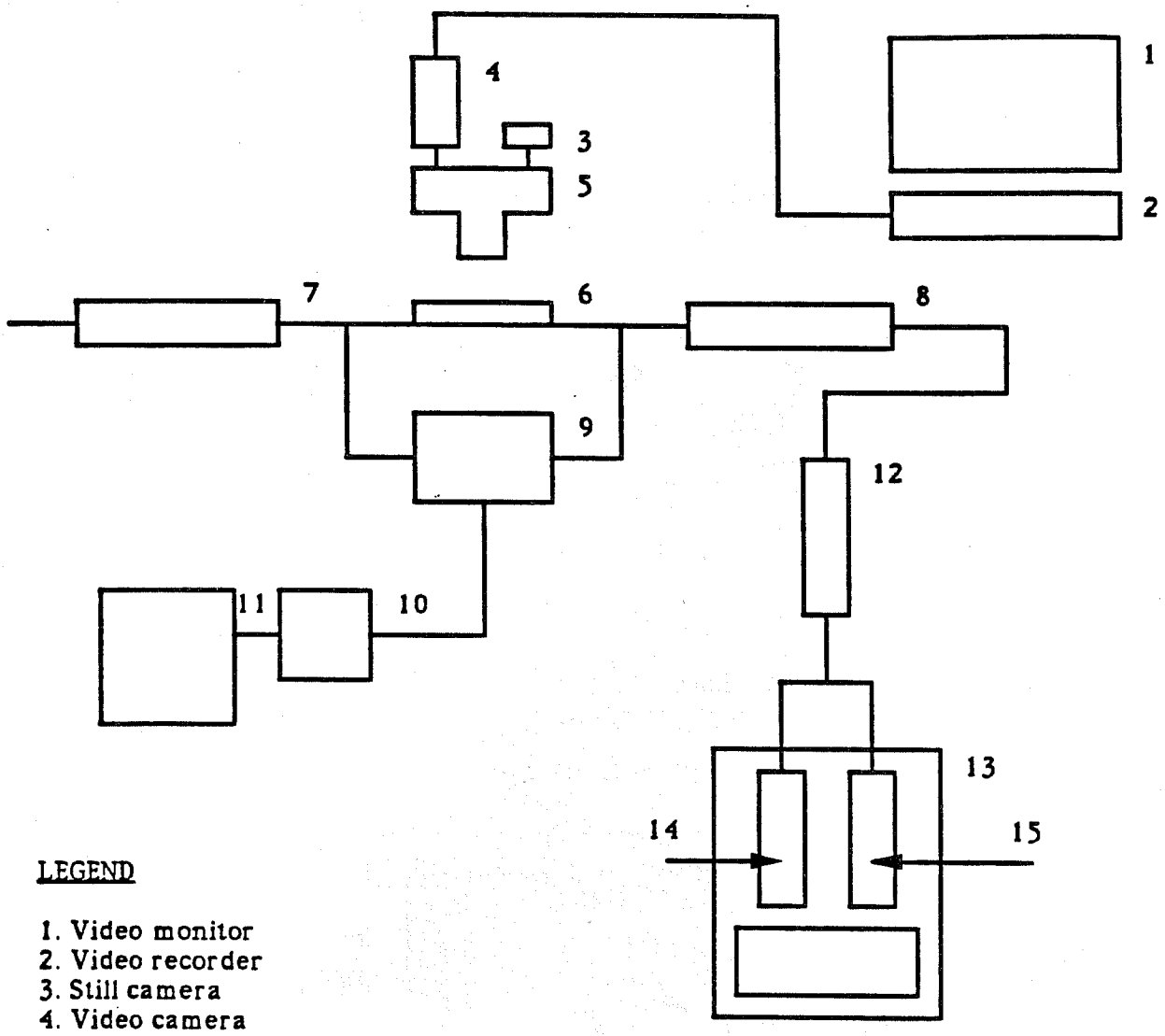


LEGEND

1. Video monitor
2. Video recorder
3. Still camera
4. Video camera
5. Microscope
6. Micromodel
7,8. Foam view port
9. Pressure transducer
10. Voltmeter
11. Chart recorder
12. Foam generation cell
13. Syringe pump
14. Surfactant solution
15. Air.

Figure 3.3.4 Schematic of experimental equipment

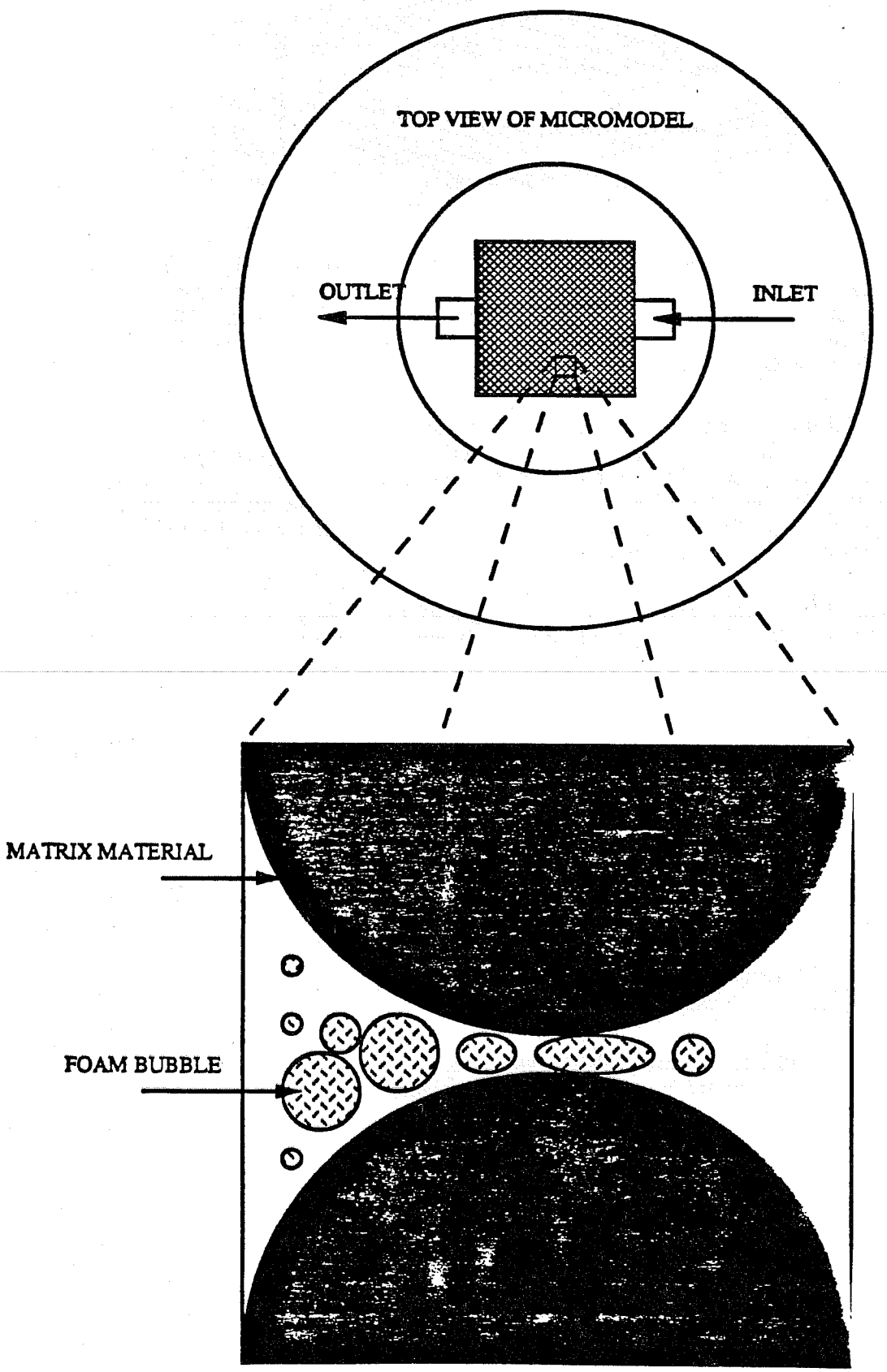


Figure 3.3.5 Schematic of foam flow through micromodel

2. Investigate the effects of medium wettability in a homogeneous flow channel micromodel. A micromodel will be made oil-wet by soaking the model in crude oil for an extended period of time to allow the deposition of polar components on the "rock" surfaces. Foam will then be injected at as low a flow rate as practical, and the pressure drop and flow characteristics will be recorded.

3. Compare Owete's results to those in a Berea sandstone replica micromodel. Air will be injected into a surfactant-saturated micromodel representing Berea sandstone at a rate of $2.5 \times 10^{-4}$ cc/s and the recorded pressure drop and general flow characteristics observed will be compared to the results obtained from the homogeneous micromodel. Additional runs at flow rates near one foot per day will be attempted.

4. Investigate the effects of medium wettability in a Berea sandstone replica micromodel. A Berea replica micromodel will be soaked in crude oil for an extended period to allow adsorption of the crude's polar components on the surfaces of the model's flow paths. Foam will then be injected at a flow rate as near to one foot per day as possible, and the pressure drop and flow characteristics will be recorded.

5. Investigate oil-foam interactions in both homogeneous flow channel and Berea replica micromodels. Foam will be injected to displace oil from both the homogeneous micromodel and the Berea replica micromodel. Oil saturation at the start of the foam flood for these investigations will be 100% in one series of tests, and residual oil saturation in the other series of tests. For both series, the pressure drop histories across the micromodel and the flow characteristics will be recorded.

An investigation into methods of obtaining images of the flowing foam will be made. Currently, the applicability of real time tomography techniques to the work described is being determined.

### 3.3.3 REFERENCES

1. Bond, D.C. and Holbrook, O.C.: "Gas Drive Oil Recovery Process", U.S. Patent 2,866,507 (1958).

2. Marsden, S.S.: "Foams in Porous Media", Supri TR-49, DOE Contract No. DE-AC03-81SF11564, May, 1986.

3. Owete, O.S., and Brigham, W.E.: "Flow of Foam Through Porous Media", Supri TR-37, DOE Document No. DOE/SF/115646, July, 1984.

4. Ettinger, R.A. and Radke, C.J.: "The Influence of Texture on Steady Foam Flow in Berea Sandstone", Presented at 64th annual Conference of SPE, San Antonio, TX, Oct. 8-11, 1989.

## 3.4. THREE DIMENSIONAL LABORATORY STEAM INJECTION MODEL
(Birol M.R. Demiral)

The objectives of this project are to observe the oil recovery mechanisms of steamflood and steam-foam injection in a 3-D laboratory model by using Computer Aided Tomography (Cat scanning). A stepwise approach is planned to achieve this goal: 3-D model development, and steam and steam foam injection experiments using Cat scanning.

### 3.4.1. 3-D MODEL DEVELOPMENT

The objective of a 3-D laboratory model is to represent field applications realistically in the laboratory. The starting point originally was to have radial flow in the model, and it was proposed to have a cylindrical shape for the model as shown in Figure 3.4.1. Although this model had the advantage of complete radial flow, it had some obvious disadvantages too:

1. Considering the dimensions of the scanning field of the SUPRI Cat scan (maximum 31 cm), the distance between the injector and the producing zone would be only 10 cm.

2. It would be difficult to sustain a uniform back pressure in the producing zone.

3. It would be almost impossible to clean, dry, and saturate the model between the runs.

Considering the importance of these disadvantages, the proposed design was changed to a pie shape (Figure 3.4.2) so that the injector-producer distance could be increased to 20 cm. There would be complete radial flow due to the cylindrical symmetry of the model. However, this symmetry introduced large heat losses through the sides. Also, the asymmetry at the producing annulus was a problem. There also were the other disadvantages of the previously proposed cylindrical shape, namely, sustaining constant backpressure in the producing zone and cleaning and saturation problems.

The next proposed shape was a diamond shaped model, obtained by adding a triangular area to the producing zone of the pie shaped model as shown on Figure 3.4.3. By so doing, the asymmetry and the difficulty of sustaining a uniform backpressure at the producing zone of the pie shaped model were eliminated. As shown, the diamond shaped model had only one producing corner instead of a large producing zone. However, the problems of heat losses through the sides and saturating the model after each run were left unsolved.

Considering the disadvantages of a diamond shape it was decided to construct a 3-D box which would represent 1/4th of a 5 spot pattern. However, all temperature and pressure readings would be done in the diamond part of the box as shown in the shaded portion in Figure 3.4.4. By so doing, it would be assumed that the heat losses through the sides of the diamond would be acceptable as compared to that for the previously proposed shapes. This was later changed to monitoring temperatures and pressures everywhere in the system, since scanning through the model would be difficult as discussed later.

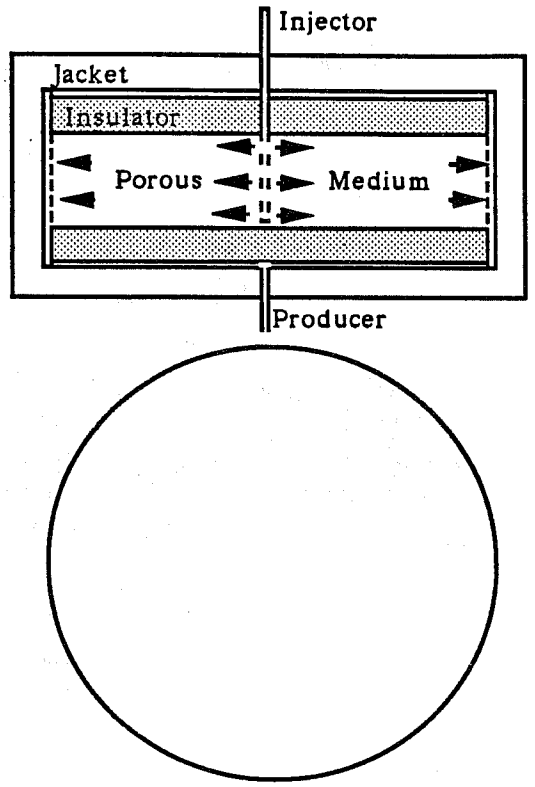


Figure 3.4.1 Cylindrical shape 3D model (proposed)

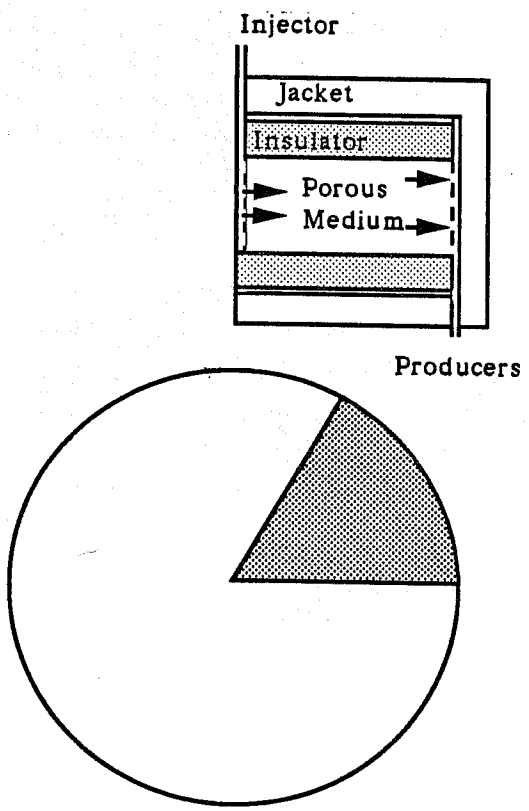


Figure 3.4.2 Pie shape 3D model (proposed)

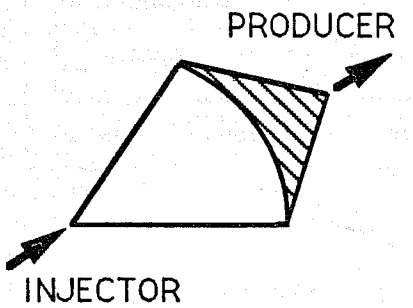


Figure 3.4.3 3D diamond shaped model (proposed)

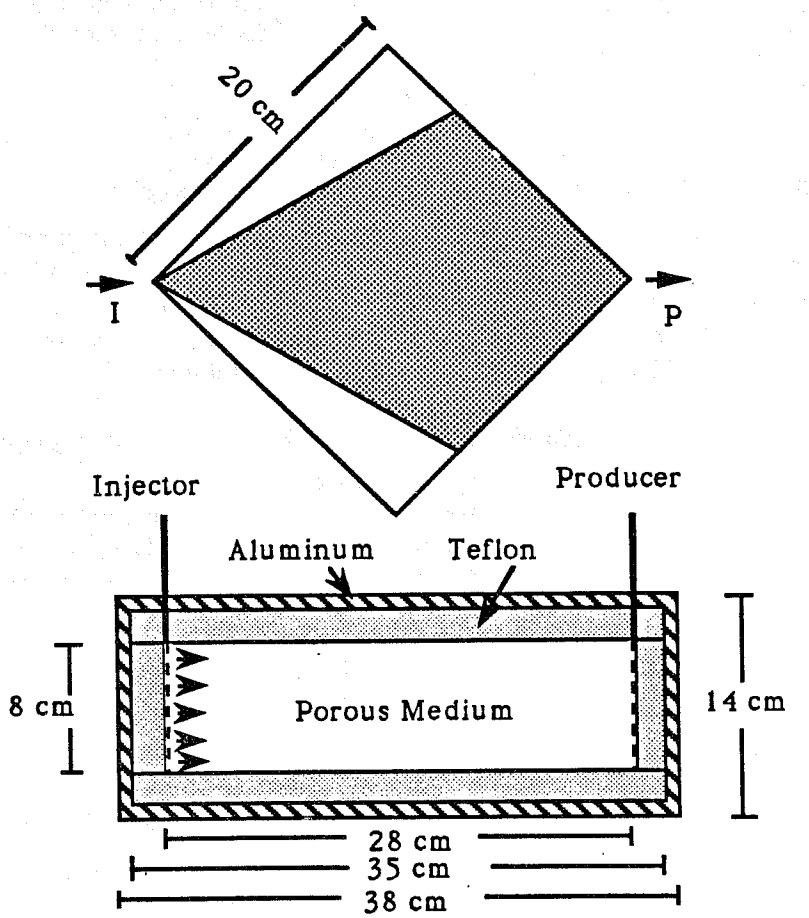


Figure 3.4.4 Proposed 3D box

As can be seen from the injector producer diagonal cross-section of the model, the heat insulation (Teflon) is in direct contact with the porous medium. We felt it was necessary to use Teflon in contact with the porous medium because of chemical and temperature stability. Fortunately Teflon has a fairly low thermal conductivity (0.1333 BTU/hr-°F-ft). The rate of heat transport in the porous medium (by means of conduction and convection) would be much faster than that of conductive heat transport in the aluminum construction material. Aluminum was necessary to support the Teflon for strength under the proposed pressure and temperature conditions. Aluminum was chosen as the construction material since it absorbs less x-ray energy than other materials. The Teflon box was to be sealed against gas or liquid leaks by using Chemgrip, a special epoxy which bonds Teflon to Teflon or Teflon to metal.

While searching for the optimum heat insulation system for the model, we considered Kynar (a high molecular weight thermoplastic polymer) as an additional insulator as shown in Figure 3.4.5. The thermal conductivity of Kynar is almost half that of Teflon (0.0667 BTU/hr-°F-ft versus 0.1333 BTU/hr-°F-ft). With the same insulation thickness, the resistance to heat flow will be increased using Kynar. This difference will be discussed later. However, Kynar had disadvantages such as cost and working temperature. The cost of Kynar was almost $500.00 for a square foot plate, and the working temperature was 300 °F maximum. We concluded that another insulation material as good as Kynar was necessary. We chose Fiberfrax, a ceramic fiber insulating material which is inexpensive and can be applied as a wet putty which air dries to a semi-permanent cast. Its thermal conductivity is even less than that of Kynar (0.04830 BTU/hr-°F-ft at 320 °F).

### 3.4.2. PRELIMINARY HEAT TRANSFER CALCULATIONS

Although we would like to prevent heat losses through the walls of the model, there will be some heat loss during the experiments. This heat loss should be computed to decide:

1. The total thickness of the insulation (within the limits of the scanning area) and the relative ratios of teflon and fiberfrax (or kynar) thicknesses.

2. The optimum steam injection rate for which a steam zone could develop.

Preliminary heat calculations were made assuming steady state conditions at steam temperature on the inner surface of the 3-D model. The resultant calculated heat loss would be a maximum estimate and design values for insulation material and steam injection rate would be within allowable limits. Assumptions used were:

1. The 3-D model is surrounded by a composite heat insulator as shown in Figure 3.4.6.

2. The inner surface temperature of this insulator is suddenly brought to the steam injection temperature (313 °F at 70 psig). The calculated heat loss using this assumption will be a maximum for a steam injection experiment in this model.

3. Steady state heat transfer conditions prevail.

4. The heat transfer mechanism between the outer surface of the insulator and air (at 68 °F) is natural convection only.

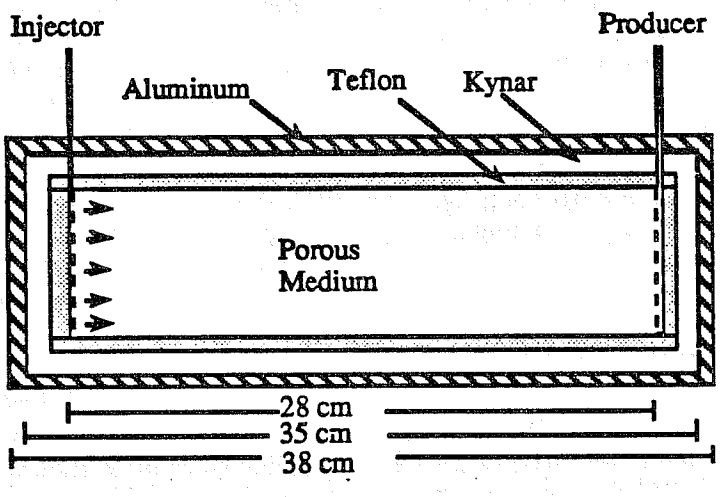


Figure 3.4.5 Insulation varieties

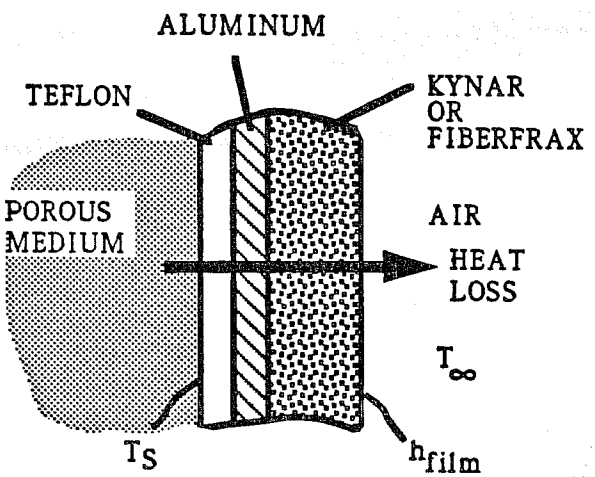


Figure 3.4.6 Composite wall representation of the insulator

Thermal resistance of this model can be written using the analogy between heat transport and ohms law:

$$R_t = \sum_{i=1}^{3} \left[ \frac{x}{kA} \right]_i + \frac{1}{h_{film} A} \tag{3.4.1}$$

Hence the rate of heat loss is:

$$\dot{Q}_L = \frac{T_s - T_\infty}{\sum_{i=1}^{3} \left[ \frac{x}{kA} \right]_i + \frac{1}{h_{film} A}} \tag{3.4.2}$$

where $A$ = Cross-sectional area to heat flow.

The cross-sectional area to heat flow for a 3D box is not constant but increases from inside to outside. Therefore the shape factor for a parallelpiped shell is introduced:

$$S = \frac{A_i}{x} + 2.16\,(a+b+c) + 1.2\,x \tag{3.4.3}$$

where:

$A_i$ = inside area
$a, b, c$ = inside dimensions
$x$ = the thickness of the shell (Figure 3.4.7)

In this shape factor the edges and the corners of the box were considered. The rate of heat loss can be determined from:

$$\dot{Q}_L = \frac{T_s - T_\infty}{\sum_{i=1}^{3} \left[ \frac{1}{kS} \right]_i + \frac{1}{h_{film} A_{out}}} \tag{3.4.4}$$

where:

$S_1$ = shape factor for teflon, ft
$S_2$ = shape factor for aluminum, ft
$S_3$ = shape factor for kynar or fiberfrax, ft
$A_{out}$ = Outside area of 3-D model, $ft^2$

Using Equation 3.4.4 for different combinations of thicknesses of insulation materials, the rate of heat loss was calculated and graphed in Figure 3.4.8.

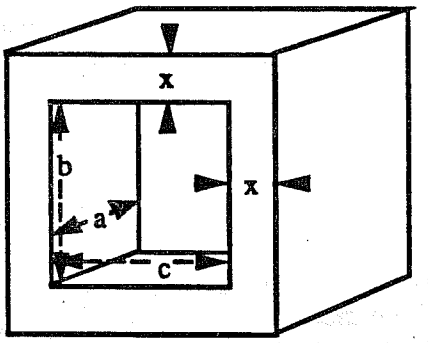


Figure 3.4.7 Parallelpiped shell assumption

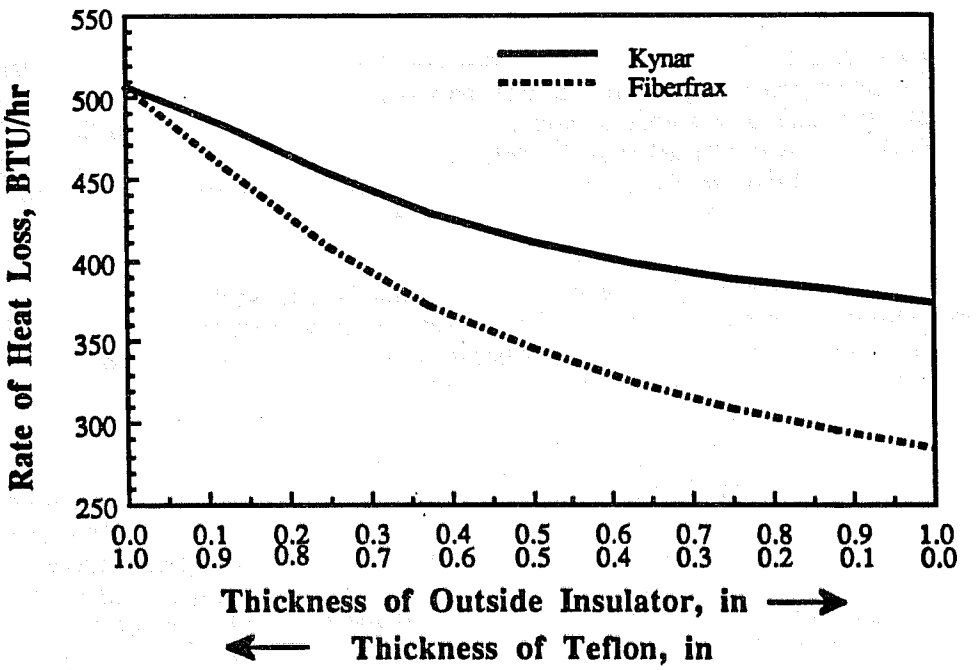


Figure 3.4.8 Total heat loss rate with different insulation material combinations

The total heat lost was also calculated during a steam injection run in which 1.0 PV of steam was injected (Figures 3.4.9 and 3.4.10). In Figures 3.4.11 and 3.4.12 rates of heat loss were calculated with and without the shape factor and compared.

After analyzing these results the optimum thickness combination for the proposed experimental conditions was chosen as 1/4" Teflon, 1/4" Aluminum and 3/4" Fiberfrax. Notice from Figure 3.4.10 that this combination allows the steam to sweep the entire model even at a rate as low as 2.0 ml/min.

### 3.4.3. QUALITY OF THE PRELIMINARY SCANS OF THE MODEL

Some preliminary work was done to determine whether the proposed model was catscannable. To do this, a mock-up model which was an aluminum box filled with sand was scanned under different combinations of scan speeds, photomultiplier and detector levels, scan modes and energy levels. During the first attempt two problems were observed.

1. Since the Cat scan was designed to x-ray a human body whose shape is mostly smooth and cylindrical, the asymmetric shape of the model was not ideal for obtaining good scan pictures.

2. The regular padding material used in hospitals for controlling x-ray attenuation could not be used satisfactorily.

Due to these two reasons, at first it was not possible to get good pictures because of artifacts and computer processing errors. It was necessary to find a suitable material which would act as an attenuator or absorber of x-rays in the proper areas of the scan field. Finally "play-doe", which is a water based clay modeling material, was found to have the proper characteristics. As a solution to the asymmetric scanning object problem, an aluminum tube (11.5" inside diameter and 1/4" wall thickness) was introduced around the mock-up model.

As can be seen in Figure 3.4.13, good pictures could be taken when the aluminum tube and play-doe were used around the model. To be sure of good results, water and oil were injected into both sides of the model to see whether it would be possible to distinguish the different saturating fluids in the porous medium by catscanning. Figure 3.4.14 shows that this method gave a satisfactory result.

After preliminary investigations, the actual 3D model was constructed, filled with sand and scanned together with "playdoe" around it. The surrounding aluminum tube was not used because resultant pictures were good without it. In this case, the CT numbers were calculated and compared from the both the dry and water saturated sand. Figures 3.4.15 and 3.4.16 show samples of these pictures. The top picture shows the model filled with dry sand and shows settling in the top portion of the model. The bottom picture represents the same cross-section after adding more sand to the model and injecting water from the left hand side. According to theory, there must be a 200 CT unit difference between dry sand and wet sand. This difference was verified in both attempts at two different power levels. This shows that it will be possible to differentiate saturating fluids in the model by comparing their CT numbers as well as by visual comparison.

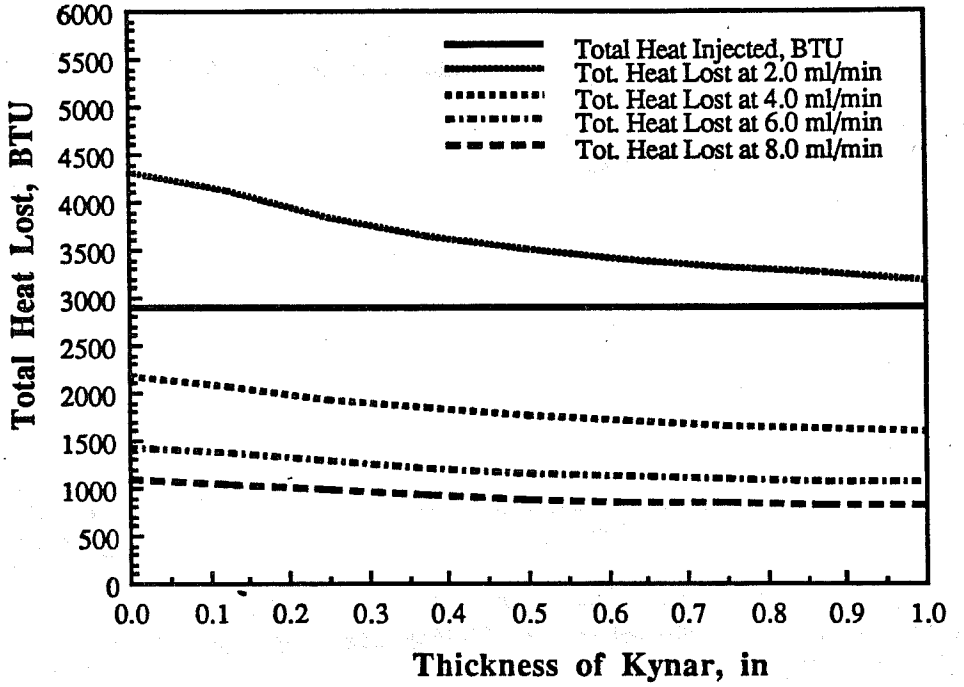


Figure 3.4.9 Total heat loss versus thickness of kynar for several injection rates after 1 PV of steam injection (insulator = teflon and kynar)

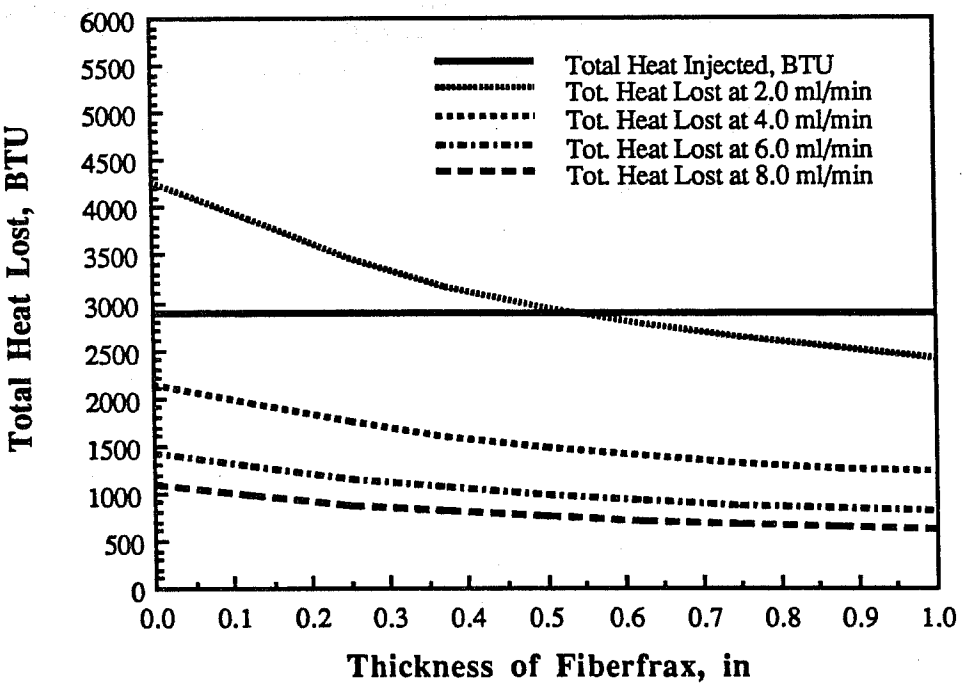


Figure 3.4.10 Total heat loss versus thickness of fiberfrax for several injection rates after 1 PV of steam injection (insulator = teflon and fiberfrax)

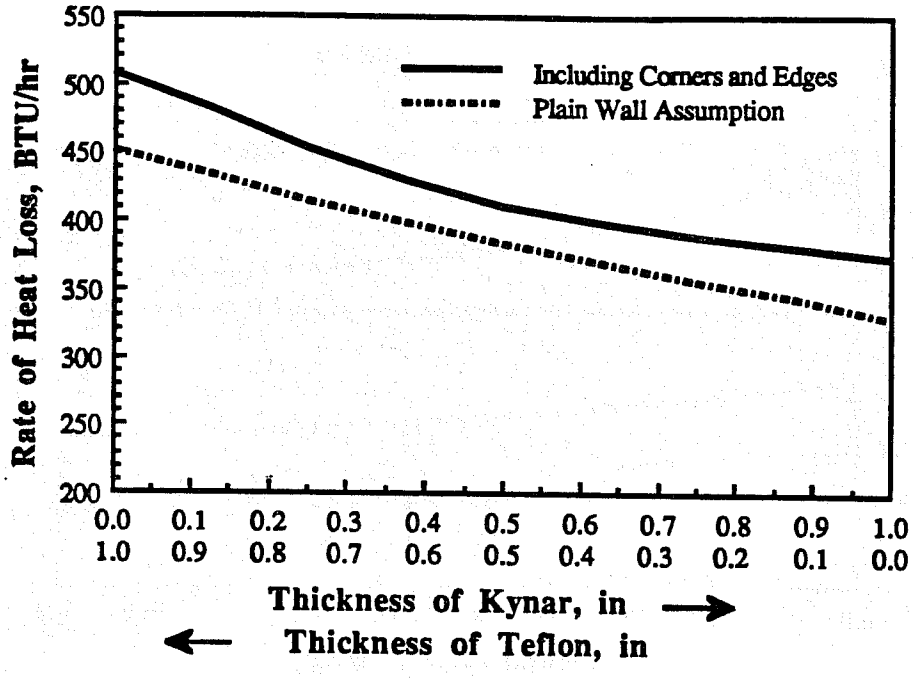


Figure 3.4.11 Total heat lost with and without the effects of corners and edge (insulator = teflon and kynar)

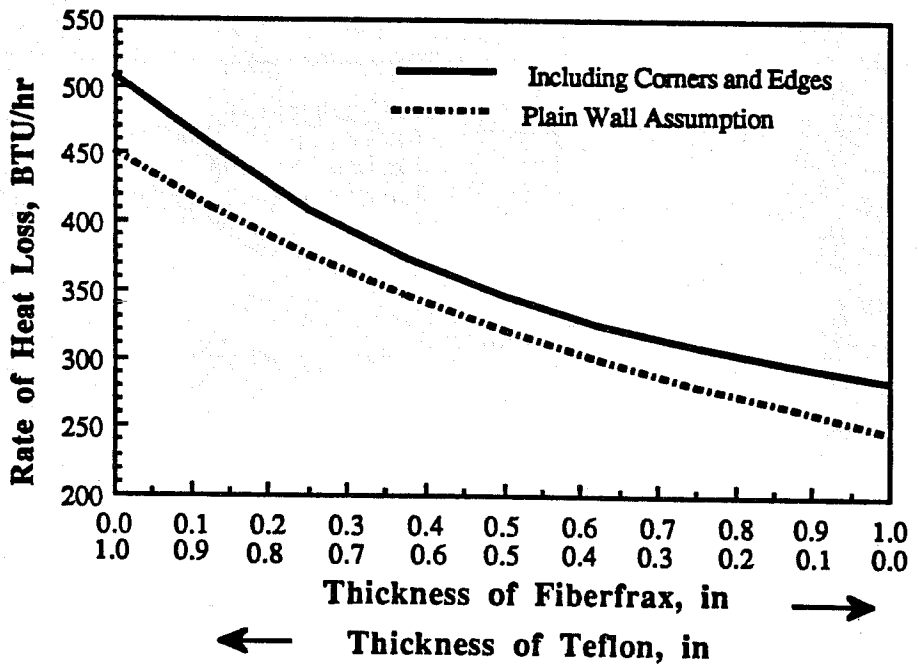


Figure 3.4.12 Total heat lost with and without the effects of corners and edges (insulator = teflon and fiberfrax)

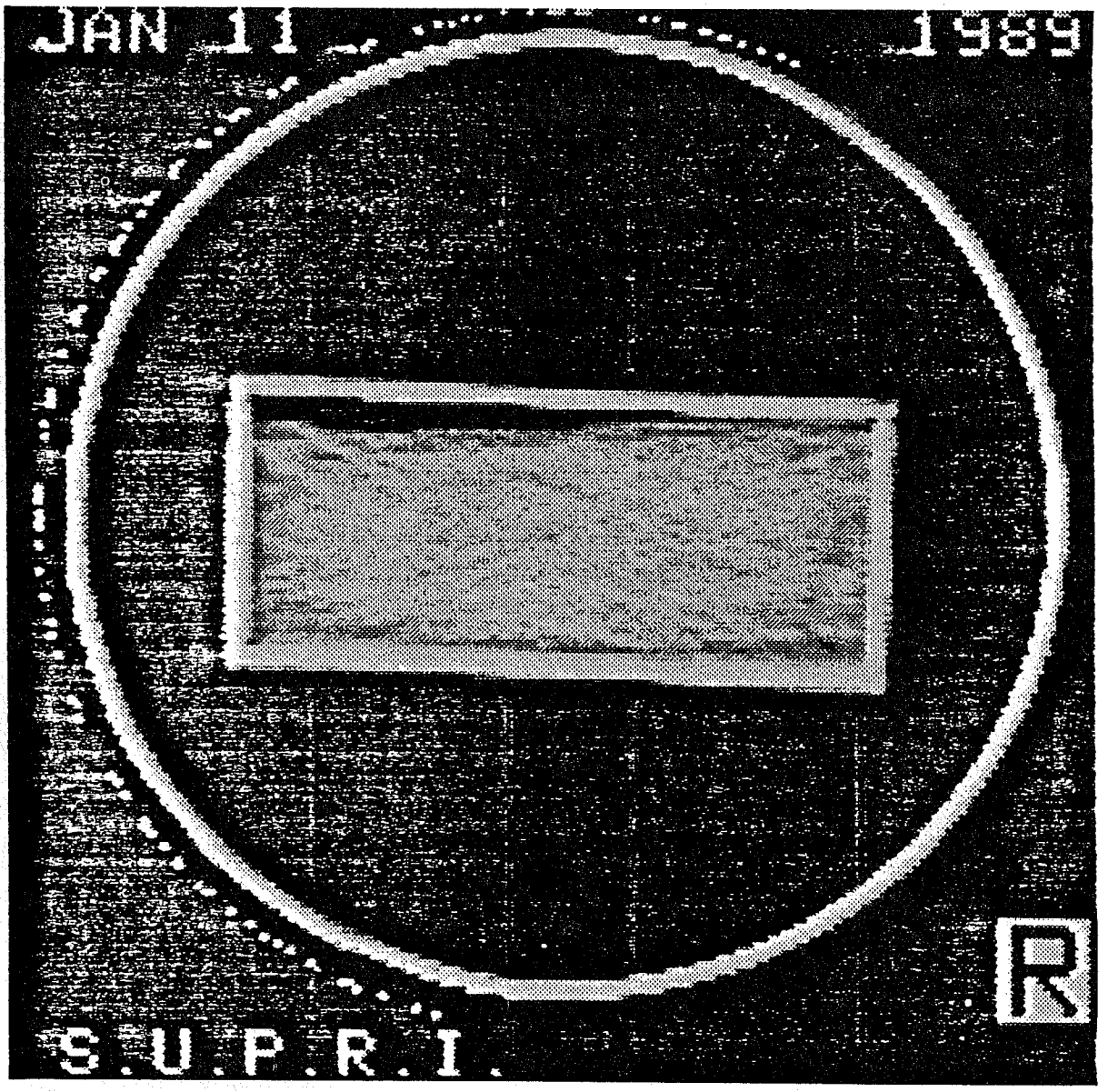


Figure 3.4.13 Scan picture of mock-up model within aluminium tube

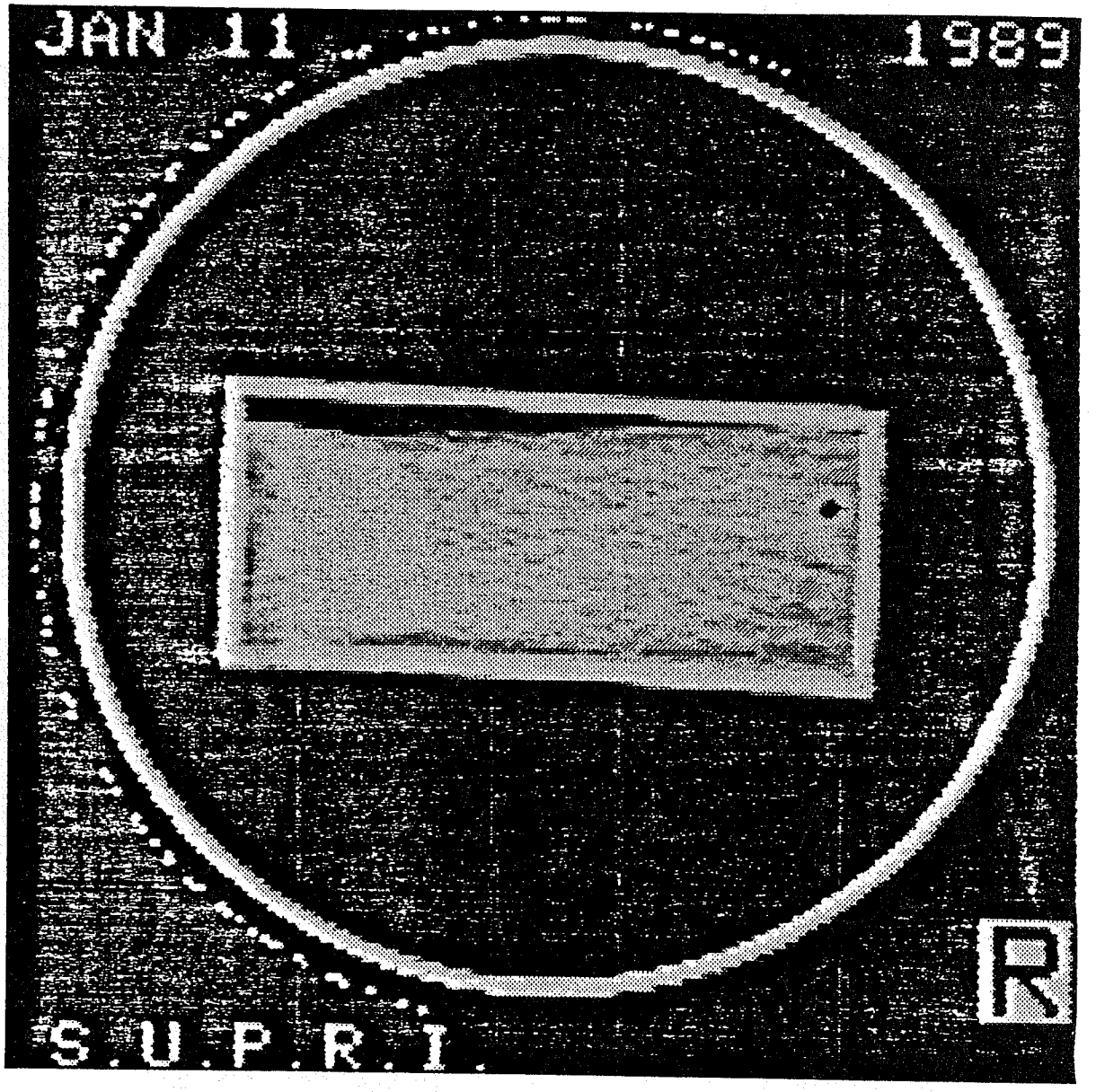


Figure 3.4.14 The same slice after injecting water and oil from either corner

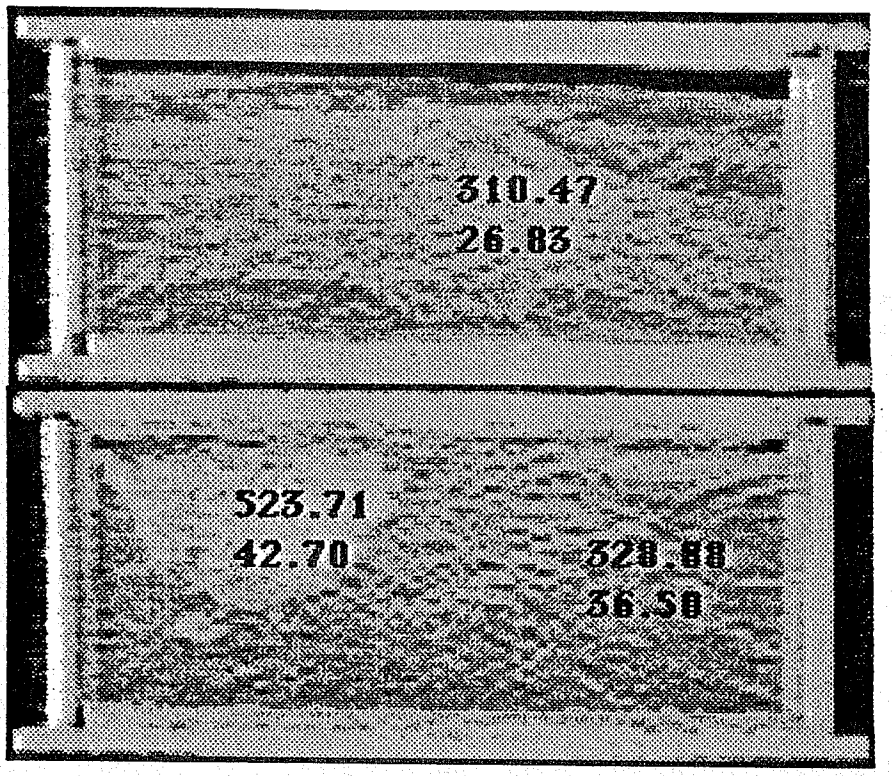


Figure 3.4.15 Scan pictures of the 3D model before and after water injection (140 kV)

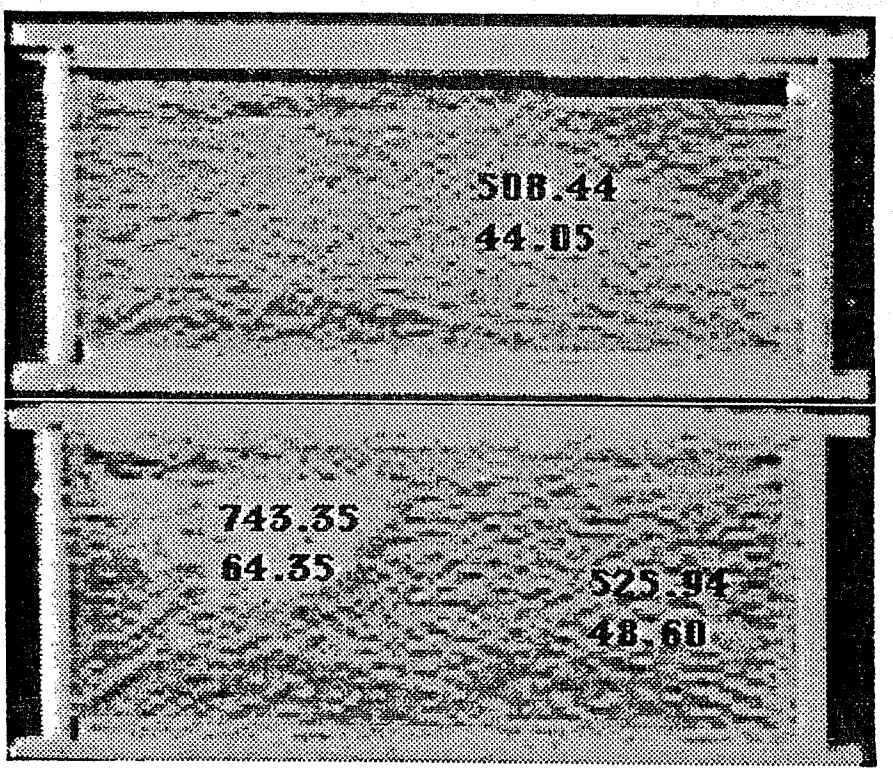


Figure 3.4.16 The same section of the 3D model before and after water injection (100kV)

### 3.4.4. RECENT MODIFICATIONS

Recent modifications are:

1. The top cover of the box has been modified such that the cover can compress the porous medium to assure there is no gas cap above it (Figure 3.4.17).

2. The injection well system is designed to allow injection of 100% steam through the total depth of the well. This is done by introducing a heater cartridge within an aluminum rod through which the steam flows, as shown on Figures 3.4.17 and 3.4.18.

3. The main insulation sequence was changed to Teflon+Aluminum+Fiberfrax instead of Teflon+Fiberfrax+Aluminum.

4. The thermocouple and pressure tap locations were chosen as shown in Figure 3.4.19. Scanning will be done through the clear area, which has a width of 1.5 cm between thermocouples.

5. The positioning tables were modified as shown in Figure 3.4.20. By using two tables, the 3D model can be precisely positioned at the proper locations within the scan field.

### 3.4.5. EXPERIMENTAL SET-UP

A schematic flow diagram of the experimental apparatus can be seen in Figure 3.4.21. There are three parts: an injection port, 3D steam injection model, and the production port.

In the injection port there are two liquid chromatography pumps. One is used to inject water or surfactant solution, and the other is to feed the steam generator with distilled water. There is also a gas mass flow controller which will be used to inject Nitrogen at a constant rate into the model during the experiments.

The 3D steam injection model has a total of 38 J-type (Iron-Constantan) thermocouples which are located at three different levels in the model. Sixteen of them, center thermocouples, were placed at a level of 1.5" from the bottom of the model. Eleven top and eleven bottom thermocouples were placed at 2.75" and 0.25" from the bottom respectively. Sixteen pressure taps (only eight of them will be used during the experiment) were located at the same places as the center thermocouples.

A back pressure regulator will be used to maintain a constant pressure at the producing corner of the model. A cooler will be used to condense the produced steam.

### 3.4.6. FORTHCOMING STEPS OF THE PROJECT

Calibration experiments will be carried out according to the following procedure:

1. The 3D model will be scanned dry.
2. The 3D model will be evacuated.

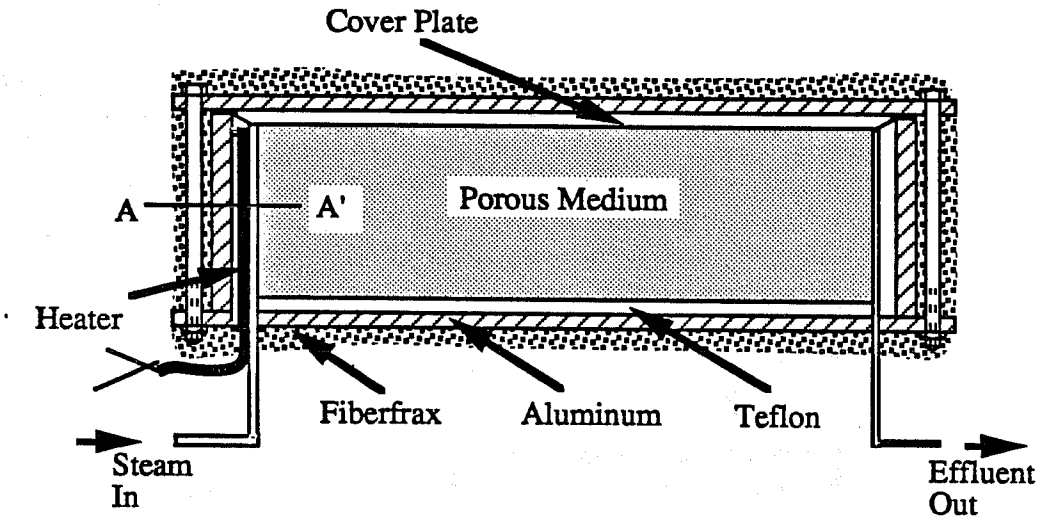


Figure 3.4.17 Injector-producer diagonal cross-section of the 3D model

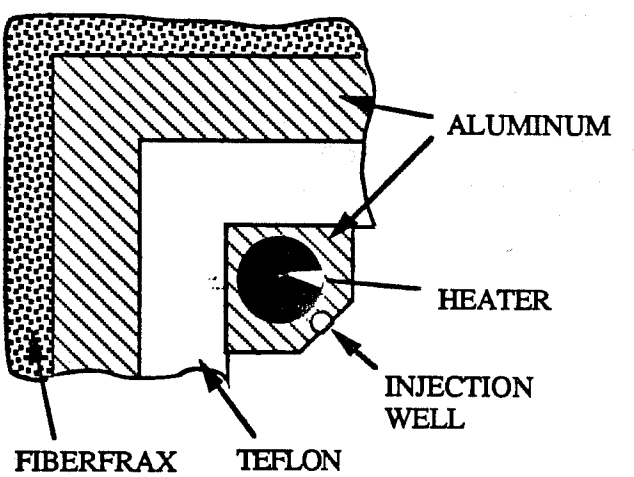


Figure 3.4.18 A-A' cross-section of the injection well

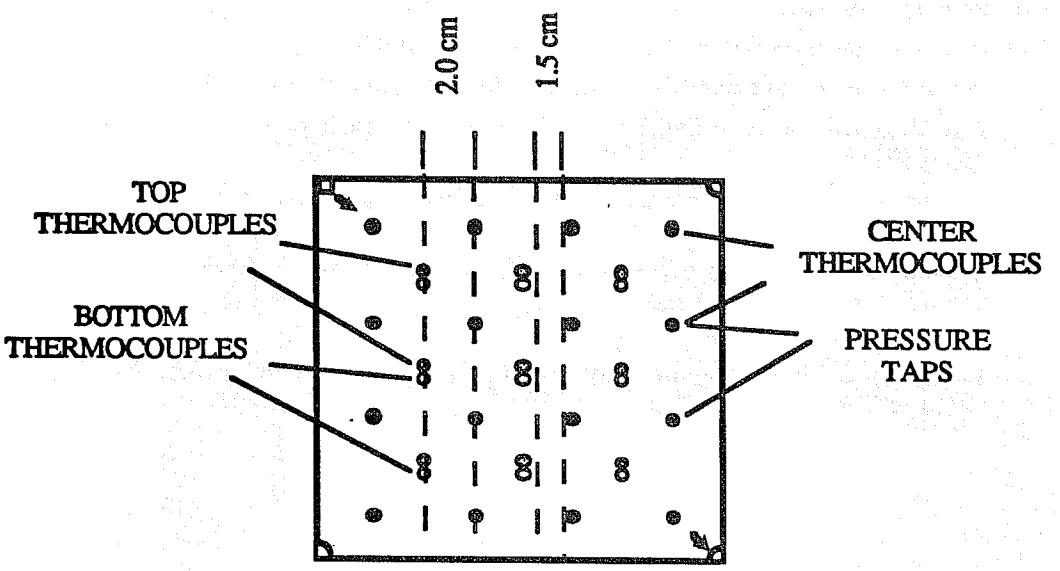


Figure 3.4.19 Locations of thermocouples and pressure taps on 3D model

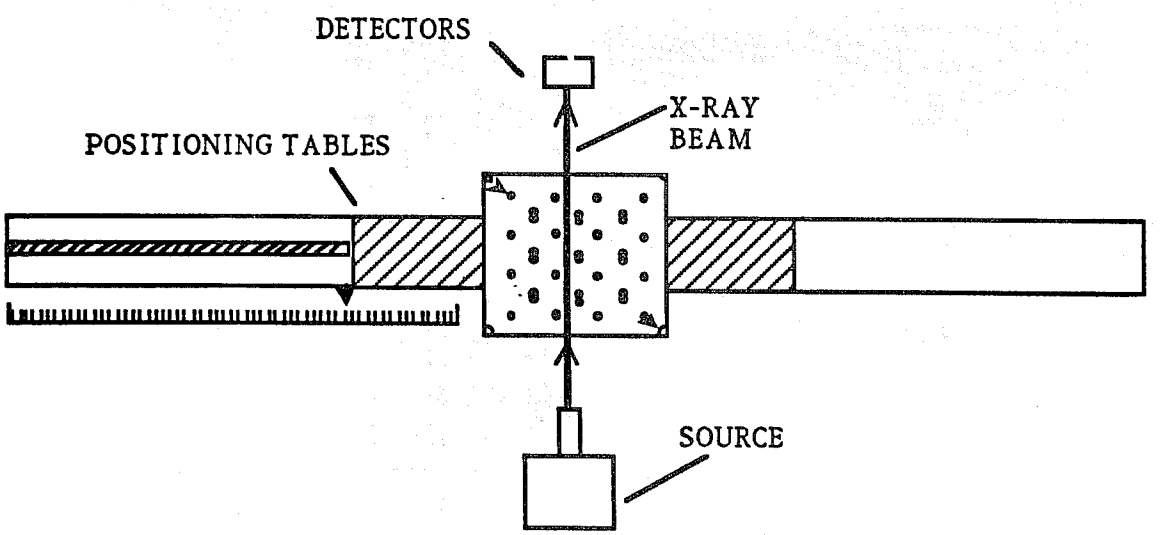


Figure 3.4.20 CATSCAN positioning table

3. The 3D model will be saturated with water.
4. The initial saturation distribution will be scanned. If we are not satisfied with the homogeneity of the medium, water injection will be continued until 100% water saturation is achieved.
5. Continuous steam injection will be started, during which:
   a) temperature and pressure data will be taken at 1 minute intervals,
   b) scan data will be recorded every 12 minutes at each of the 6 to 8 sections at two different energy levels, and
   c) production will be measured every 12 minutes to make overall material balances.
6. The scan data will be analyzed to calibrate the CT numbers at two different energy levels, for air, water and steam saturated sand.

After measuring the CT numbers, the future scan pictures and CT values can be analyzed in terms of saturation within the model at a given time.

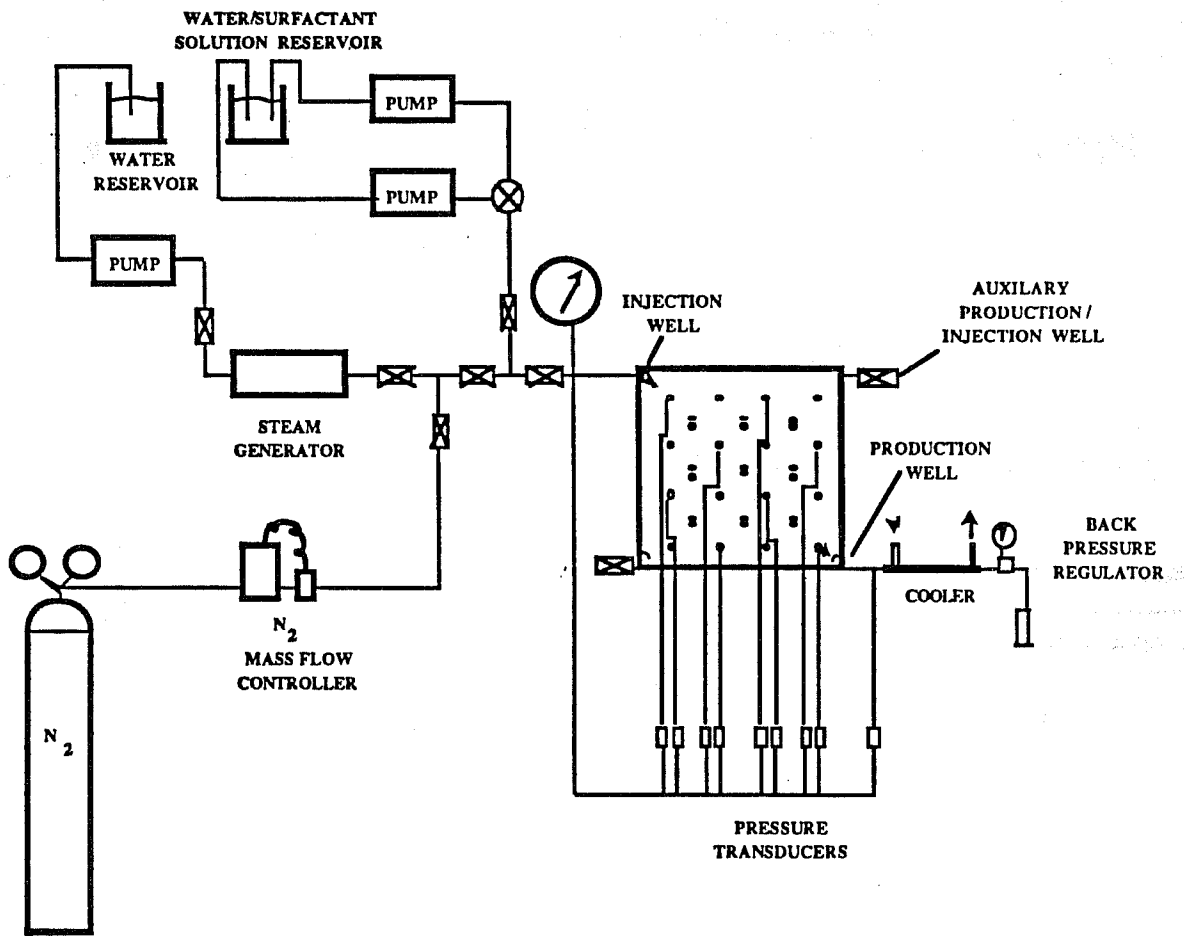


Figure 3.4.21 Schematic flow diagram of the 3D steam injection model

# PROJECT 4: RESERVOIR DEFINITION

Reservoir definition is a key to application of findings from other projects. The science and engineering of energy fluid recovery from porous rocks is tied to knowledge of the rocks. This project involves developing and improving techniques of reservoir formation evaluation such as tracer tests, pressure transient tests, and ancillary methods.

## 4.1 THEORETICAL DEVELOPMENT OF FLOW INTO THE WELL THROUGH PERFORATION
(G. Ahmed)

A technical report on this topic is in the draft stage. The following is an abstract of this work.

A theoretical solution to flow into a well via perforations is synthesized using Green's functions. The solution is three dimensional and applies to steady-state single phase homogeneous flow. The complete solution for a cylindrical perforation involves double infinite summation and triple integration and is difficult to compute. A useful approximation is made by treating the perforation as a line-sink; this reduces the solution to double infinite summation and a single integration.

The solution contains expressions of Bessel functions and their derivatives. The infinite summation is over the order and the argument of these functions. An array of eigenvalues are first computed from an implicit equation. These eigenvalues are then used for computation of a solution.

The solution involves five physical parameters: wellbore diameter, perforation diameter, perforation length, perforation density (vertical spacing) and phasing (angular spacing). These parameters influence the cost as well as the efficiency of a well completion. A sensitivity analysis can be done for an optimization of the completion design using this analytical solution.

Perforation length is the most important parameter and performance improves with increasing length. Initially, even a small increase in length gives a significant improvement. Perforation density is an important parameter, but beyond an optimum number of shots per foot there is little gain in productivity ratio. This result will lead to a saving of cost, since a higher shot density is generally used by industry. The phasing of perforations influences the performance. A phasing of 90° in the same horizontal plane or along a spiral gives a significant advantage over 0° phasing, and this improvement increases with an increase in perforation length.

Further work is needed to extend the solution for uniform potential but variable flow rate along the length of a perforation.

## 4.2 ANALYSIS OF RADIAL TRANSPORT OF REACTIVE TRACERS IN POROUS MEDIA (G.K. Falade)

A paper titled "Analysis of Radial Transport of Reactive Tracers in Porous Media," by G.K. Falade and W.E. Brigham, was published in SPE Reservoir Engineering (February 1989). The following is a summary of this paper.

The paper presents new closed-form analytical solutions of equations describing radial transport of reactive tracers in porous media under conditions of tracer adsorption, nonuniform convection, and variable coefficients of dispersion. Three different types of variable dispersion coefficients were considered, and exact solutions presented in Laplace Space. The special case where shear-mixing or convection dominates dispersion, which is important for tracer test studies, was programmed for concentration profiles for continuous and slug-injection test models.

## 4.3 PRESSURE TRANSIENT ANALYSIS FOR COMPOSITE SYSTEMS
(A. Ambastha)

A technical report titled "Pressure Transient Analysis for Composite Systems," SUPRI TR 68, was published in August 1989. The following is an abstract of this report.

A composite reservoir model was used to analyze well-tests from a variety of enhanced oil recovery projects, geothermal reservoirs, and acidization projects. A composite reservoir is composed of two or more regions. Each region has its own rock and fluid properties. Transient pressure behavior of a well in a two-region composite reservoir has been considered extensively in the literature, and several methods have been proposed to estimate front (or discontinuity) radius, or swept volume. This study considers transient pressure derivative behavior for a well in a two-region composite reservoir to establish the applicability and the limitations of different methods to estimate front radius or swept volume. A finite-radius well with wellbore storage and skin was assumed to produce (or inject) at a constant rate. Three outer boundary conditions were considered: infinite, closed, and constant-pressure. A study of drawdown and buildup responses resulted in a set of correlating parameters for the pressure derivative responses, and new design and interpretation relations for well-tests in composite reservoirs. Guidelines were presented for the applicability of different methods to estimate front radius. Producing time effects on buildup responses showed that analyzing a well-test after a short producing (or injection) time may be difficult.

Dynamic phenomena, such as phase changes and multi-phase flow effects in a region near the front, can cause a sharp pressure drop at the front. A sharp pressure drop was modeled as a thin skin at the front in this study. An analytical solution for transient pressure behavior of a well in a two-region composite reservoir with a skin at the front was obtained using Laplace transformation. A thin skin at a front can explain a short-duration pseudosteady state even for small mobility and storativity contrasts. The effects of a skin at a front are similar to the effects of storativity ratio. Thus, neglecting a thin skin at the front can cause large errors in parameter estimation using a type-curve matching method.

Pressure derivative behavior of a well in a homogeneous, or a three-region composite reservoir was also discussed. Several well tests from composite reservoirs were analyzed to establish the applicability and the limitations of the deviation time method to estimate front radius.

## 4.4 DEPENDENT VARIABLES FOR DISPERSIVE MODELS
(I. Kocabas)

A major objective of this project is the study of the formulation of mathematical equations describing dispersive models, and classification of their solutions in terms of various dependent variables. Another objective is the use of these concepts in material balance calculations in simulators and in analysis of tracer-return profiles from laboratory and field experiments. This work was initiated in the Stanford Geothermal Program during an investigation of tracer and thermal transients due to injection of cold water. This report discusses additional work performed since that time.

Many physical processes of enhanced oil recovery (EOR) are governed by a convective-dispersive mechanism: heat transport during thermal methods, miscible and immiscible displacement of oil, and tracer studies. The following is a discussion of the formulation of dispersive models in terms of several dependent variables commonly used in tracer studies. The concepts are general and apply to processes governed by convective-dispersive mechanisms.

A variable of a system is a characteristic that may be measured, and which assumes different numerical values when measured at different times[12] The resident concentration, $C_R$ (the amount of the tracer per unit volume of the system at a given instant), has usually been taken as the variable of a system. On the other hand, the flux concentration, $C_F$ (ratio of the tracer flux to the volumetric flux), has been the most commonly measured quantity. As a result, tracer return profiles have been graphed by using the flux concentration as the output variable. These two concentrations always differ when a system is dispersive. Consequently, whenever a dispersive model is used for interpreting tracer return profiles, failure to distinguish between the two concentrations leads to the use of solutions derived for the wrong initial and boundary conditions.

If a dispersive model is used, the constitutive relation describing flux is:

$$J = u\ C_R - D\ \frac{\partial C_R}{\partial x} \tag{4.4.1}$$

where $J$ is the total flux, $u\ C_R$ is the convective flux, and $D\ \partial C_R/\partial x$ is the dispersive flux.

From the definition of the flux concentration:

$$J = u\ C_F \tag{4.4.2}$$

Substituting Eq. 4.4.2 in Eq. 4.4.1 and rearranging yields:

$$C_F = C_R - \frac{D}{u}\ \frac{\partial C_R}{\partial x} \tag{4.4.3}$$

Eq. 4.4.3 serves for finding $C_F$ when the theoretical form of $C_R$ is known. The next section presents formulations of the governing equations of dispersive systems in terms of the three dependent variables, $J$, $C_R$ and $C_F$.

### 4.4.1 DEPENDENT VARIABLES FOR DISPERSIVE MODELS

A one-dimensional linear dispersive system is represented by:

$$f\,\frac{\partial C_R}{\partial t} + u\,\frac{\partial C_R}{\partial x} - D\,\frac{\partial^2 C_R}{\partial x^2} + q = 0 \tag{4.4.4}$$

Eq. 4.4.4 may be derived by applying a material balance. The parameter $f$ represents flowing fraction of the system and the value must be $0 < f \leq 1$. The source term, $q$, can consider several phenomena, such as chemical reaction, adsorption, and molecular diffusion into the adjacent porous matrix. Using the constitutive relation given by Eq. 4.4.1, the dependent variable $C_R$ may be transformed to $J$, to obtain:

$$f\,\frac{\partial J}{\partial t} + u\,\frac{\partial J}{\partial x} - D\,\frac{\partial^2 J}{\partial x^2} + uq - D\,\frac{\partial q}{\partial x} = 0 \tag{4.4.5}$$

Four forms of the source term, $q$ were considered. If the source term is equal to zero, then either $C_R$ or $J$ satisfy the convection-dispersion equation[9]. If there is no flow, then either variable satisfies the heat equation as pointed out by Carslaw and Jeager[10].

If the source term represents a linear reaction such that:

$$q = kC_R \tag{4.4.6}$$

either variable $C_R$ or $J$ satisfies the same equation[18].

In heterogeneous system models, the source term represents diffusion into the adjacent porous matrix. A heterogeneous system is characterized by preferential flow paths due to dead end pores[13], aggregates[19], fissures[3], fractures[15], or layering[8]. Tracer transport in a heterogeneous porous system may be modelled in four ways[6]:

1. the very near field,
2. the near field,
3. the far field,
4. the very far field.

These various models are related to the scale of heterogeneities with respect to the scale of flow.

Independent of the heterogeneous system it represents, the Laplace transformation of Eq. 4.4.4 is:

$$D\,\frac{\partial^2 \overline{C}_R}{\partial x^2} - u\,\frac{\partial \overline{C}_R}{\partial x} - (fs + g(s))\overline{C}_R = 0 \tag{4.4.7}$$

in which the Laplace transform of the source term $q$, corresponds to:

$$\bar{q} = g(s)\bar{C}_R \tag{4.4.8}$$

In Eq. 4.4.8, the function $g(s)$ depends on the approach used to model a heterogeneous system. See the attached Appendix 4.4.5 for derivation of $g(s)$ for heterogeneous system models and the classification of solutions of Eq. 4.4.7.

The Laplace transform of Eq. 4.4.5 is:

$$D\,\frac{\partial^2 \bar{J}}{\partial x^2} - u\,\frac{\partial \bar{J}}{\partial x} - fs\bar{J} - (u\bar{q} - D\,\frac{\partial \bar{q}}{\partial x}) = 0 \tag{4.4.9}$$

Substituting Eq. 4.4.8 into Eq. 4.4.9 results in:

$$D\,\frac{\partial^2 \bar{J}}{\partial x^2} - g(s)u\frac{\partial \bar{J}}{\partial x} - fs\bar{J} - g(s)(u\bar{C}_R - D\,\frac{\partial \bar{C}_R}{\partial x}) = 0 \tag{4.4.10}$$

Laplace transformation of Eq. 4.4.1 yields the relation between $J$ and $C_R$ in Laplace space:

$$\bar{J} = u\bar{C}_R - D\,\frac{\partial \bar{C}_R}{\partial x} = 0 \tag{4.4.11}$$

Substituting Eq. 4.4.11 into Eq. 4.4.10 yields:

$$D\,\frac{\partial^2 J}{\partial x^2} - u\,\frac{\partial \bar{J}}{\partial x} - (fs + g(s))\bar{J} = 0 \tag{4.4.12}$$

Equations 4.4.7 and 4.4.12 show that both functions $J$ and $C_R$ satisfy Eq. 4.4.4. The discussion on the dependent variables also applies if multiple sources such as a reaction term and a diffusion term exist in the system, or if three continua are superposed in the far field approach. In the case of the superposition of multiple continua in the far field approach, if a diffusive transport is considered between the two phases, a geometry and a size may be assigned to the immobile phase. Superposition of multiple continua is required due to existence of differing geometries, and also differing sizes of the same geometry.

A natural extension of multiple source terms is to assume the immobile phase size is a distribution function. This concept has been used successfully for fluid flow in porous media[7,11,16] modelled as superposition of multiple continua. Using the same procedure, the expressions for the source terms are derived in Appendix 4.4.5. The source function $g(s)$ for this case is equal to integration of $g(s)$ for single size over the size distribution function $(f(a))$. Since a size distribution can have a large effect on the pressure response, a similar effect should be seen on tracer distribution and tracer return profiles.

In the first three approaches of modelling heterogeneous systems, the transport equation in the immobile phase is also satisfied by two separate dependent variables namely, $C_m$ corresponding to $C_R$ and $J_m$ corresponding to $J$ of the mobile phase equation. These two variables $J_m$ and $C_m$ are also related by:

$$J_m = u\ C_m - D\ \frac{\partial C_m}{\partial x} \tag{4.4.13}$$

Three forms of $q$ satisfy the variable $J$; also any other variable obtained by dividing $J$ by a constant will satisfy Eq. 4.4.4. In fact, $C_F$, one of the two concentration variables used in tracer studies, is obtained by dividing $J$ by $u$.

If the source term represents a reaction of higher order, then Eq. 4.4.4 becomes nonlinear, and neither of the functions $J$ or $C_F$ satisfies Eq. 4.4.4. In such a case, $C_F$ does not lose physical meaning, and can be found from the theoretical expression for $C_R$ by using Eq. 4.4.3.

## 4.4.2 CLASSIFICATION OF SOLUTIONS

Since both concentration variables $C_R$ and $C_F$ satisfy Eq. 4.4.4, initial and boundary conditions determine whether the solution is in terms of $C_R$ or $C_F$. In solving mathematical equations, Brigham[9] explained the proper specification of the initial and boundary conditions based on these two concentration variables. Later, Kreft and Zuber[17] provided a classification of solutions of the convection-dispersion(CD) equation and the transformations linking the solutions. Parker and van Genuchten[20,22] discussed the same concepts, and showed that the averaging techniques lead to different boundary conditions.

Tables of the CD model $C_R$ and $C_F$ solutions for infinite systems are in the paper by Kreft and Zuber[17]. A similar table for finite system solutions is given by Barry and Sposito[5]. Kreft and Zuber[17] also give a table of transformations linking infinite medium solutions for different injection and detection modes.

Classification of solutions of dispersive models may be generalized by constructing a table of solutions for heterogeneous medium models. An improvement can be achieved by considering the source term as a distribution function. In this study, a table of instantaneous injection solutions for heterogeneous system models has been constructed (see Table 4.4.1 in the appendix) by using a standard source function. Explicit expressions are presented for several immobile phase geometries and extension to other geometries by using block geometry functions given by Barker[4]. The presence of a distribution of immobile phase sizes is treated by using probability distribution functions in a study of fluid flow in multiple porosity media. In addition, numerical differences between various solutions for a single fracture located in a porous matrix are compared as an example. Finally, effects of diffusion into an immobile phase are discussed by comparing numerical results from heterogeneous system model solutions with those for homogeneous system models. A homogeneous system is equivalent to a convection-dispersion (CD) model which has no source term.

A special case of heterogeneous medium models, the very-near field single fracture (AD) model, was first developed by Avdonin[2] to calculate the temperature distribution in an oil layer due to a hot fluid injection. The AD model's source function $g(s)$ that needs to be used in the table of heterogeneous system solutions, is derived in the appendix.

AD model solutions were computed for Peclet numbers 10, 33 and 100 and graphed in Figs. 4.4.1 to 4.4.3. Fig. 4.4.1 shows that numerical differences between AD model solutions are negligible for high ($P_e \approx 100$) Peclet numbers. For moderately dispersive systems ($P_e \approx 30$) numerical differences become more pronounced as in Fig. 4.4.2. When the system is highly dispersive ($P_e \approx 10$), numerical differences become significant [Fig. 4.4.3].

Tracer return profiles in Figs. 4.4.1 to 4.4.3 have nearly the same characteristics with those of the CD model solutions plotted in Figs. 4.4.4 and 4.4.5. However, the concentration values computed from the AD model solutions are significantly smaller than those computed from the CD model solutions.

Numerical differences between the CD model solutions and those of the AD model solutions may be compared by studying the function:

$$\psi = \left[ \frac{C_{IFF} - C_{IRR}}{C_{IRR_{max}}} \right] * 100 \qquad (4.4.14)$$

where $C_{IRR_{max}}$ is the peak concentration value of $C_{IRR}$.

The solution $C_{IFF}$ of the CD model describes the variation of flux in time and space, when an amount of tracer equal to $m$ is injected at $x = 0$ and $t = 0$. Due to injection and flow, an initially asymmetric tracer distribution is produced, the leading edge being longer than the trailing edge. Also, backward dispersive flux behind the peak is compensated by convective flux. This generates milder concentration gradients behind the peak than those ahead of it and increases the asymmetry of tracer distribution within the system.

The solution $C_{IRR}$ of the CD model requires that a tracer zone symmetrically distributed about the point $x = ut$ moves with the mean speed of flow, and grows as the square root of time.

$C_{IFF}$ and $C_{IRR}$ solutions of the CD model are related by:

$$C_{IFF} = \frac{x}{ut} C_{IRR} \qquad (4.4.15)$$

Based on this relation, the function $\psi$ becomes:

$$\psi = \frac{C_{IRR}}{C_{IRR_{max}}} \left[ \frac{t_w}{t} - 1 \right] * 100 \qquad (4.4.16)$$

According to Eq. 4.4.16, the absolute value of $\psi$ is proportional to absolute values of $C_{IRR}$ and $((t_w/t)-1)$. $C_{IRR}$ and $((t_w/t)-1)$ are competing elements. While the absolute value of the first increases, the second decreases.

At early times, as the leading edge passes the observation point, $C_{IRR}$ values increase with time reaching a maximum at $t = L/u$. Then $C_{IRR}$ values decrease with time becoming virtually zero after the trailing edge passes. Values of the $((t_w/t)-1)$ part of $\psi$ are maximum at

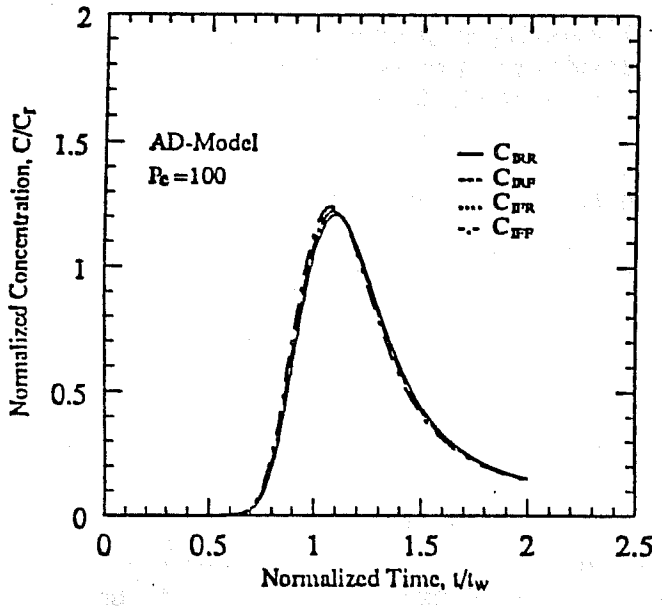


Figure 4.4.1 AD-Model Solutions for High Peclet Numbers

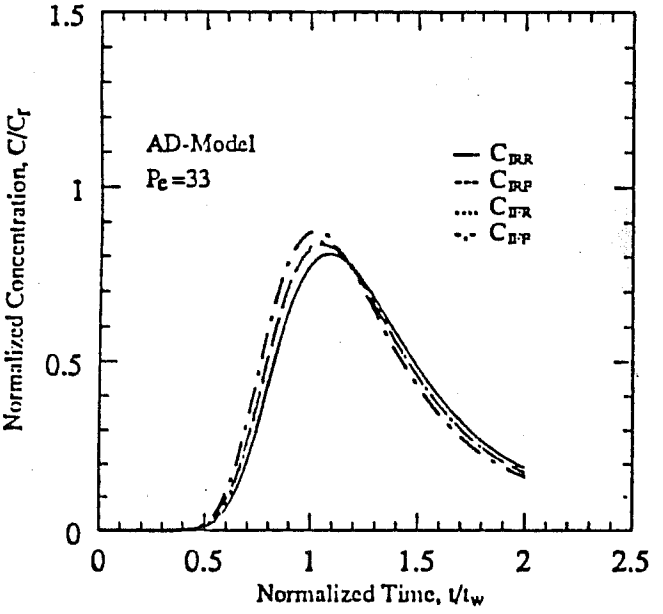


Figure 4.4.2 AD-Model Solutions for Moderate Peclet Numbers

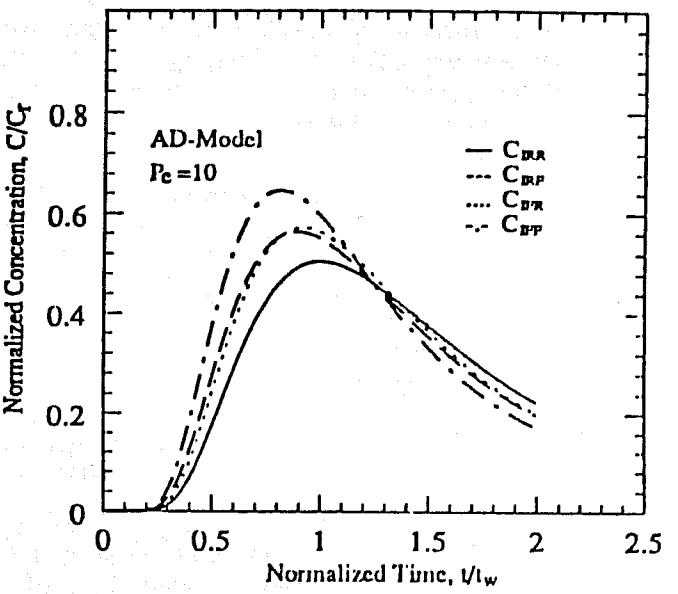


Figure 4.4.3 AD-Model Solutions for Small Peclet Numbers

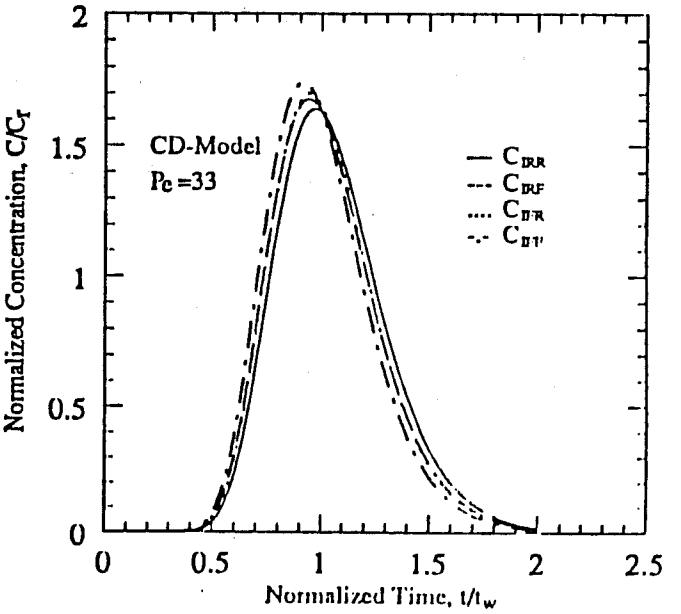


Figure 4.4.4 CD-Model Solutions for Moderate Peclet Numbers

$t = 0$ and decrease with time, and become zero at $t = L/u$. The time term becomes negative causing $\psi$ to be negative, and approach negative unity as time goes to infinity. Values of $\psi$ vary depending on which of the two terms is dominant.

Diffusion into an immobile phase alters the behavior of $\psi$ as follows. In general, diffusion into an immobile phase provides a time dependent storage of tracer. Thus, it slows the movement of a tracer slug and produces asymmetric long tailed tracer return profiles. Specifically, behind the peak, it causes the tracer to spread over longer distances and smooths concentration gradients. This dispersion reduces differences between $C_{IRR}$ and $C_{IFF}$ profiles behind the peak and causes the profiles to persist longer than those with no diffusion.

Effects of diffusion ahead of the peak are dependent on length, dispersivity and average flow velocity of the system. The tracer breakthrough time is directly proportional to average flow velocity and inversely proportional to length of the system. High dispersion also reduces the tracer breakthrough time significantly. Sometimes, the tracer breakthrough time may be too short for diffusion into the immobile phase to affect early parts of tracer return profiles. As a result, at early times, $\psi$ for AD model solutions may behave the same as $\psi$ of the CD model solutions (Fig. 4.4.7). If tracer breakthrough time is not small, diffusion causes numerical differences between $C_{IRR}$ and $C_{IFF}$ to appear later than those differences seen when there is no diffusion (Fig. 4.4.6). This effect is partly due to the slowing down of the tracer slug because of the time dependent storage in the immobile phase.

In summary, the numerical differences between $C_{IRR}$ and $C_{IFF}$ solutions may be as high as sixty percent for the CD model; and differences may be even higher for the AD model. Similar differences will also be observed for other heterogeneous models. These differences will be higher when size distributions exist. Therefore, when analyzing tracer return profiles for systems with moderate to high dispersivity, it is important to use a solution consistent with the method of measurement and the boundary conditions of the experiment.

### 4.4.3 CONCLUSIONS

Equations of linear dispersive systems are satisfied by two different concentration variables, $C_R$ and $C_F$, commonly used in tracer studies. Further, initial and boundary conditions determine whether the solution is in terms of $C_R$ or $C_F$. Failure to distinguish between these two concentration variables leads to solutions inconsistent with the conditions of the experiment.

Solutions to heterogeneous medium models for various initial and boundary conditions are classified in terms of $C_R$ and $C_F$. It is shown that numerical differences between solutions are significant for highly dispersive systems ($P_e < 30$). Therefore, for highly dispersive systems, it is essential to use solutions that are consistent with experimental measurements.

These concepts must also be used in simulators to specify boundary conditions properly and to avoid material balance errors.

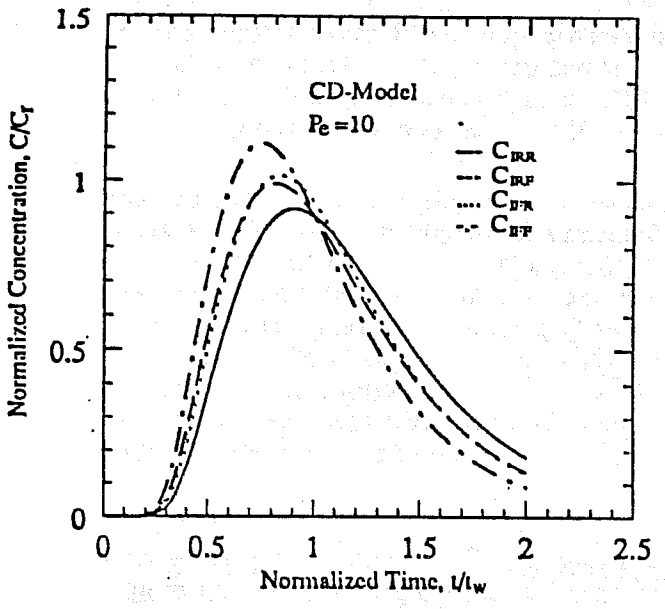


Figure 4.4.5 CD-Model Solutions for Small Peclet Numbers

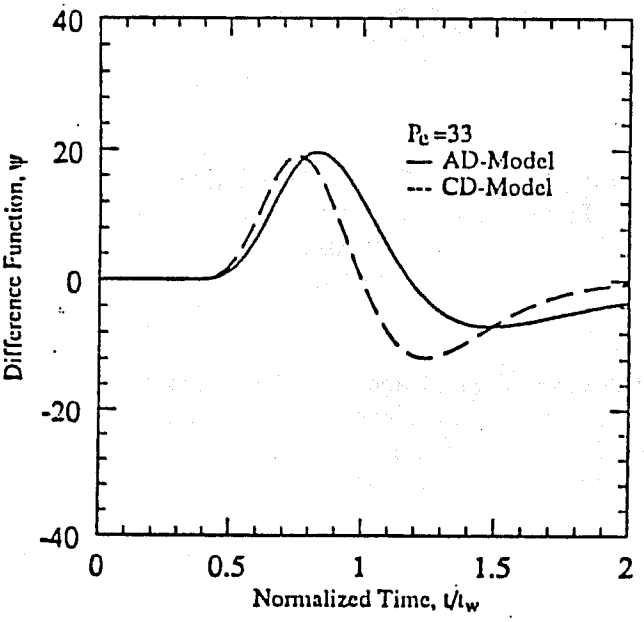


Figure 4.4.6 Numerical Differences between $C_{IFF}$ and $C_{IRR}$ for Moderate Peclet Numbers

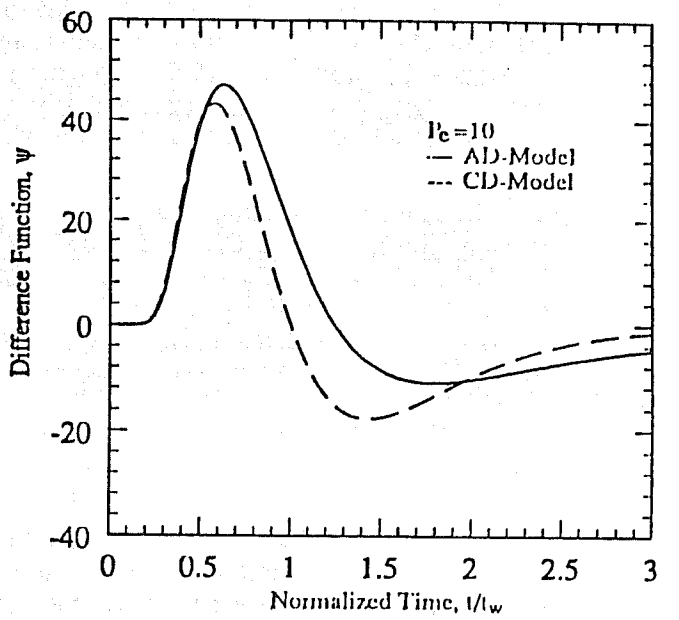


Figure 4.4.7 Numerical Differences between $C_{IFF}$ and $C_{IRR}$ for Small Peclet Numbers

## 4.4.4 REFERENCES


1. Aris, R.: "On Shape Factors for Irregular Particles-I," *Chem. Eng. Sci.*, (1957), 6, 262-268.

2. Avdonin, N. A.: "Some Formulas for Calculating the Temperature Field of a Stratum Subject to Thermal Injection," *Nefti Gaz*, (1964), 3, 37-41.

3. Barker, J. A.: "Laplace Transform Solutions for Solute Transport in Fissured Aquifers," *Adv. Water Resour.*, (1982), 6, 98-104.

4. Barker, J. A.: "Block Geometry Functions Characterizing Transport in Densely Fissured Media," *J. Hydrol.*, (1985), 7, 263-279.

5. Barry, D. A. and Sposito, G.: "Application of the Convection-Dispersion Model to Solute Transport in Finite Soil Columns," *Soil Sci. Am. J.*, (1988), 52, 3-9.

6. Bear, J. and Berkowitz, B: "Groundwater Flow and Pollution in Fractured Aquifers," *Developments in Hydraulic Engineering*, Vol. 4, P. Novak (Editor), Elsevier, London, (1987), 175-235.

7. Belani, A. K. and Jalali-Yazdi, Y.: "Estimation of Matrix Block Size Distribution in Naturally Fractured Reservoirs," SPE paper # 18171, Presented at the 63rd Annual Fall Technical Conference, (1988), Houston, TX.

8. Bretz, R. E. and Orr, F. M. Jr.: "Comparison of Analytical and Explicit Finite Difference Solutions of the Convection-Dispersion Equation," PRRC report 85-6, (1985), New Mexico petroleum Recovery Research Center.

9. Brigham, W. E.: "Mixing Equations in Short Laboratory Cores," *Soc. Pet. Eng. J.*, (1974), 14, 91-99.

10. Carslaw, H. S. and Jeager, J. C.: *Conduction of Heat in Solids*, Clarendon Press, Oxford, (1986), 75-77.

11. Cinco-Ley, H., Samaniengo-V, F. and Kuchuk, F.: "The Pressure Transient Behavior for Naturally Fractured Reservoirs with Multiple Block Size," SPE Paper # 14168, Presented at the 60th Annual Fall Technical Conference, (1985), Las Vegas, NV.

12. Clark, R. T.: "A Review of Some Mathematical Models Used in Hydrology with Observations on Their Calibration and Use," *J. Hydr.* (1973), 19, 1-20.

13. Coats, K. H. and Smith, B. D.: "Dead-end Pore Volume and Dispersion in Porous Media," *Soc. Pet. Eng. J.*, Trans. AIME, 231, (March 1964), 73-84.

14. Correa, A. C., Pande, K. K., Ramey, H. J. Jr. and Brigham, W. E.: "Prediction and Interpretation of Miscible Displacement Using a Transverse matrix Dispersion Model," (Sep. 1987), SPE Paper # 16704.

15. Horne, R. N.: "Geothermal Reinjection Experience in Japan," *J. Pet. Tech.*, (March 1982a), 495-503.

16. Johns, T. R. and Jalali-Yazdi, Y.: "Comparison of Pressure Transient Response in Intensely and Sparsely Fractured Reservoirs," SPE Paper # 18800, Presented at SPE California Regional Meeting, (1989), Bakersfield, CA.

17. Kreft, A. and Zuber, A.: "On the Physical Meaning of the Dispersion Equation and its Solutions for Different Initial and Boundary Conditions," Chem. Eng. Sci. 33, (1978), 33, 1471-1480.

18. Kreft, A. and Zuber, A.: "On the Use of the Dispersion Model of Fluid Flow," *Int. J. Appl. Rad. Isot.* (1979), 30, 705-708.

19. Passioura, J. B.: "Hydrodynamic Dispersion in Aggregated Media: I. Theory," *Soil Sci.*, (1971a), 3, 6, 339-344.

20. Parker, J. C. and van Genuchten M. Th.: "Flux-Averaged and Volume-Averaged Concentrations in Continuum Approaches to Solute Transport," *Water Resour. Res.* (1984a), 20 7, 866-872.

21. Rao, P. S. C., Jessup, R. E., Rolston, D. E., Davidson, J. M., and Kilcrease, D. P.: "Experimental and Mathematical Description of Nonadsorbed Solute Transfer by Diffusion in Spherical Aggregates," *Soil. Sci. Soc. Am. J.*, (1980a), 44, 684-688.

22. van Genuchten, M. Th. and Parker, J. C.: "Boundary Conditions for Displacement Experiments Through Short Laboratory Soil Columns," *Soil Sci. Soc. Am.*, (1984), 48, 703-708.

## 4.4.5 APPENDIX: SOURCE FUNCTIONS OF HETEROGENEOUS SYSTEM MODELS

Derivation of a standard source term for the heterogeneous medium equations, and a table showing a classification of their solutions are presented in the following.

A heterogeneous medium may be modelled using one of the following four approaches: the very near field, the near field, the far field and the very far field.

The very near field is usually conceptualized as a fracture, in which the tracer fluid is mobile, located in a porous matrix in which the reservoir fluid is virtually immobile. The exchange of material between fracture and matrix occurs by molecular diffusion. Tracer concentrations across the fracture are equalized before any significant effect of the convection appears. Within the matrix, diffusive transport is assumed to occur only perpendicular to the flow direction in the fracture. Thus, two coupled one-dimensional equations are used to represent tracer transport. The equations are coupled by using the continuity of the flux and concentration across the fracture-matrix interface.

In the near field, tracer transport is considered in a set of well defined preferential flow paths. When a deterministic approach is chosen the transport equations are identical to equations of the very near field approach.

In the far field approach, tracer transport is modelled by using two superposed continua, a mobile phase composed of a network of preferential flow paths, and an immobile phase representing the rest of the system. The immobile phase is assumed to act as a distributed source in the mobile phase. Transfer from mobile to immobile phase may be assumed proportional to the difference between average concentrations of the two phases[13]. Alternatively, a diffusive transport may be assumed between mobile and immobile phases[4,14,21].

Finally, in the very far field approach, the entire medium is treated as a single continuum representing characteristics of both mobile and immobile phases. No source term exists in the transport equation.

In an initially tracer free system, independent of the heterogeneous system it represents, Laplace transform of Eq. 4.4.4 is:

$$D\,\frac{\partial^2 \bar{C}_R}{\partial x^2} - u\,\frac{\partial \bar{C}_R}{\partial x} - fs\bar{C}_R - \bar{q} = 0 \qquad (4.4.17)$$

If the source term is given by Eq. 4.4.8 the normalized instantaneous injection solutions of Eq. 4.4.17 for various injection and detection modes are given in Table 4.4.1. Normalizing parameter $C_r$ in Table 4.4.1 is the concentration that would be obtained if all the injected tracer were to mix in the fracture.

If a diffusive transport is assumed between the two continua, the transport equation in the immobile portion of the system is:

$$\frac{\partial C_m}{\partial t} - D_a\,\nabla^2 C_m + k_m C_m = 0 \qquad (4.4.18)$$

Table 4.4.1 Normalized Solutions to Heterogeneous Displacement Models

| IC & BC | Parameters | Solution |
|---|---|---|
| $\lim_{x\to\infty} C(x,t) = 0$<br>$\lim_{x\to-\infty} C(x,t) = 0$<br>$C(x,0) = \frac{m}{\phi_f A}\delta(x)$<br>$C_m(x,y,0) = 0$<br>$C_m(x,0,t) = C(x,t)$<br>$\lim_{y\to\infty} C_m(x,y,t) = 0$ | $\alpha_1 = \frac{1}{P_e} = \frac{D}{uL}$<br>$\alpha_2 = \frac{1}{t_w} = \frac{u}{L}$ | $\frac{\overline{C}_{IRR}}{C_r} = \frac{1}{\alpha_2\sqrt{1+(4\alpha_1(s+g(s)))/\alpha_2}}\left(\exp^{-1/(2\alpha_1)}\exp^{\sqrt{1/(4\alpha_1^2)+(s+g(s))/(\alpha_1\alpha_2)}}-1\right)^{-1}$ |
| $\lim_{x\to\infty} C(x,t) = 0$<br>$\lim_{x\to-\infty} C(x,t) = 0$<br>$C(x,0) = \frac{m}{\phi_f A}(\delta(x) - \frac{D}{u}\frac{\partial\delta(x)}{\partial x})$<br>$C_m(x,y,0) = 0$<br>$C_m(x,0,t) = C(x,t)$<br>$\lim_{y\to\infty} C_m(x,y,t) = 0$ | $\alpha_1 = \frac{1}{P_e} = \frac{D}{uL}$<br>$\alpha_2 = \frac{1}{t_w} = \frac{u}{L}$ | $\frac{\overline{C}_{IRF}}{C_r} = \frac{1}{2\alpha_2}\left(1+\frac{1}{\sqrt{1+(4\alpha_1(s+g(s)))/\alpha_2}}\right)\left(\exp^{-1/(2\alpha_1)}\exp^{\sqrt{1/(4\alpha_1^2)+(s+g(s))/(\alpha_1\alpha_2)}}-1\right)^{-1}$ |
| $C(x,0) = C_m(x,y,0) = 0$<br>$\lim_{x\to\infty} C(x,t) = 0$<br>$\left[C(x,t) - \frac{D}{u}\frac{\partial C(x,t)}{\partial x}\right]_{x=0} = \frac{m}{Q}\delta(t)$<br>$C_m(x,0,t) = C(x,t)$<br>$\lim_{y\to\infty} C_m(x,y,t) = 0$ | $\alpha_1 = \frac{1}{P_e} = \frac{D}{uL}$<br>$\alpha_2 = \frac{1}{t_w} = \frac{u}{L}$ | $\frac{\overline{C}_{IFR}}{C_r} = \frac{2}{\alpha_2+\alpha_2\sqrt{1+(4\alpha_1(s+g(s)))/\alpha_2}}\left(\exp^{-1/(2\alpha_1)}\exp^{\sqrt{1/(4\alpha_1^2)+(s+g(s))/(\alpha_1\alpha_2)}}-1\right)^{-1}$ |
| $C(x,0) = C_m(x,y,0) = 0$<br>$\lim_{x\to\infty} C(x,t) = 0$<br>$C(0,t) = \frac{m}{Q}\delta(t)$<br>$C_m(x,0,t) = C(x,t)$<br>$\lim_{y\to\infty} C_m(x,y,t) = 0$ | $\alpha_1 = \frac{1}{P_e} = \frac{D}{uL}$<br>$\alpha_2 = \frac{1}{t_w} = \frac{u}{L}$ | $\frac{\overline{C}_{IFF}}{C_r} = \frac{1}{\alpha_2}\left(\exp^{-1/(2\alpha_1)}\exp^{\sqrt{1/(4\alpha_1^2)+(s+g(s))/(\alpha_1\alpha_2)}}-1\right)^{-1}$ |

with the boundary condition

$$C_m = C_R \quad \text{on} \quad \Gamma \tag{4.4.19}$$

The rate of transport between the two continua is:

$$q = -\frac{A_p}{V_t}\,\phi D_a \left(\frac{\partial C_m}{\partial n}\right)_\Gamma \tag{4.4.20}$$

Taking Laplace transform of Eq. 4.4.18 and rearranging:

$$\nabla^2 \bar{C}_m = \chi_m^2 \bar{C}_m \tag{4.4.21}$$

where

$$\chi_m^2 = \frac{s + k_m}{D_a} \tag{4.4.22}$$

If $\psi$ denotes the solution of Eq. 4.4.21 which has boundary values, $\psi = 1$ on $\Gamma$, then[1]:

$$\bar{C}_m = \bar{C}_R \psi \tag{4.4.23}$$

Substituting Eq. 4.4.23 into the Laplace transform of Eq. 4.4.20 results in:

$$\bar{q} = -\frac{A_p}{V_t}\,\phi D_a \left(\frac{\partial \psi}{\partial n}\right)_\Gamma \bar{C}_R \tag{4.4.24}$$

Recalling Eq. 4.4.8, we obtain the function $g(s)$ from Eq. 4.4.24:

$$g(s) = -\frac{A_p}{V_t}\,\phi D_a \left(\frac{\partial \psi}{\partial n}\right)_\Gamma \tag{4.4.25}$$

Eq. 4.4.25 is valid for all heterogeneous systems discussed earlier. Two examples of $g(s)$ are derived for the very near field in the following. First a single fracture (AD) model will be considered. For the AD model, $\psi$ is the solution of the following boundary value problem:

$$\frac{\partial^2 \psi}{\partial y^2} = \chi_m^2 \psi \tag{4.4.26}$$

with $\psi = 1$ at $y = 0$ (4.4.27)

$\psi \rightarrow 0$ $y \rightarrow \infty$ (4.4.28)

and for this problem, Eq. 4.4.24 reduces to:

$$\bar{q} = -\frac{2\phi D_a}{b}\left[\frac{d\psi}{dy}\right]_{y=0} \bar{C}_R \tag{4.4.29}$$

The solution of Eq. 4.4.26 subject to Eqs. 4.4.27 and 4.4.28 is:

$$\psi = \exp(-\chi_m y) \tag{4.4.30}$$

Substituting Eq. 4.4.30 into Eq. 4.4.29 results in:

$$\bar{q} = \frac{2\phi D_a}{b}\chi_m \bar{C}_R \tag{4.4.31}$$

Comparing Eqs. 4.4.8 and Eq. 4.4.29, one finds:

$$g(s) = \frac{2\phi D_a}{b}\chi_m \tag{4.4.32}$$

Second, a model with parallel fractures is considered. The assumption of parallel fractures spaced by a distance, $L$, changes the second boundary condition (Eq. 4.4.28) of Eq. 4.4.26 to:

$$\frac{\partial \psi}{\partial y} = 0 \quad \text{at} \quad y = \frac{L}{2} \tag{4.4.33}$$

Solving Eq. 4.4.26 subject to the above boundary conditions yields:

$$\psi = -\tanh\left[\frac{\chi_m L}{2}\right]\sinh(\chi_m y) + \cosh(\chi_m y) \tag{4.4.34}$$

Eq. 4.4.29 is also valid for the parallel fracture model. Substituting Eq. 4.4.34 in Eq. 4.4.29 yields:

$$\bar{q} = \frac{2\phi D_a}{b}\chi_m \tanh\left[\frac{\chi_m L}{2}\right]\bar{C}_R \tag{4.4.35}$$

Thus, the function $g(s)$ for a parallel fracture system modelled by the very near field approach is:

$$g(s) = \frac{2\phi D_a}{b} \chi_m \tanh\left[\chi_m \frac{L}{2}\right] \tag{4.4.36}$$

For the far field approach, to obtain the function $g(s)$, one may use block geometry functions (BGF) presented by Barker[4]. Using BGF, Barker showed that the source term reduces to a standard form:

$$\bar{q} = -\nu K_m \frac{\chi^2}{a^2} B(\chi) \bar{C}_R \tag{4.4.37}$$

where $B(\chi)$ is the BGF, defined as:

$$B(\chi) = \frac{a}{\chi^2} \left(\frac{\partial \psi}{\partial n}\right)_\Gamma \tag{4.4.38}$$

The parameters which Barker used in Eqs. 4.4.37 and 4.4.38 can be related to the parameters used in this work as follows:

$$S_m = \phi$$
$$k_m = \phi k_m$$
$$K_m = \phi D_a$$
$$\nu = (1 - f)$$
$$\chi^2 = a^2 \chi_m^2$$

The parameter, $a$, defined as the volume to surface ratio of an immobile phase block, is the same in both works. Substituting these definitions into Eq. 4.4.37 and comparing the result with Eq. 4.4.8, one finds:

$$g(s) = (1 - f)\phi D_a \chi_m^2 B(a\chi_m) \tag{4.4.39}$$

For example, by using the BDF, the function $g(s)$ for an infinite cylinder may be evaluated as follows:

$$B(\chi) = \frac{I_1(2\chi)}{\chi I_o(2\chi)} \tag{4.4.40}$$

In terms of the variables used in this work, the BGF for an infinite cylinder becomes:

$$B(\chi_m) = \frac{I_1(2a\chi_m)}{a\chi_m I_o(2a\chi_m)} \tag{4.4.41}$$

Substituting this definition into Eq. 4.4.39, one finds:

$$g(s) = \frac{(1-f)\phi D_a}{a} \chi_m \frac{I_1(2a\chi_m)}{I_o(2a\chi_m)} \tag{4.4.42}$$

In the same way, we can use BGFs for other geometries to derive the function $g(s)$ (Table 4.4.2). Expressions are derived for a large variety of geometries and sizes of nonflowing media. A size distribution function may also be used. For this case the source function $g(s)$ is derived as described next.

Consider a reservoir composed of matrix blocks of multiple sizes uniformly distributed throughout the medium. Also, let $f_i$ represent the pore volume stored in matrix blocks of size $a_i$ (volume to surface ratio of a block), expressed as a fraction of the total pore volume of the matrix in the reservoir. By definition:

$$\frac{\phi_{mi} V_{mi}}{\phi V_m} = f_i \tag{4.4.43}$$

The source term for the matrix blocks of size $a_i$ is:

$$\overline{q}_i = -\frac{A_{pi}}{V_t} \phi D_a \left(\frac{\partial \psi_i}{\partial n}\right)_\Gamma \overline{C}_R \tag{4.4.44}$$

For $NB$ number of sizes, the source term becomes:

$$\overline{q}_i = \sum_{i=1}^{NB} \overline{q}_i = \sum_{i=1}^{NB} -\frac{A_{pi}}{V_t} \phi D_a \left(\frac{\partial \psi_i}{\partial n}\right)_\Gamma \overline{C}_R \tag{4.4.45}$$

Since the entire immobile phase fraction in the total system is:

$$(1-f) = \frac{V_m}{V_t} \tag{4.4.46}$$

and $a_i$ is given by:

$$a_i = \frac{V_m}{A_{pi}} \tag{4.4.47}$$

substituting Eqs. 4.4.46 and 4.4.47 into Eq. 4.4.45 results in:

$$\overline{q}_t = -\sum_{i=1}^{NB} (1-f)\phi D_a \frac{f_i}{a_i} \left(\frac{\partial \psi_i}{\partial n}\right)_\Gamma \overline{C}_R \tag{4.4.48}$$

Table 4.4.2 Source Functions for Heterogeneous Medium Models

| Approach | Model | a | $g(s)$ |
|---|---|---|---|
| the very near field | single fracture | - | $\frac{2\phi D_a}{b}\chi_m$ |
| | parallel fractures | $L/2$ | $\frac{2\phi D_a}{b}\chi_m \tanh(a\chi_m)$ |
| the far field | parallel plates | $L/2$ | $\frac{(1-f)\phi D_a}{a}\chi_m \tanh(a\chi_m)$ |
| | sphere | $R/3$ | $\frac{(1-f)\phi D_a}{a}\chi_m \left(\coth(3a\chi_m) - \frac{1}{3a\chi_m}\right)$ |
| | cylinder | $R/2$ | $\frac{(1-f)\phi D_a}{a}\chi_m \left(\frac{I_1(2a\chi_m)}{I_0(2a\chi_m)}\right)$ |
| | Coats-smith | - | $\frac{M(1-f)s}{(1-f)s+M}$ |

Notice if the rate constant $M$ is assumed to be:

$$M = \frac{\alpha D_a}{(1-f)a^2} \tag{1}$$

the source function becomes:

$$g(s) = (1-f)(s + k_m)\frac{\alpha/(1-f)}{a^2\chi_m^2 + \alpha/(1-f)} \tag{2}$$

as given by Barker[3].

For a continuous variation of matrix block sizes, $f_i$ is the probability distribution function of matrix blocks of size $a_i$. Then, Eq. 4.4.48 becomes:

$$\bar{q}_i = - \int_{a_{min}}^{a_{max}} (1-f)\phi D_a \frac{f(a)}{a} \left(\frac{\partial \psi_i}{\partial n}\right)_\Gamma \bar{C}_R \, da \tag{4.4.49}$$

Substituting Eq. 4.4.25 into Eq. 4.4.49 yields:

$$\bar{q}_i = - \bar{C}_R \int_{a_{min}}^{a_{max}} f(a) g(s) da \tag{4.4.50}$$

where $g(s)$ is the source function for a block size, $a$. Therefore, Eq. 4.4.50 states that the source function for a uniformly distributed size case is merely the integration of $g(s)$ for a single size with its distribution function. As a result, for a distribution of matrix blocks (immobile phases) with multiple sizes and a particular geometry we find that Eq. 4.4.4 holds for all independent variables $J$, $C_R$ and $C_F$. A large variety of probability distribution functions used for $f_i$ can be found in works by Belani and Jalali-Yazdi[7] and Johns and Jalali-Yazdi[16].

It is possible to extend the model to assume several geometries as well as multiple block sizes. However, since results are more sensitive to size variation than to geometry, accounting only for the size variation is often adequate in modelling.

# 4.5 NUMERICAL STUDY OF INTERWELL TRACER TESTS WITH NONUNITY MOBILITY RATIO

(B. Goyeau)

A numerical study of tracer flows was carried out for different developed flooding patterns for nonunity mobility ratio. The UTCHEM simulator from the University of Texas at Austin was used to model physical dispersion phenomena and, therefore, to account for numerical dispersion phenomena associated with finite difference solution of convection-dispersion equations. A verification of the program was performed in one dimension by comparison with analytical solutions of the convection-dispersion equation.

## 4.5.1 OBJECTIVES OF THE STUDY

Since the overall efficiency in enhanced oil recovery processes depends on reservoir heterogeneities, single and well-to-well tracer tests have been the subject of several studies[1,2,3] to determine quantitative information about reservoir characteristics. Indeed, the main objective of these studies was to examine the sensitivity of test responses to the presence of heterogeneity and to extract the layer parameters from an overall tracer breakthrough profile.

In most cases, quantitative analysis of well-to-well tracer tests have been performed for a classical multilayer five-spot pattern. However, Abbaszadeh-Dehghani and Brigham[4] developed equations for computing tracer breakthrough curves in several flooding patterns (five-spot, direct line drive, staggered line drive and seven spot) by analytically formulating tracer slug concentration in a general streamtube. To simplify the analysis, tracer breakthrough curves for different patterns were correlated into a single set of curves. Finally, a computer program was developed to decompose a tracer profile from a multilayered reservoir into several responses from individual layers. In this study, the theory and analysis of tracer flow behavior was formulated on the assumption of unit mobility ratio, and exact analytical equations were obtained in the form of elliptic integrals which provide breakthrough curves for the different patterns. An attempt was made to define pattern breakthrough curves analytically for nonunit mobility ratio in a developed five-spot, but the results obtained contradicted experimental observations. This was because of the unrealistic assumption that streamlines are independent of the mobility ratio.

Because the streamtube procedure can not generate breakthrough curves at nonunity mobility ratio accurately and because there is a need to describe tracer flow in such systems, we intend to develop a numerical study of interwell tracer tests when a mobility contrast exists. In the same way as Abbaszadeh-Dehghani and Brigham[4], a correlation between breakthrough curves from several patterns and mobility ratio will be sought and compared.

Generally, tracer tests are slug processes whereby a small amount of tracer is injected into a reservoir, and, therefore, mixing phenomena characterized by longitudinal and transverse dispersion have an important effect on the performance of these processes. Proper numerical modelling is necessary for an accurate representation of these processes, especially considering numerical dispersion associated with finite difference solutions of the convection-dispersion equations. Because simulation results of pattern flooding can be affected by grid orientation, an analysis of a grid orientation effect will be included in this study.

In order to reach these objectives, we decided to use the University of Texas UTCHEM simulator. UTCHEM is a three-dimensional compositional chemical flooding simulator, well adapted to describe tracer flow in different patterns, and also to control numerical dispersion and grid orientation effects. Several convection differencing schemes are available in this simulator. Of particular value is a third-order scheme based on Leonard's method involving accurate and inexpensive simulation of small dispersivities with relatively large gridblocks.

## 4.5.2 DESCRIPTION OF UTCHEM

We will not describe the UTCHEM simulator in detail. The main features of this program have been the subject of several papers and theses[5,6,7,8]. We will give some information about the principal characteristics of this simulator. Because of the necessity to simulate mixing phenomena, and, therefore, to minimize numerical dispersion, the four convective differencing schemes available in UTCHEM will be reviewed.

Contrary to the traditional Black-Oil simulators, UTCHEM is a compositional simulator where several components are present in each phase and, pressure and phase distribution must be determined as well as the composition of the different phases. Among the three main categories of Enhanced Oil Recovery (EOR), UTCHEM has been specially developed to simulate chemical flooding processes. It is defined as an isothermal, slightly compressible, three-dimensional compositional chemical flooding simulator. The different chemical flooding EOR methods that can be used in this simulator are polymer flooding, alkaline flooding, and micellar/polymer flooding. Simulation of these processes can be performed either in three dimensional cartesian coordinates or, in a two-dimensional radial ($r-z$) system[8]. The different chemical processes can be simulated using nineteen components which may form three liquid phases, aqueous, oleic, and microemulsion. The components available in UTCHEM are water, oil, surfactant, polymer, chloride, calcium, two alcohols, and three tracers. Four components are also available if the gel option is selected, and four alkaline options can provide up to eighteen components. The major phenomena modelled in the simulator are dispersion, phase density, modeling of polymer properties, surfactant adsorption, phase viscosity, capillary pressure, relative permeability model, capillary desaturation, interfacial tension, phase behavior, cation exchange, tracer flow, capacitance and gels. All phenomena can be simulated in heterogeneous reservoirs using constant variable grid size. An automatic time step selector is also available. Different types of well constraint can be used, and gravity effects can be included.

Since it is possible to consider all these phenomena, UTCHEM has many input options to specify which phenomena will be included. Therefore, one of the main difficulties for a user of UTCHEM is to define the input data choice correctly. Four input data files are present. The first file is used to title and describe the run. The second file concerns the grid characteristics, initial condition, and also the output options. Injection/production data are specified in the third file, while the fourth one is related to physical properties.

The main assumptions made in the development of the mathematical model of UTCHEM are isothermal reservoir, slightly compressible fluid and solid, Darcy's law applies, local thermodynamic equilibrium, dispersion follows Fick's law for multiphase flow, and surfactant and polymer are treated as monospecies without a molecular weight distribution.

The derivation of the conservation equations and the slightly compressible formulation of the pressure equation are given in detail by N. Saad[7], but some important concepts are given here.

In order to simulate physical dispersion, a full hydrodynamic dispersion tensor is used in UTCHEM. The first diagonal term is:

$$K_{xxkl} = \frac{D_{kl}}{\tau} + \frac{1}{\phi S_l |u_l|} \left[ \alpha_{Ll} u_{xl}^2 + \alpha_{Tl} \left[ u_{yl}^2 + u_{zl}^2 \right] \right] \tag{4.5.1}$$

and the symmetric extra-diagonal term is:

$$K_{xykl} = \frac{(\alpha_{Ll} - \alpha_{Tl})}{\phi S_l} \frac{u_{xl} u_{yl}}{|u_l|} \tag{4.5.2}$$

The IMPES method is used in the simulator. The pressure equation is solved first implicitly to obtain phase pressures and phase velocities. Then the conservation equations are solved explicitly for overall concentrations. The Jacobian Conjugate Gradient iterative method is used to solve linear systems.

The numerical dispersion associated with finite difference solution of convection-dispersion equations is mainly generated by truncation error of the finite difference operator used to approximate the first order derivatives of the convective term. These truncation errors can be significant and sometimes their effects can be larger than the physical dispersion effects. Because of the hyperbolic nature of these equations, when convective flow is predominant, oscillary solutions can be obtained at high Peclet numbers.

In order to eliminate or minimize numerical dispersion effects, four methods are available in UTCHEM. The characteristics, advantages and disadvantages of the different methods follow. More detail is given by Saad[7].

a) Single point upstream

The convective term in the component conservation equation is approximated by:

for $\phi_{i-1} > \phi_i > \phi_{i+1}$

$$\frac{\partial}{\partial x} (u_{xl} C_{kl})_i = \frac{(u_{xl} C_{kl})_i - (u_{xl} C_{kl})_{i-1}}{\Delta x_i} + \frac{\Delta x_i}{2} \frac{\partial}{\partial x} \left[ u_{xl} \frac{\partial C_{kl}}{\partial x} \right]_i + \text{hot} \tag{4.5.3}$$

where "hot" designates higher order terms. This method has good stability, but is strongly affected by numerical dispersion and grid orientation effects and provides inaccurate results.

b) Chaudhari's method

In order to approximate the convective term with a second order approximation, a negative dispersion term is introduced which is equal to the leading term in the truncation errors[9]. The second term of Equation (4.5.3) becomes:

$$\frac{\partial}{\partial x} \left[ (\Delta x_i u_{xl} - \phi S_l K_{xykl}) \frac{\partial C_{kl}}{\partial x} \right] \tag{4.5.4}$$

where $\Delta x_i$ is assumed constant.

This method is effective to reduce numerical dispersion but requires a low Peclet number. For higher cell Peclet number, oscillations are observed. Another limitation of this method is a constant grid size requirement.

## c) Two point upstream

In this method convective differencing for constant velocity and grid sizes is given by:

for $\phi_{i-1} > \phi_i > \phi_{i+1}$

$$u\left[\frac{\partial C}{\partial x}\right]_i = u\left[\frac{3C_i + 4C_{i-1} - C_{i-2}}{2\Delta x_i} + \frac{\Delta x_i^2}{3}\left[\frac{\partial^3 C}{\partial x^3}\right]_i + \text{hot}\right] \qquad (4.5.5)$$

The truncation error is second order in space. Two conditions are necessary:

- The grid block face values, $C_{i+½}$ and $C_{i-½}$, must be positive or nul.
- The monotonicity condition must be respected.

This method is more difficult than the two previous ones. However, improved accuracy results for the same number of blocks.

## d) Leonard's third order method

The following differencing form is proposed[10]:

for $u > 0$,

$$u\left[\frac{\partial C}{\partial x}\right]_i = u\left[\frac{C_{i+1}+C_{i-1}}{2\Delta x_i} - \frac{C_{i+1}-3C_i+3C_{i-1}-C_{i-2}}{6\Delta x_i} - \frac{\Delta x_i^3}{12}\left[\frac{\partial^4 C}{\partial x^4}\right]_i + \text{hot}\right] \qquad (4.5.6)$$

where four nodal points are used and the order of truncation error is 3. This scheme applied to the convection term leads to differencing equations where the number of nodal points depends on the velocity sign. If the velocities have the same sign on the two sides of the block, then four points are used. For diverging flow, only three points are used, while a five point symmetric scheme is used for converging flow. In two dimensional flow, the number of points varies from five to nine and varies from seven to thirteen for three dimensional flow.

As in the two-point upstream method, $C_{i+½}$ and $C_{i-½}$ must be greater than or equal to zero, and the monotonicity condition must also be satisfied. According to Leonard[10], stability of this method is ensured because of strict negative feed-back sensitivity. Contrary to the previous method, Leonard's third order method is able to provide both stable and accurate results for a first order spatial derivative of the convection term.

## 4.5.3 VALIDATION

The first step of this study was installation of the scalar version of UTCHEM D-4.23 on the Apollo 10000. Some modifications were necessary since there are incompatibilities between the different systems and the compiler used.

Then UTCHEM D-4.23 was validated on our system in one dimensional miscible displacement (tracer in aqueous phase). In this example, convective flow dominates and the Peclet number is equal to 1000, while the Courant number is 0.05. Results were compared with analytical solution of the convection-dispersion equation[11] (Figure 4.5.1). In this case, Leonard's method was selected and the agreement was outstanding. However, when the Courant number increased (C=0.1), instabilities were observed.

A comparison of the four differencing methods has been performed and is shown on Figure 4.5.2. The single point upstream method is stable, but produces smearing of the front. The Chaudhari method is close to the analytical solution, but is unstable. The two-point upstream method seems unappropriate for this range of Peclet number.

An accurate description of dispersion phenomena is possible only if enough blocks are considered. Figure 4.5.3 presents a comparison of concentration profiles using different numbers of gridblocks. If the number of cells is too small, even if Leonard's method is used, numerical dispersion is larger than physical dispersion and the solution is not correct.

The results obtained in this validation showed that some parameters like the number of gridblocks, the Peclet number, and the time step have a strong influence on the solution. Therefore, the choice requires attention.

Some complementary runs were also carried out to validate the simulator in a two-dimensional, five-spot pattern where analytical solutions were available[4]. A set of simulations will be performed in several repeated patterns where mobility contrast exists. As done by Abbaszadeh-Dehghani and Brigham[4], a correlation of tracer breakthrough curves from different patterns will be sought to find whether a single tracer breakthrough curve is possible.

## 4.5.4 REFERENCES

1. Yuen, D.L., Brigham, W.E. and Cinco-L., H.: "Analysis of Five-Spot Tracer Tests to Determine Reservoir Layering", U.S. DOE Report SAN 1265-8, Washington D.C., 1979.

2. Brigham, W.E. and Abbaszadeh-Dehghani, M.: "Tracer Testing for Reservoir Description", J. Pet. Tech., 1987, 519-527.

3. Mishra, S.: "On the Use of Pressure and Tracer Test Data for Reservoir Description", Ph.D. dissertation, 1987, Stanford University, Stanford, California.

4. Abbaszadeh-Dehghani, M. and Brigham, W.E.: "Analysis of Unit-Mobility Ratio Well-to-Well Tracer Flow to Determine Reservoir Heterogeneity", Stanford University, Petroleum Research Institute Report SUPRI-TR-36, 1982, Stanford, California.

5. Datta Gupta, A.: "Three Dimensional Simulation of Chemical Flooding", Master's dissertation, 1985, Univ. of Texas, Austin, Texas.

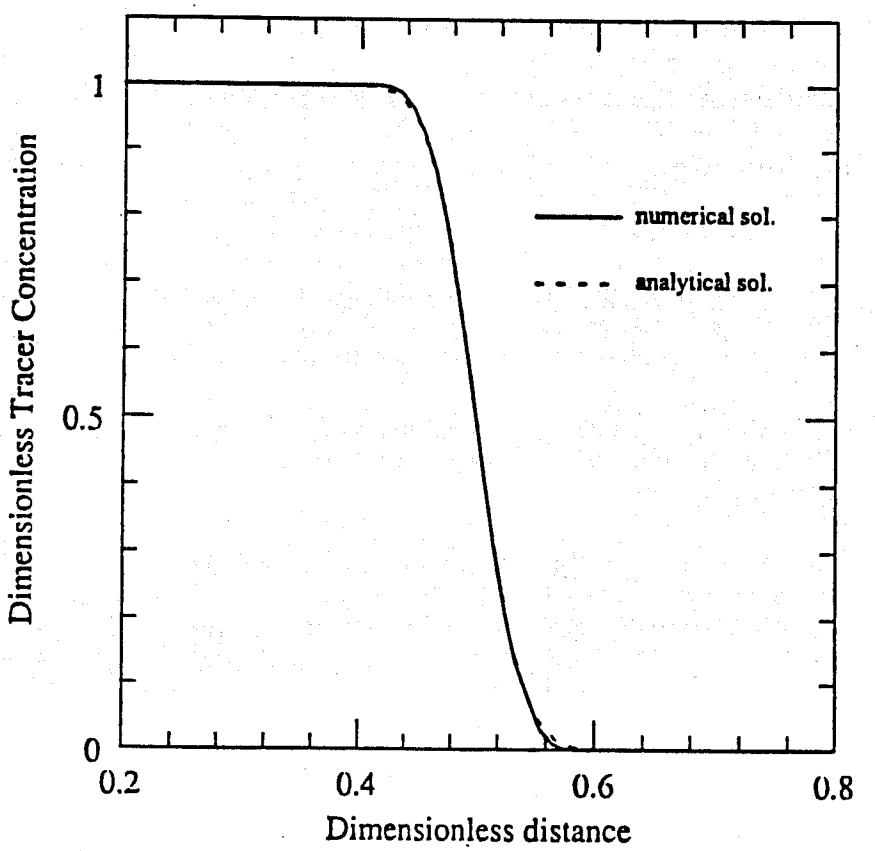


Figure 4.5.1 Dimensionless tracer concentration vs dimensionless distance for numerical and analytical solutions

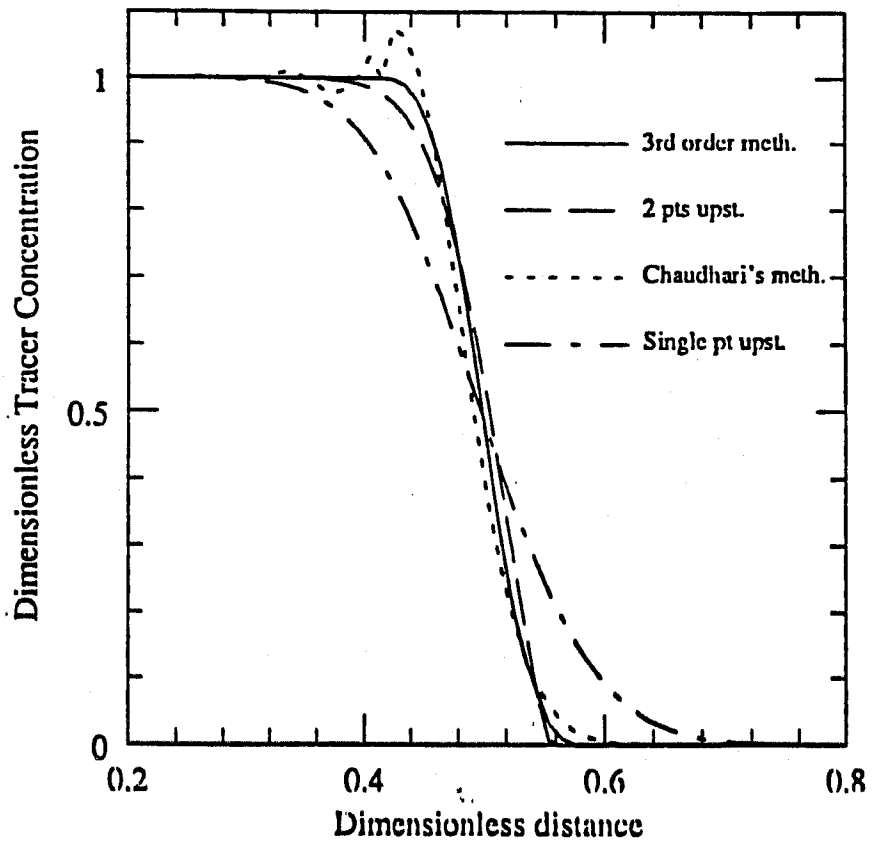


Figure 4.5.2 Tracer concentration vs distance showing numerical dispersion

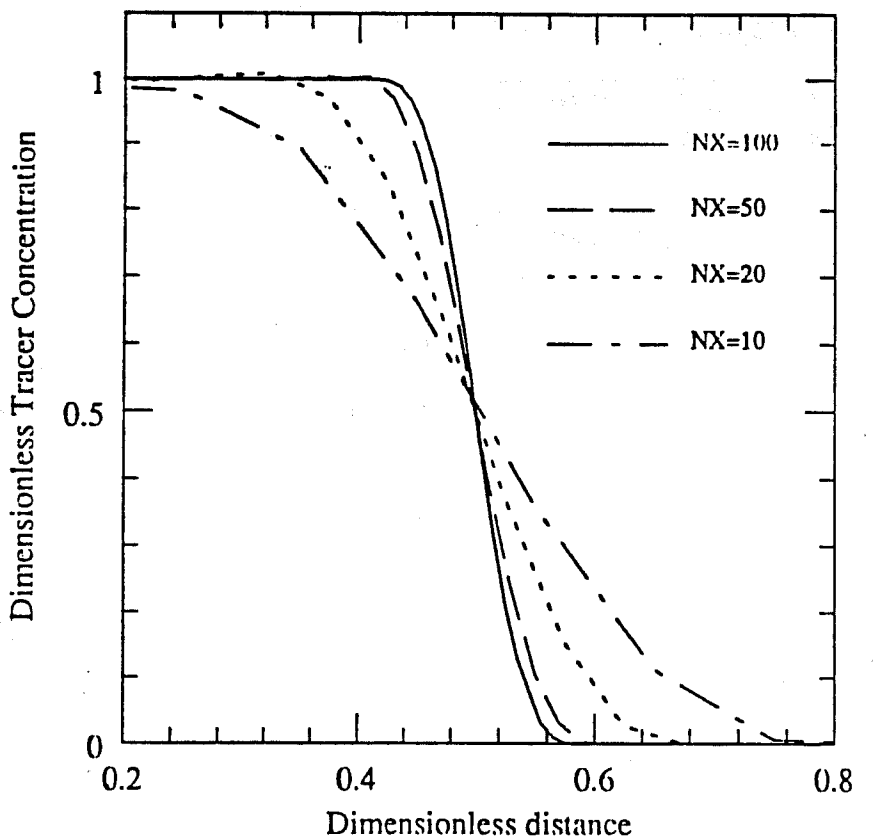


Figure 4.5.3 Tracer concentration vs distance for a range of numbers of cells

6. Datta Gupta, A., Pope, G.A., Sepehrnoori, K., Tharsher, R.L.: "Asymmetric, Positive Definite Formulation of a Three-Dimensional Micellar/Polymer Simulator". SPE Reservoir Engineering, Nov., 1986, 622-632.

7. Saad, N.: "Field Simulation of Chemical Flooding", Ph.D. dissertation, 1989, Univ. of Texas, Austin, Texas.

8. Descant III, F.J.: "Simulation of Single-Well Tracer Flow", Master's dissertation, 1989, Univ. of Texas, Austin, Texas.

9. Chaudhari, N.M.: "An Improved Numerical Technique for Solving Multidimensional Miscible Displacement Equations", Soc. Pet. Eng. J., Sept. 1971, 277-284.

10. Leonard, B.P.: "A Survey of Finite Difference of Opinion on Numerical Muddling of the Incomprehensible Defective Confusion Equation", Finite Element Methods for Convection Dominated Flows, ASME, New York, NY, Dec. 2-7, 1979, 1-17.

11. Aronosky, J.S. and Heller, N.R.: "A Diffusion Model to Explain Mixing of Flowing Miscible Fluids in Porous Media", Trans. AIME, 1957, 210, 345-349.

# PROJECT 5: FIELD SUPPORT SERVICES

The purpose of this project is to provide technical support for field test design. An example is the use of numerical thermal simulators to study practical field problems, monitoring of DOE sponsored or industry initiated field projects, and economic evaluation procedures. Two projects are reported. The first is a semianalytical prediction of recovery from steam floods, the second is an evaluation of various schemes to optimize such differing operations as well testing, steam flooding and reservoir simulation.

## 5.1 A SEMIANALYTICAL THERMAL MODEL FOR A LINEAR STEAM DRIVE (R.J. Gajdica)

A technical report titled "A Semianalytical Thermal Model for Linear Steam Drive," by R.J. Gajdica was sent to DOE for publication. The following is a summary of this report.

Thermal oil recovery by steam injection has proven to be an effective means of recovering heavy oil. Forecasts of reservoir response to the application of steam are necessary before starting a steam drive project. Thermal numerical models are available to provide forecasts. However, these models are expensive and consume a great deal of computer time. An alternative to numerical modeling is to use an analytical model. Analytical models are fast, but the assumptions necessary to generate the solutions may lead to poor results. Common assumptions in analytical models are: (1) a horizontal reservoir, (2) incompressible oil, water, and formation, and (3) no thermal expansion of the oil, water and formation. Furthermore, many analytical models require steam zone saturation as input, or do not consider a water front when calculating production rates. Finally, one-dimensional analytical models do not consider gravity override of steam.

A semianalytical model (SAM) was developed for one-dimensional linear systems and two-dimensional linear cross-sectional systems. Wells are located at both ends of the reservoir. At the injection well, wet steam is injected at a constant rate and enthalpy. The production well produces at a constant flowing bottom hole pressure. The SAM includes formation dip, compressible formation, water, and oil, and thermal expansion of the formation, water and oil. The model automatically calculates the steam zone steam saturation and includes the water front and overburden heat losses. The two-dimensional model also includes gravity override of steam.

The system of equations is solved by iterating on the injection well pressure. For each iteration, the lengths of the steam, water, and oil zones are determined. The pressure drop is calculated for each of these zones and at each well to compute the production well pressure. This value is compared to the production well boundary condition, and iteration continues until convergence is achieved, usually in five iterations. In the process, front locations, temperatures, pressures, and phase saturations are determined for each of the zones. Since the temperatures and pressures are computed, the compressibility and thermal expansion of the rock, oil, and water can be considered. Oil and water production rates are calculated by material balance. In the two-dimensional model, a new empirical method is presented which determines the shape of the steam front, and an extension of an existing water flooding correlation is used to determine the volumetric sweep efficiency for the reservoir.

Many cases were run on both the SAM and a numerical model. The Computer Modelling Group's general purpose thermal simulator ISCOM was used for comparisons. The SAM runs were several orders of magnitude faster than the thermal simulator, yet matched thermal simulator results in over 2,000 runs over a wide range of variables. The result is a computer program that can be run on a personal computer by a field engineer. The program is not intended to replace a thermal simulator. The simulator is more general and can handle more detailed problems than the SAM. However, the SAM is ideal for: (1) preliminary studies before running a numerical model, (2) running many cases for sensitivity analysis and optimization, (3) screening prospective field projects, and (4) providing guidance for operating decisions.

## 5.2 A STUDY ON NEWTON RELATED NONLINEAR METHODS IN WELL TEST ANALYSIS, PRODUCTION SCHEDULE OPTIMIZATION AND RESERVOIR SIMULATION (J. Barua)

A technical report titled "A Study on Newton Related Nonlinear Methods in Well Test Analysis, Production Schedule Optimization and Reservoir Simulation", SUPRI TR 70, by J. Barua, was published in November 1989. The following is an abstract of this report.

This is a study on the use of alternative nonlinear methods in automated well test analysis, production and injection schedule optimization and in reservoir simulation. In automated well test analysis the advantages and disadvantages of second-order partial derivatives are investigated. Newton's method is shown to be prone to difficulties. However by adjusting the eigenvalues of the Hessian matrix, performance can be substantially improved.

In optimizing the cyclic steam injection process, Newton's method is compared with the Quasi-Newton method using a simplified model to simulate the process. The Quasi-Newton method does significantly better than Newton's method in saving function evaluations. Specific operating strategies for the process are identified: the need to eliminate soak, the need for greatly increased steam volumes and temperatures, and the need to optimize a combination of economic objectives.

The two methods are then compared in reservoir simulation. Tests show that while it is possible to use the Quasi-Newton method to build up inverse Jacobians as the iterations proceed, for difficult problems the method requires the use of matrix solution techniques. The method then becomes directly comparable to Newton's method. Tests show that depending upon the linear scheme used, and the difficulty of the problem, the Quasi-Newton method may prove to be less expensive than Newton's method in certain cases.

The study also addresses the issue of building scalable parallel reservoir simulators. Residual constraints are used to improve the robustness of the parallel matrix solution scheme. The solution of the constraint matrix is shown to be a critical point

☆ U.S. GOVERNMENT PRINTING OFFICE: 1990—761 -030 20036